Dynamical System Representation and Analysis of Unsteady Flow and Fluid-Structure Interactions

Ahmed A. Hussein

Dissertation submitted to the Faculty of the

Virginia Polytechnic Institute and State University

in partial fulfillment of the requirements for the degree of

Doctor of Philosophy

in

Engineering Mechanics

Muhammad R. Hajj, Chair

Saad A. Ragab

Robert A. Canfield

Craig A. Woolsey

September 26, 2018

Blacksburg, Virginia

Keywords: Finite-State Unsteady Aerodynamics, Lagrangian, Point Vortices, Flutter, Aeroelasticity, Finite Element Method, Flexibility, Hydroelasticity, Nonlinear Time-Periodic Dynamics, Floquet Analysis, Optimal Control

Dynamical System Representation and Analysis of Unsteady Flow and Fluid-Structure Interactions

Ahmed A. Hussein

(ABSTRACT)

A dynamical system approach is utilized to reduce the representation order of unsteady fluid flows and fluid-structure interaction systems. This approach allows for significant reduction in the computational cost of their numerical simulations, implementation of optimization and control methodologies and assessment of their dynamic stability. In the first chapter, I present a new Lagrangian function to derive the equations of motion of unsteady point vortices. This representation is a reconciliation between Newtonian and Lagrangian mechanics yielding a new approach to model the dynamics of these vortices. In the second chapter, I investigate the flutter of a helicopter rotor blade using finite-state time approximation of the unsteady aerodynamics. The analysis showed a new stability region that could not be determined under the assumption of a quasi-steady flow. In the third chapter, I implement the unsteady vortex lattice method to quantify the effects of tail flexibility on the propulsive efficiency of a fish. I determine that flexibility enhances the propulsion. In the fourth chapter, I consider the stability of a flapping micro air vehicle and use different approaches to design the transition from hovering to forward flight. I determine that first order averaging is not suitable and that time periodic dynamics are required for the controller to achieve this transition. In the fifth chapter, I derive a mathematical model for the free motion of a two-body planar system representing a fish under the action of coupled dynamics and hydrodynamics loads. I conclude that the psicform are inherently stable under certain conditions that depend on the location of the center of mass.

# Dynamical System Representation and Analysis of Unsteady Flow and Fluid-Structure Interactions

Ahmed A. Hussein

(GENERAL AUDIENCE ABSTRACT)

We present modeling approaches of the interaction between flying or swimming bodies and the surrounding fluids. We consider their stability as they perform special maneuvers. The approaches are applied to rotating blades of helicopters, fish-like robots, and micro-air vehicles. We develop and validate a new mathematical representation for the flow generated by moving or deforming elements. We also assess the effects of fast variations in the flow on the stability of a rotating helicopter blade. The results point to a new stable regime for their operation. In other words, the fast flow variations could stabilize the rotating blades. These results can also be applied to the analysis of stability of rotating blades of wind turbines. We consider the effects of flexing a tail on the propulsive force of fish-like robots. The results show that adding flexibility enhances the efficiency of the fish propulsion. Inspired by the ability of some birds and insects to transition from hovering to forward motion, we thoroughly investigate different approaches to model and realize this transition. We determine that no simplification should be applied to the rigorous model representing the flapping flight in order to model transition phenomena correctly. Finally, we model the forward-swim dynamics of psciform and determine the condition on the center of mass for which a robotic fish can maintain its stability. This condition could help in designing fish-like robots that perform stable underwater maneuvers.

Dedication

The almighty Allah says in his holy book, the Quran, chapter Yusuf, verse 76

بسم الله الرحمن الرحيم

نَرْفَعُ دَرَجَاتٍ مَّن نَّشَاءُ

وَفَوْقَ كُلِّ ذِي عِلْمٍ

عَلِيمٌ
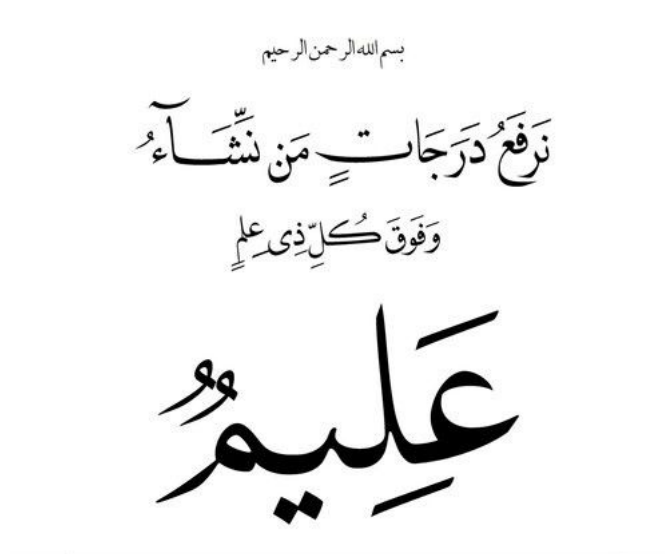
which may be translated as We elevate by degrees whomever We will; and above every person of knowledge, there is one more learned.

Acknowledgments

I would like to thank my supervisor Prof. Muhammad Hajj for his unprecedented technical, spiritual, and financial supports. I was lucky to have a lot of very fruitful discussions with him during the course of this work. I am grateful for his patience and optimism about my work as well as for giving me the freedom to work with other professors. In addition, he was always providing me with sincere beneficial advices regarding my career.

I would like to thank Prof. Robert Canfield for his tremendous help and support. I have really learnt a lot from him. Indeed, he has shaped my future career. In addition to being my mentor for the optimization world, I would say that my contact with Prof. Canfield has considerably affected my academic personality. I am so grateful to Prof. Craig Woolsey for his valuable discussions and suggestions that have really led to better final works. Also, I am so grateful for Professors Saad Ragab for his continuous help and cooperation. I gained a deep and thorough understanding of fluid mechanics through his courses and discussions during our work together. I am so grateful to Prof. Mayuresh Patil for his continuous valuable suggestions and recommendations. I would like to express my deepest gratefulness to Prof. John Burns, Prof. John Rossi, Prof. Martin Klaus, Prof. Christopher Beattie, Prof. Serkan Gugercin for their engraved teachings and comments that led to better understanding of mathematics world. I would like to express my sincere gratefulness for Prof Gamal Elbyoumi, Prof. Samir Elkholy, Prof. Mokhtar Elnomrossy for their inspiration, support and guidance.

I would like to thank my wife Mai and my son Omar for their surpassing help and indescribable endurance. Indeed, without them, I would never be able to make it. Also, I would like to express

my deepest gratitude to my parents for their extra-ordinary spiritual support and encouragement. They were always unflinching pillars to my self, family and work.

Special thanks and appreciation go to Dr. Haithem Taha for his support and guidance. He has been always there to motivate and discuss many technical problems. I would like to thank my colleagues Dr. Mohammed Zakaria, Dr. Jamal Alroyjah, Ahmed Roman, Hisham Shehata, Saeed Al-Nuami. Finally, I would like to thank my friends Mostafa Ali, Amr Hilal, Mohammed Zein, Mohammed Magdy for their continuous encouragement, sincere wishes of success, and lovely moments that made me pursue and overcome any hardships.

Contents

List of Figures

List of Tables

Chapter 1

Introduction

1.1 Background

Some of the models which represent dynamical systems that are involved in engineering applications these days can be described as a first-order differential equation of the form

$$\dot{\boldsymbol{x}} = \boldsymbol{f}(\boldsymbol{x}, t) \tag{1.1}$$

This general differential equation could represent the dynamics of a discrete dynamical system [1, 2] or could be the result of a discretization of a general partial differential equation [3, 4]. Analyzing the dynamics of this system (1.1) depends on the type of the application. In Chapter 2, Eq. (1.1) represents the equations of motion of unsteady point vortices. It was first derived by Brown and Michael [5] using Newtonian approach. Here we proposed a new Lagrangian function from which the same equation of motion could be derived. This represent a reconciliation between Lagrangian and Newtonian approach for the dynamics of unsteady point vortices. The use of previous Lagrangian proposed by Chapman [6] does not yield the Brown-Michael equation.

In Chapter 3, Eq. (1.1) represents the finite degrees of freedom of an aeroelastic system of a helicopter blade rotating in hover. The dynamics of this system is analyzed by linearizing around

the equilibrium positions as

$$\dot{\boldsymbol{x}} = \frac{\partial \boldsymbol{f}(\boldsymbol{x}, t)}{\partial \boldsymbol{x}}\big|_{x - x_0} = \boldsymbol{A}(\boldsymbol{x}_0)\boldsymbol{x} \tag{1.2}$$

The stability of this system is investigated using the eigen value technique. In Chapter 4, Eq. (1.1) represents the finite degrees of freedom of hydroelastic system of a fish tail oscillating in water. The dynamics of this system is analyzed by numerically integrating Eq. (1.1) as

$$\boldsymbol{x}^{m+1} = \boldsymbol{x}^m + \Delta t \boldsymbol{f}(\boldsymbol{m}^{m+1}, t^{m+1}) \tag{1.3}$$

As will be shown later, explicit methods for local iteration introduce numerical instability for this type of problem. Instead, we used an implicit solver for the time integration, Newmark method [7], and compared two different methods for the local iteration: loosely coupling (fixed point iteration with under relaxation factor), and strong coupling (Newton Raphson). The resulting time histories of the deflections $\boldsymbol{x}$ are used to calculate the power and the thrust to compare the efficiency for the rigid case versus the flexible one.

In Chapters 5 and 6, Eq. (1.1) represents the degrees of freedom of the rigid body motion of a flapping micro air vehicle and planar fish-like robotic, respectively. Since the input to this problem is periodic, the equilibrium solution can be described as a periodic solution

$$\boldsymbol{x}(t + T) = \boldsymbol{x}(t) \tag{1.4}$$

The stability of this type of orbit is assessed using Floquet theory. As seen from the above discussion, all the problems that are discussed in this dissertation are written in the same compact form (1.1), the analysis of their dynamics are different depending on two main things: 1) their nature, either finite degrees of freedom system or of a finite discretization of an infinite degrees of freedom system , 2) the goal of the analysis. Figure 1.1 shows a brief layout of the problems solved in this dissertation.

$$\dot{x} = f(x, t)$$

Reconciliation between Lagrangian and Newtonian Approach for **Unsteady Point Vortices**

$$\frac{d}{dt}\left(\frac{\partial L}{\partial \dot{x}}\right) - \frac{\partial L}{\partial x} = 0 \rightarrow \dot{x} = f(x, t)$$

Discretization of Infinite Degrees of Freedom System

Rigid Body Dynamics of FWMAV and **Fish planar motion**

$$\dot{x} = f(x, t)$$

Floquet Analysis and Controller Design

$$x(t + T) = x(t)$$

Eigen Value Analysis

$$\dot{x} = A(x_0)x$$

Rotor Blade in Hovering

Direct Numerical Integration

$$x^{m+1} = x + \Delta t\, f(x^{m+1}, t^{m+1})$$

Flexible Fish Tail

Figure 1.1: Layout of the techniques used to solve the different problems in the dissertation.

1.2   Layout of the Dissertation

In Chapter 2, we proposed a new Lagrangian function for unsteady point vortices [8, 9]. The new Lagrangian and Chapman's [6] one yield the same equation of motion for the case of constant strength point vortices. For the case of unsteady point vortices, the proposed Lagrangian agrees with the same dynamical equation derived by Brown and Michael [5]. In addition, the proposed Lagrangian allows for the integration of the equations of motion using the weak form (variational form) which was not directly applicable to the strong form (differential equation) [5].

In Chapter 3, we investigated the flutter phenomena of helicopter rotor blades in hover [10]. The blade structure is modeled as three-dimensional beam and the unsteady aerodynamics is modeled using a two-dimensional strip theory [11, 12]. The flutter analysis is performed about the equilibrium conditions which are obtained using the Newton-Raphson method. We constructed

a finite-state time approximation for the unsteady aerodynamics loads of Theordorsen [13] and Loewy's [14] strip theories. The results showed that unsteady aerodynamics have a stabilization effect at lower pitching angle [15], which was not clear in the previous work [16].

In Chapter 4, we looked at the effect of tail flexibility on the propulsive efficiency of fish-like locomotion [17]. The tail structure is modeled as a beam and the hydrodynamic loads are calculated using the unsteady vortex lattice method (UVLM) [18, 19]. The equations of motion are integrated using Newmark method [7]. The coupling between the structure and hydrodynamic loads is performed using two different methods: the under-relaxation (loose coupling), and the Newton-Raphson method (strong coupling). The latter one showed more stability to any input parameters unlike the first one. The results using a two-dimensional UVLM with an aspect ratio correction [20] indicate a slight enhancement in the propulsive efficiency with an inconsistency for the results of the active flexible cases. On the contrary, the results using a three-dimensional UVLM show a consistent improvement in the propulsive efficiency.

In Chapter 5, we examined the stability of the flapping wing micro-air vehicle (FWMAV) using Floquet theory. The results showed that the stability of hovering orbits depend on the periodic orbit, i.e. stable and unstable equilibrium exist. On the other hand, the forward flight orbit is always unstable. Furthermore, we investigated the controller design to switch between hovering and forward flight for both averaged and time-periodic dynamics. The results of the transition between these two flight conditions indicate that first-order averaged dynamics is not suitable for controller design [21].

In Chapter 6, we derived a mathematical model for psciform freely moving in a plane under the action of the coupled dynamics and hydrodynamic loading generated by both the body and tail. We extended Garrick's [22] model for an airfoil oscillating with a flap to account for the time-varying free stream [23]. We showed that the psciform is inherently stable if center of mass is ahead of the mid-point of the total length of the body and tail. If this is not the case, the equilibrium orbit of the fish is unstable and a feedback controller is needed to switch between different forward speeds. We conclude in Chapter 7 by summarizing the results in this dissertation.

Chapter 2

A Variational Approach for the Dynamics of Unsteady Point Vortices

In this chapter, we present a new Lagrangian function for the dynamics of point vortices that is more general than Chapman's [6]. We examine the relation between the proposed Lagrangian and Chapman's Lagrangian for the cases of constant strength and time-varying point vortices. Interestingly, the proposed Lagrangian dynamics of unsteady point vortices recovers the momentum based Brown-Michael model [24]. We apply the resulting dynamic model of time-varying vortices to the problem of an impulsively started flat plate as well as an accelerating and pitching flat plate, with comparison to experimental data in the literature [25, 26]. To the best of our knowledge, this is the first variational principle to govern the dynamics of unsteady point vortices.

2.1 Lagrangian Dynamics of Point Vortices

2.1.1 General Formulation

Considering the flow around a sharp-edged body (in the z-plane) and mapping it to the flow over a cylinder (in the ζ-plane) with an interrelating conformal mapping $z = z(\zeta)$, as shown in Fig. 2.1, the regularized local fluid velocity (Kirchhoff velocity) of the shed k^{th} vortex is given by [27–29]

$$\frac{dz_k}{dt} = w_k(z_k) = \frac{1}{[z'(\zeta_k)]^*} \lim_{\zeta \to \zeta_k} \left[\frac{\partial F}{\partial \zeta} - \frac{\Gamma_k}{2\pi i} \frac{1}{\zeta - \zeta_k} - \frac{\Gamma_k}{4\pi i} \frac{z''(\zeta)}{z'(\zeta)} \right]^* \tag{2.1}$$

where F is the complex potential, Γ_k is the constant strength of the kth vortex, and the asterisk refers to a complex conjugate. The last term on the right hand side, which involves the second derivative of the transformation, was first derived by Routh then by Lin [27] and later by Clements [28].
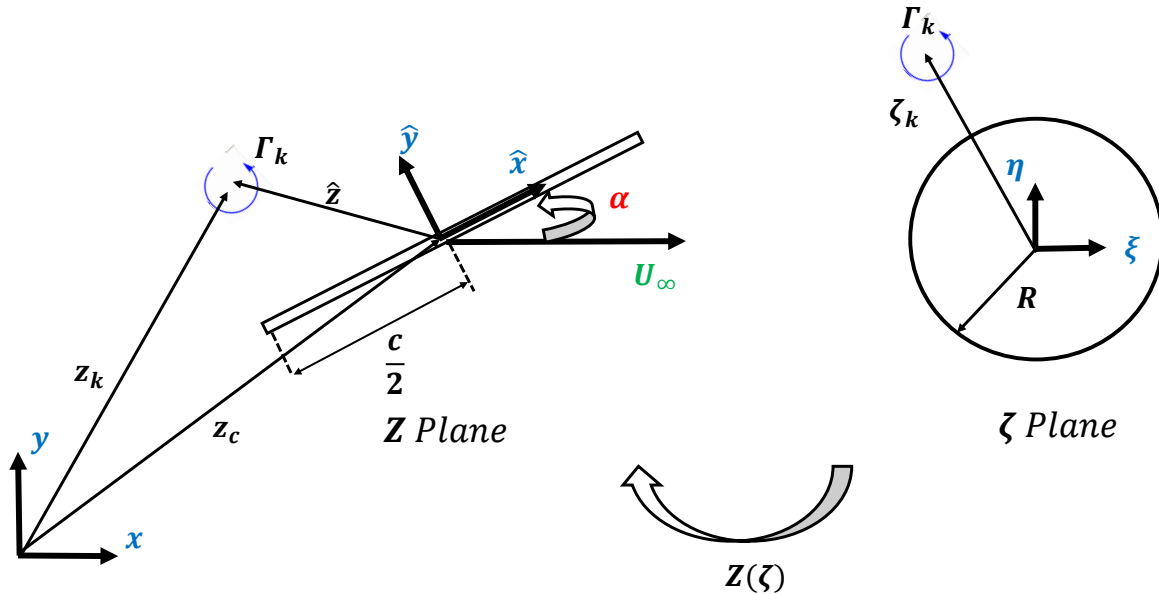
Figure 2.1: Conformal mapping between a sharp-edged body and a circular cylinder.

Lin [30] showed the existence of a Kirchhoff-Routh function W ([31, Sec.13.48]) that relates the velocity components of the kth vortex to the derivatives of W, in a Hamiltonian form, such that

$$
\begin{aligned}
\Gamma_k u_k &= \frac{\partial W}{\partial y_k} \\
\Gamma_k v_k &= -\frac{\partial W}{\partial x_k}
\end{aligned}
\tag{2.2}
$$

The Kirchhoff-Routh function $\tilde{W}$ in the circle plane is related to the stream function ψ_0 by [27, 31, 32]

$$
\tilde{W}(\xi_k, \eta_k) = \Gamma_k \psi_o(\xi_k, \eta_k) + \sum_{k,l,k \neq l} \frac{\Gamma_k \Gamma_l}{4\pi} \left[ln|\zeta_k - \zeta_l| - ln|\zeta_k - \zeta_l^I| \right] + \sum_k \frac{\Gamma_k^2}{4\pi} ln|\zeta_k - \zeta_k^{(I)}| \tag{2.3}
$$

where ψ_o is the stream function of the body motion (i.e., $F = F_0 + \sum_{k=1}^n \Gamma_k$ and $F_0 = \phi_0 + i\psi_0$). Then the relation betwen the Kirchhoff-Routh function W in the flat plate plane and that in circle plane $\tilde{W}$ is given as [27] :

$$
W = \tilde{W} + \sum_k \frac{\Gamma_k^2}{4\pi} ln|\frac{dz}{d\zeta}| \tag{2.4}
$$

It is noteworthy that, as shown by Lin [30], the term ρW is a measure of the kinetic energy, where ρ is the density of the fluid. As such, the equations of motion of constant strength vortices can be determined from an energy minimization process. More details about the Hamiltonian structure of the motion of point vortices are provided by Aref [33].

2.1.2 Proposed Lagrangian of Point Vortices

We postulate a new Lagrangian function for the motion of point vortices in an infinite fluid in the z-plane in the most basic form as

$$
L(z_k, z_k^*, \dot{z}_k, \dot{z}_k^*) = \frac{1}{i} \sum_{k=1}^n \Gamma_k z_k^* \dot{z}_k + W \tag{2.5}
$$

where the first term is the bilinear function in variables z_k and $\dot{z}_k$, and the second term is the Routh stream function

$$W = -\frac{1}{2\pi} \sum_{k,l,k \neq l} \Gamma_k \Gamma_l \ln(z_k - z_l)(z_k - z_l)^* \tag{2.6}$$

The variable z_k and its conjugate z_k^* are treated as an independent variables. The bilinear nature of the first term ensures that the resulting equations of motion will involve only time derivatives of first order. The same concept was introduced by Chapman whose Lagrangian is written as

$$\begin{aligned} L'(z_k, z_k^*, \dot{z}_k, \dot{z}_k^*) &= \frac{1}{2i} \sum_{k=1}^{n} \Gamma_k (z_k^* \dot{z}_k - z_k \dot{z}_k^*) - \frac{1}{2\pi} \sum_{k,l,k \neq l} \Gamma_k \Gamma_l ln(z_k - z_l)(z_k - z_l)^* \\ &= I_o + W \end{aligned} \tag{2.7}$$

where I_0 is one of the constants of motion associated with the motion of vortices of constant strengths in an infinite fluid. This Lagragian was then used in different contexts [34, 35].

The proposed Lagrangian L and Chapman's Lagrangian L' are related via a gauge symmetry for the case of constant-strength vortices. That is, we have

$$L' = L - \frac{1}{2i}\frac{d}{dt} \sum_{k=1}^{n} \Theta_k \tag{2.8}$$

where $\Theta_k = \Gamma_k z_k^* z_k$ is the angular momentum of the kth vortex about the origin. Note that the gauge symmetry between any two Lagrangian functions such as L and L' implies that they add up to a total time derivative of some function, i.e., we have

$$L' = L + \frac{d}{dt}[F(q,t)] \tag{2.9}$$

where q are the generalized coordinates. As such, it is said that L and L' are related by a gauge symmetry or a gauge transformation and that both are gauge invariant [1, 36].

On the other hand for the case of constant strength vortices, using Eq. (2.8), one may explain Chapman's Lagrangian L' as a constrained version of our proposed Lagrangian L to satisfy the constraint

that the total angular momentum of the vortices about origin is conserved; i.e., $\frac{d}{dt}\sum_{k=1}^{n}\Theta_k = 0$.

2.1.3 Dynamics of a Constant Strength Point Vortices

To obtain the equations of motion for the case of vortices of constant strength, we define the action to be the integral of the Lagrangian

$$S = \int_{t_1}^{t_2} L(z_k, z_k^*, \dot{z}_k, \dot{z}_k^*)dt \tag{2.10}$$

Applying the principle of least action, i.e. setting the first variation of the action integral S to zero, the corresponding Euler-Lagrange equations are written as

$$\frac{d}{dt}\left(\frac{\partial L}{\partial \dot{z}_k}\right) - \frac{\partial L}{\partial z_k} = 0 \tag{2.11}$$

which yields the Biot-Savart law [19, 31, 37] that governs the motion of point vortices and is given by

$$\dot{z}_k^* = \frac{1}{2\pi i}\sum_{k,l,k\neq l}\frac{\Gamma_k}{z_k - z_l} \tag{2.12}$$

The same result can be obtained using Chapman's Lagrangian L' [6].

2.1.4 Dynamics of Unsteady Point Vortices Interacting with a Conformal Body

For a single point vortex of constant strength Γ, the Lagrangian proposed in Eq. (2.5) is written as

$$L(z, z^*, \dot{z}, \dot{z}^*) = \frac{1}{i}\Gamma z^*\dot{z} + W(z, z^*) \tag{2.13}$$

where $W(z, z^*)$ is the Kirchhoff-Routh function, which is a measure of the instantaneous energy in the flow [30] while accounting for the presence of the body. Allowing for a time-varying vortex

strength (i.e. $\Gamma = \Gamma(t)$), a term that depends on the time rate of change of circulation (i.e. $d/dt\Gamma$) is added to ensure that the derivatives resulting from the bilinear function are coordinate-independent. As such, the Lagrangian is written as

$$L(z, z^*, \dot{z}, \dot{z}^*) = \frac{1}{i}\left(\Gamma z^* \dot{z} + \dot{\Gamma} z_0^* z\right) + W(z, z^*) \tag{2.14}$$

where z_0 is the coordinate of an arbitrary point on the body.

Now the Lagrangian of n point vortices of time-varying strengths is written as

$$L(z_k, z_k^*, \dot{z}_k, \dot{z}_k^*) = \frac{1}{i}\sum_{k=1}^{n}\left(\Gamma_k z_k^* \dot{z}_k + \dot{\Gamma}_k z_{0k}^* z_k\right) + W(z_k, z_k^*) \tag{2.15}$$

where z_{0k} is the coordinate of a reference point on the body, which is usually the coordinate of the edge from which the vortex is shed [24, 29, 38, 39].

Applying Euler-Lagrange equations (2.11) associated with minimizing the action integral based on this transformed Lagrangian (2.15), we obtain the dynamics of an unsteady point vortex as

$$\dot{z}_k + \frac{\dot{\Gamma}_k}{\Gamma_k}(z_k - z_{0k}) = \left(\frac{i}{\Gamma_k}\frac{\partial W}{\partial z_k}\right)^* \tag{2.16}$$

which reduces to the Biot-Savart law given by Eq. (2.12) if $\dot{\Gamma}$ is set to zero.

The right hand side of Eq. (2.16) can be represented in terms of the regularized local fluid velocity (Kirchoff velocity) $w^*(z_k)$, obtained from Eq. (2.1) as shown by [31], which is expressed as

$$\left(\frac{i}{\Gamma_k}\frac{\partial W}{\partial z_k}\right)^* = w^*(z_k) \tag{2.17}$$

Combining Eq. (2.16) and Eq. (2.17), we write

$$\dot{z}_k + \frac{\dot{\Gamma}_k}{\Gamma_k}(z_k - z_{0k}) = w^*(z_k) \tag{2.18}$$

which is exactly the same equation obtained by Brown and Michael [24] from a completely differ-

ent approach that was based on a linear momentum argument.

While both the proposed Lagrangian L and Chapman's L' [6] yield the exact same dynamics for constant-strength vortices, i.e. the Biot-Savart law, they yield different dynamics for unsteady point vortices. Adding a similar term to Chapman's Lagrangian L' to obtain a coordinate-independent expression for the vortex absolute velocity and minimizing the action integral based on this transformed Lagrangian, the resulting equation of motion is

$$\dot{z}_k + \frac{\dot{\Gamma}_k}{2\Gamma_k}(z_k - z_{0k}) = w^*(z_k) \tag{2.19}$$

which differs from that of Brown-Michael by the factor of one half that multiplies the $\dot{\Gamma}$-term.

Next, we apply the variational principle approach as defined above and evaluate the performance of both postulated and Chapman's [6] Lagrangians in predicting flow quantities. Particularly, we compare time histories of the circulation and lift coefficient to those obtained using the impulse matching model by Wang and Eldredge [29] and Wagner's function [40].

2.2 Impulsively Stared Flat Plate (The Starting Vortex Problem)

We consider a flat plate of semi-chord $c/2$ mapped from a circle of radius R, as shown in Fig. 2.1, according to the conformal mapping

$$z(\zeta) = z_c + g(\zeta)e^{i\alpha} \tag{2.20}$$

where the mapping function, g, is defined as

$$g(\zeta) = \zeta + \frac{R^2}{\zeta} \tag{2.21}$$

The derivative of z with respect to ζ is

$$\frac{dz}{d\zeta} = g'(\zeta)e^{i\alpha} \tag{2.22}$$

We also consider the case where the flat plate is moving with a constant speed U_∞, inclined to the x-axis by an angle α. A vortex of strength Γ_v is shed from the trailing edge as shown in Fig. 2.1. For this flow, the complex potential in the circle plane is written as [31, 32, 38]

$$F(\zeta) = \phi(\zeta) + i\psi(\zeta) = V(\zeta - g(\zeta)) + \frac{R^2\bar{V}}{\zeta} + \frac{\Gamma_v}{2\pi i}\left[ln(\zeta - \zeta_v) - ln(\zeta - \zeta_v^{(I)})\right] \tag{2.23}$$

where ϕ is the velocity potential, ψ is the stream function, $V = -U_\infty e^{i\alpha}$ is the velocity of the flat plate in the plate-fixed frame, and $\zeta_v^I = R^2/\zeta_v^*$ denotes the position of the image vortex within the circle. The first term inside the brackets $(\zeta - g(\zeta))$ ensures that the complex potential will contain only ζ with negative power (see [31, Sec. 9.63] , [37, Sec. 4.71], [32, Sec. 4], [38, Sec. 3.2]).

2.2.1   Dynamics of the Starting Vortex

Taking the origin at the mid-chord point and assuming that the starting vortex shed from the trailing edge $(\hat{z}_{v0} = -c/2)$, we write the evolution equation of the starting vortex according to the Lagrangian dynamics as

$$\begin{aligned}
\dot{z}_v + \frac{\dot{\Gamma}_v}{\beta\Gamma_v}(z_v - z_{v0}) &= \left(\frac{i}{\Gamma_v}\frac{\partial W}{\partial z_v}\right)^* \\
&= \left(\frac{i}{\Gamma_v}\frac{\partial W}{\partial \zeta_v}\left(\frac{dz}{d\zeta}\right)_{z_v}^{-1}\right)^* \\
&= w^*(z_v)
\end{aligned} \tag{2.24}$$

where β is a factor used to differentiate between the equation obtained from the proposed Lagrangian L ($\beta = 1$) or Chapman's Lagrangian L' ($\beta = 2$). The calculation of the value of Γ_v and

its time derivative will be discussed in 2.2.2. Also, we have

$$W(z_v) = \Gamma_v \psi_o + \frac{\Gamma_v^2}{4\pi} |\ln(\zeta_v - \zeta_v^{(I)})| + \frac{\Gamma_v^2}{4\pi} \ln|\frac{dz}{d\zeta}|_{z_v} \tag{2.25}$$

and

$$\psi_0 = Im\left(V(\zeta - g(\zeta)) + \frac{R^2 V^*}{\zeta}\right) \tag{2.26}$$

Transforming Eq. (2.24) to the circle plane, the first term in the left hand side is written as

$$\dot{z}_v = U_\infty + g'(\zeta_v)e^{i\alpha}\dot{\zeta}_v \tag{2.27}$$

and the right hand side of Eq. (2.24) is re-written as

$$\begin{aligned}
w^*(\zeta) &= \frac{e^{i\alpha}}{[g'(\zeta)]^*}\left[V(1 - g'(\zeta)) - \frac{R^2\bar{V}}{\zeta^2} - \frac{\Gamma_v}{2\pi i}\frac{1}{\zeta - \zeta_v^I} - \frac{\Gamma_v}{4\pi i}\frac{g''(\zeta)}{g'(\zeta)}\right]^* \\
&= \frac{e^{i\alpha}}{[g'(\zeta)]^*}\left[V - \frac{R^2\bar{V}}{\zeta^2} - \frac{\Gamma_v}{2\pi i}\frac{1}{\zeta - \zeta_v^I} - \frac{\Gamma_v}{4\pi i}\frac{g''(\zeta)}{g'(\zeta)}\right]^* - Ve^{-i\alpha}
\end{aligned} \tag{2.28}$$

Recalling that $V = -U_\infty e^{i\alpha}$, we write

$$w^*(\zeta) = \frac{e^{i\alpha}}{[g'(\zeta)]^*}\left[V - \frac{R^2\bar{V}}{\zeta^2} - \frac{\Gamma_v}{2\pi i}\frac{1}{\zeta - \zeta_v^I} - \frac{\Gamma_v}{4\pi i}\frac{g''(\zeta)}{g'(\zeta)}\right]^* + U_\infty \tag{2.29}$$

The evolution equation is then re-written in terms of the circle-plane variables as

$$\dot{\zeta}_v + \frac{\dot{\Gamma}_v}{\beta\Gamma_v}\frac{(g(\zeta_v) - 2R)}{g'(\zeta_v)} = \frac{1}{g'(\zeta_v)[g'(\zeta_v)]^*}\left[V - \frac{R^2\bar{V}}{\zeta_v^2} - \frac{\Gamma}{2\pi i}\frac{1}{\zeta_v - \zeta_v^I} - \frac{\Gamma_v}{4\pi i}\frac{g''(\zeta_v)}{g'(\zeta_v)}\right]^* \tag{2.30}$$

A more general form of Eq. (2.30), for $\beta = 1$, for a flat plate moving and rotating in space can be found in the work of Michelin and Smith [38], which will be used, without derivation, for the case of pitching flat plate.

2.2.2 Aerodynamic Forces
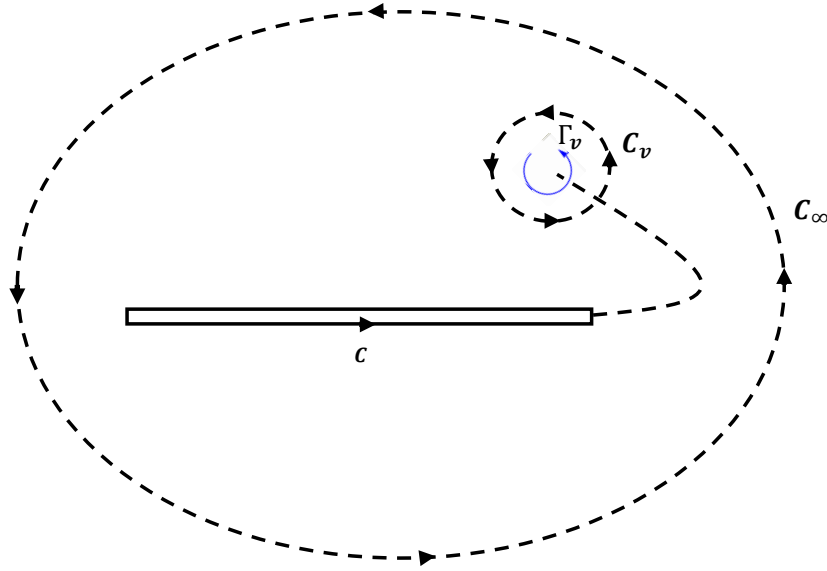
Figure 2.2: The contour used to evaluate the integral on the solid body. The flat plate is exaggerated to show the direction of the contour

The force on the flat plate is obtained using the force formula derived by Sedov [41], in terms of the complex variable z, as

$$F_x + iF_y = -i\rho z_o \frac{d\Gamma_v}{dt} + \overline{\frac{i\rho}{2} \int_C [w(z)]^2 dz} + \frac{d}{dt}\left[i\rho \int_C zw(z)dz \right] \tag{2.31}$$

Using Cauchy's theorem [42], the integration can be changed from an integration over the solid body C to an integration over the infinite domain C_∞ that excludes the integration over an infinitesimally small contour C_v around the vortex (see [38, Sec.3.4.1]) as shown in Fig. 2.2. Upon evaluating the integration, the force in terms of the complex variable ζ becomes

$$F_x + iF_y = i\rho e^{i\alpha}\left[2i\pi R^2 Im(V) + \frac{d}{dt}\left(\Gamma_v(\zeta_v - \frac{R^2}{\bar{\zeta}_v}) \right) \right] \tag{2.32}$$

The vortex strength Γ_v is calculated by satisfying the Kutta condition at each time instant. The

Kutta condition is implemented by requiring that the tangential velocity at the trailing edge in the circle plane vanishes; i.e., the terms inside the brackets in Eq. (2.30) are set to zero at the trailing edge to cancel the singularity due to $1 - R^2/\zeta_{v0}^2 = 0$. This will ensure a finite velocity at the trailing edge. As such, we write

$$V - \frac{R^2 \bar{V}}{\zeta_0^2} + \frac{\Gamma_v}{2\pi i}\left(\frac{1}{\zeta_0 - \zeta_v} - \frac{1}{\zeta_0 - \zeta_v^I}\right) = 0 \tag{2.33}$$

Equation (2.33) is then re-written as

$$2iIm(V) + \frac{\Gamma_v}{2\pi i}\left(\frac{-R^2 + (\eta_v + \xi_v)^2}{2(\eta_v^2 + (\xi_v - 2)^2)}\right) = 0 \tag{2.34}$$

where ξ_v and η_v are the real and imaginary parts of ζ_v.

By simple manipulation, Eq. (2.34) is re-written in a simple form as [29, 38]

$$2Im(V) + \frac{\Gamma_v}{2\pi}Re\left(\frac{\zeta_{v0} + R}{\zeta_{v0} - R}\right) = 0 \tag{2.35}$$

Equation (2.35) is used to calucalte the value of Γ_v and its time derivative $\dot{\Gamma}_v$. For the force calculations using the impulse of the starting vortex, the reader is referred to section 3.10 of Ref. [43].

2.3   Numerical Results

Two types of airfoil motion are considered in this section: (i) an impulsively started motion in which the airfoil is suddenly accelerated to velocity U_∞, (ii) a finite acceleration from rest to reach U_∞ after some non-zero but finite time, and (iii) and the vortex generated by a pitching plate. For integrating the equations of motion, we used the Matlab solver **ode15s** with a fixed time step of $\Delta t = 10^{-5}c/U_\infty$. This solver shows a better and stable performance than others because of the stiff nature of the evolution equation. For the first time step, instead of integrating the equations

of motion analytically along with the Kutta condition as in Refs [38, 44], we used an appropriate initial condition for the position of the vortex , i.e. $x(0) = c/2 + \epsilon$, where $\epsilon \approx 10^{-4} c$.

2.3.1 Impulsively Started Flat Plate

First, similar to the classical unsteady thin airfoil theory (e.g., Wagner [40], Theodorsen [13], and Von Karman and Sears [45]), we assume that the starting vortex moves along the x-axis and the local fluid velocity is U_∞ (i.e., $w(z_v) = U_\infty$). As such, the evolution equation (2.24) in the z plane is written as

$$\dot{x}_v + \frac{\dot{\Gamma}_v}{\beta \Gamma_v}(x_v - x_{v0}) = U_\infty \tag{2.36}$$

The evolution equation of the impulse matching model [29, 39] can also be simplified to

$$\dot{x}_v + \frac{\dot{\Gamma}_v}{\Gamma_v}\frac{(x_v^2 - x_{v0}^2)}{x_v} = U_\infty \tag{2.37}$$

Figure 2.3 shows the time variations of the normalized vortex strength Γ_v, the lift coefficient C_L, and the time-variation of the normalized vortex location x_v for the case of $\alpha = 5^o$. Plots from simulations based on (i) the proposed Lagrangian dynamics ($\beta = 1$ Brown-Michael), (ii) Chapman's Lagrangian ($\beta = 2$), (iii) the impulse matching model of Wang and Eldredge [29], and (iv) Wagner's [40] step response function are presented for the sake of comparison. The impulse matching results are more relatively a close to the Wagner's one.
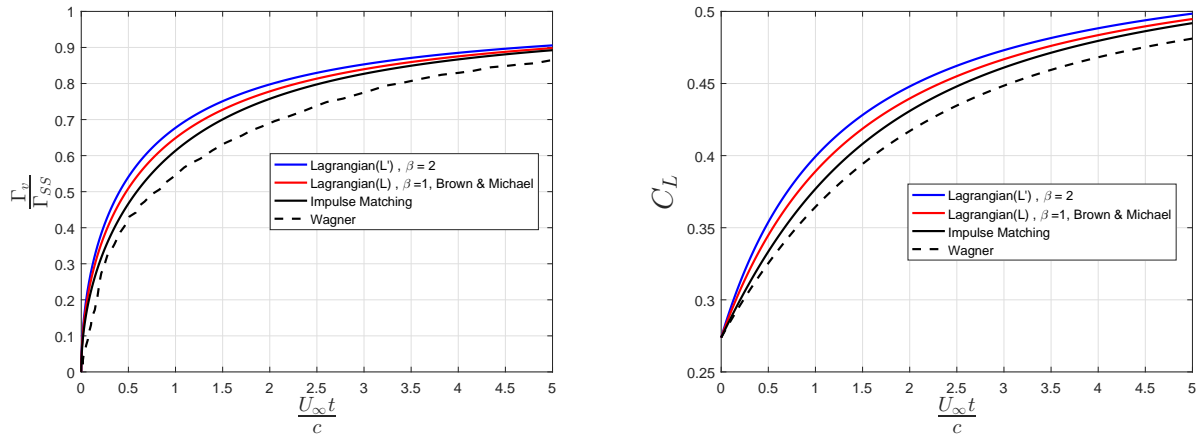
(a) Time variation of the normalized vortex strength Γ_v. The circulation is normalized with the steady-state value Γ_{SS}.

(b) Time variation of the lift coefficient C_L
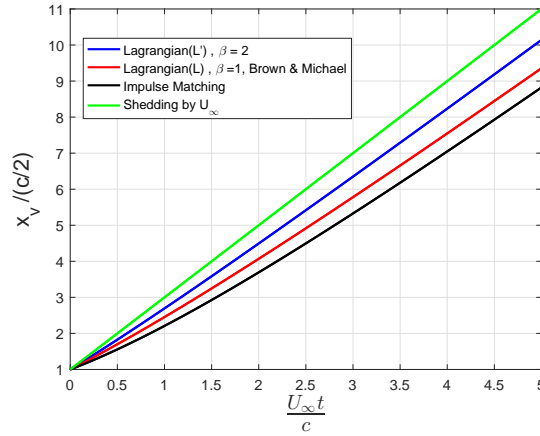
(c) Time variation of the normalized vortex position x_v. The position is normalized using the semi-chord of the airfoil.

Figure 2.3: Time variations of (a) the normalized circulation, (b) lift coefficient and (c) normalized position of the starting vortex for $\alpha = 5^o$ and the vortex is assumed to move only in the x direction. The time is normalized using the airfoil speed U_∞ and chord c.

The plots show that all models agree qualitatively with Wagner's exact potential flow solution. Note that in the three models, the infinite sheet of wake vorticity is approximated by a single vortex. As expected, the correction to the Kirchhoff velocity (taken as U_∞ here) in the case of $\beta = 2$ is half of that in the case of $\beta = 1$ yields slightly higher (spurious) lift.

Next, we consider increasing the angle of attack to $\alpha = 10°$ to relax the flat wake assumption, thus the vortex moves in the plane, i.e. with two degrees of freedom. Figure 2.4 shows the resulting time variations of the normalized circulation Γ_v, lift coefficient C_L, vortex position along the x_v-axis, and the slope of the vortex trajectory θ_v as a function of x_v. The singular value of the lift at $t = 0$, which corresponds to the added mass effect, is removed to highlight the difference between results from different models. Again, the results based on L' ($\beta = 2$) predict a larger vortex strength (airfoil circulation) and a slightly higher lift, than those predicted by the two other models. Figure 2.4d shows that the slope of the starting vortex asymptotically approaches a line parallel to the incident free stream (i.e. $\theta_v \approx \alpha = 10^o$). As shown, the proposed Lagrangian (Brown-Michael model) yield lift and circulation values that do no match Wagner's function. In addition, the impulse matching results in a slower downstream convection. Consequently the development of circulation takes place at a slower rate with an overall effect of reduced lift coefficient that matches Wagner's function. We note, however, that the Wagner's response should not be considered as a reference for comparison in this case because of the flat-wake and shedding by U_∞ assumptions that may not be appropriate for the relatively large angle of attack. This can be seen from the high-fidelity results in Fig. 2.4b as the lift starts to disagree with Wagner's function after non-dimensional time of $U_\infty t/c > 1.2$. The high-fidelity results were produced in Ref.[29] using the viscous vortex particle method developed by Eldredge [46].
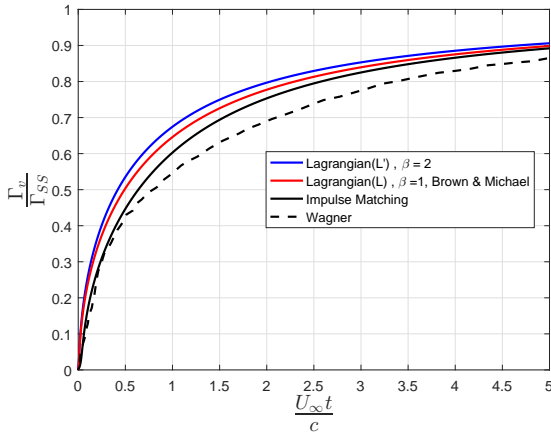
(a) Time variation of the normalized vortex strength Γ_v. The circulation is normalized with the steady-state value Γ_{SS}
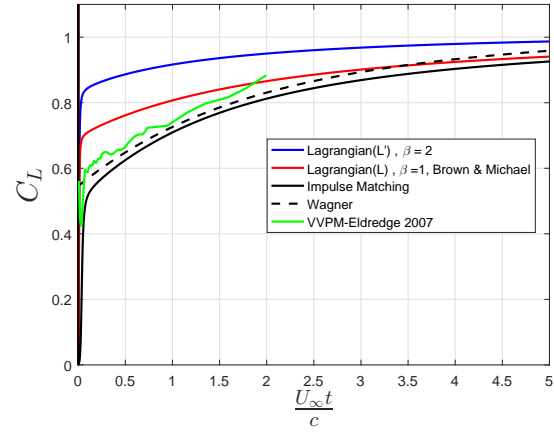
(b) Time variation of the lift coefficient C_L
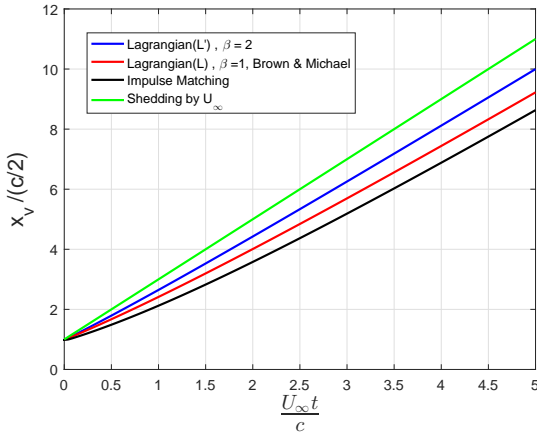
(c) Vortex position x_v versus non-dimensional time
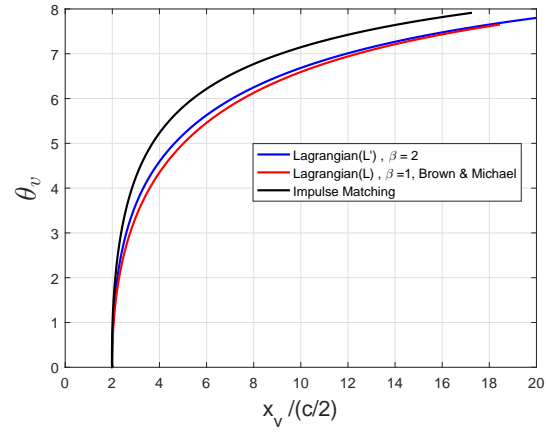
(d) Slope of the vortex trajectory θ_v versus vortex position x_v

Figure 2.4: Time variations of (a) the normalized circulation, (b) lift coefficient, (c) normalized position of the starting vortex, and the slope of the vortex trajectory for $\alpha = 10^o$ and the vortex is allowed to move freely in the plane of the airfoil. The time is normalized using the airfoil speed U_∞ and chord c.

2.3.2 Flat Plate Accelerating from Rest

Next, we consider the lift on a flat plate that accelerates from rest. To validate our results, we consider the velocity profile of Beckwith and Babinsky [25] that is shown in Fig. 2.5. In that

experiment, the airfoil is accelerated to the velocity $U_\infty = 0.48\ m/s$ over a distance of 0.6 chords.
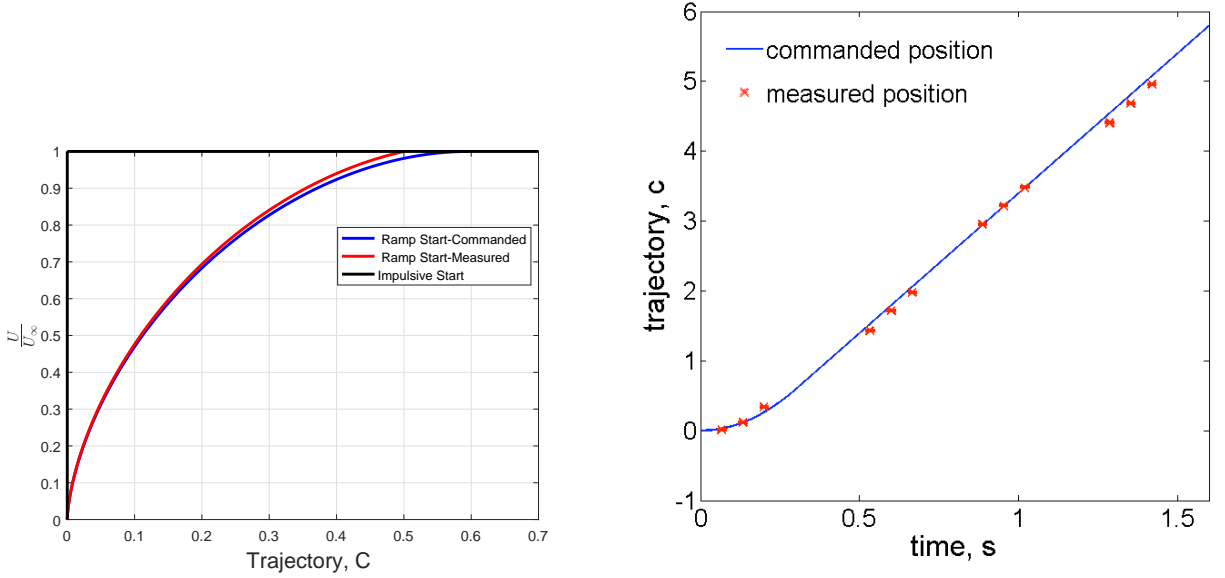
(a) Velocity profiles for the accelerated airofoil-Beckwith and Babinsky[25]

(b) Commanded and actual trajectory profile for the airofoil motion-Beckwith and Babinsky [25]

Figure 2.5: Kinematics for the accelerated flat plate

The velocity profile of the accelerated flat plate, shown in Fig. 2.5a, is obtained from the data of Beckwith and Babinsky [25] via the following optimization problem

$$\min_{P_m} \sum_{i=1}^{N} \left(X_i - \sum_{0}^{m} (P_m t^m) \right) \tag{2.38}$$

subject to the end constraints

$$\dot{X}_P(0) = 0, \quad \dot{X}_P(t_f) = U_\infty, \quad \text{and} \quad \ddot{X}_P(t_f) = 0 \tag{2.39}$$

where $X_P = \sum_{0}^{m} P_m t^m$ represents the polynomial fit to the given data, N is the number of sample points ($X_i's$) taken from Fig. 2.5b in Ref. [25] by Beckwith and Babinsky, and m is the degree of the fitting polynomial. We used the **fmincon** Matlab function for solving the constrained optimization problem defined above. The resulting equation for the commanded and the measured

positions respectively are

$$
\begin{aligned}
X_C(t) &= -8.7540t^4 + 5.3376t^3 - 0.0265t^2 + 0.004 \\
X_M(t) &= -8.3073t^4 + 5.0119t^3 + 0.0233t^2 - 0.0002t + 0.004
\end{aligned}
\tag{2.40}
$$

Because few number of "measured data" points were available for fitting, we present results for both maneuvers; commanded and measured. In addition, we use the extended lifting line theory [20] to account for three-dimensional effects on the lift which implies a correction factor of 0.618 based on aspect ratio $A\!R = 4$.

Figure 2.6 shows time variations of the normalized circulation and lift coefficient for a flat plate accelerating from rest using both commanded and measured fits of the velocity profile. The plots show agreement among all representations except that the predicted circulation and lift based on Chapman's Lagrangian [6] is slightly higher and shows faster convergence to the steady state value. The lift coefficient shows that the proposed Lagrangian (Brown-Michael equation) yields values that are closer to the experimental data of Beckwith and Babinsky [25] than both Chapman's Lagrangian ($\beta = 2$) and the impulse matching model of Wang and Eldredge [29], particularly in capturing the transient peak. The large overshoot in the lift coefficient for $\beta = 2$ indicates that the exclusion of the symmetry term (angular momentum constraint) is necessary to satisfy the linear momentum around the vortex and the branch cut in an integral sense. In other words, the evolution equation based on the Lagrangian L' violates the conservation of linear momentum around the vortex and the shedding edge. Hence, the proposed Lagrangian L is a more general (unconstrained) Lagrangian of point vortices. It governs the dynamics of both vortices of constant and time-varying strengths.
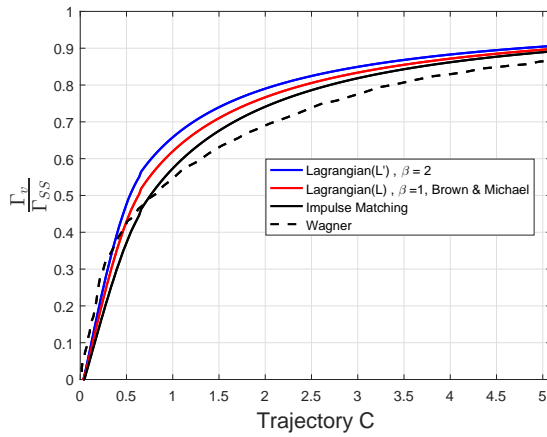
(a) Time variation of the normalized vortex strength Γ_v for the *commanded* position. The circulation is normalized with the steady-state value Γ_{SS}
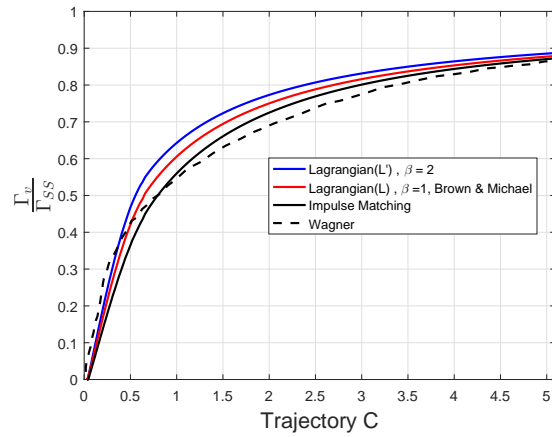
(b) Time variation of the normalized vortex strength Γ_v for the *measured* position. The circulation is normalized with the steady-state value Γ_{SS}
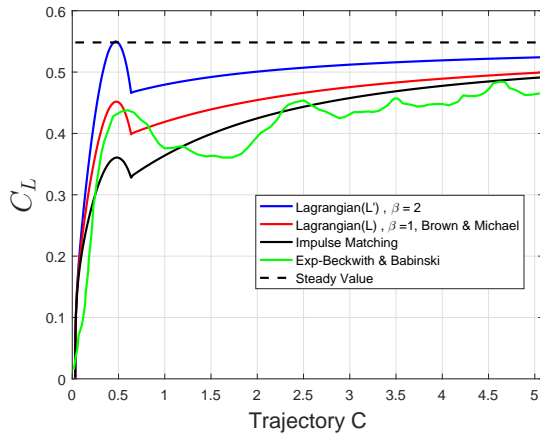
(c) Time variation of the normalized lift coefficient C_L for the *commanded* position
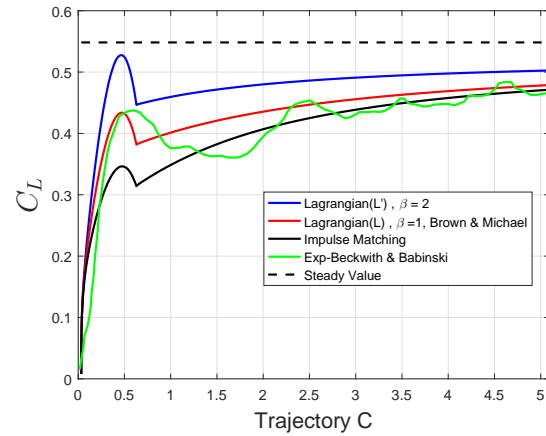
(d) Time variation of the normalized lift coefficient C_Le for the *measured* position

Figure 2.6: Time variations of the normalized circulation and lift coefficient for $\alpha = 5^o$ for the accelerated flat plate

2.3.3 Pitching Flat Plate

In Figure 2.7, the lift coefficient versus angle of attack is shown for an airfoil pitching at a reduced frequency $k = 0.2$, and compared to the experiment carried out by Granlund et al. [26] at Reynolds number $Re = 20,000$. In this case, two vortices are shed from the leading and trailing edges. The

same trend as in the case of the starting vortex is noted. Moreover, the difference is maximum when the angle of attack reaches 45° and approaches zero when the angle of attack reaches 90°. We also noted that while both proposed and Chapman's Lagrangian yielded similar dynamics for the case of the starting vortex, they yielded different dynamics for the case of pitching flat plate. Although the proposed Lagrangian (Brown-Michael) yielded a better agreement with the experimental results than Chapman's Lagrangian, the impulse matching results have a better agreement with the experiment unlike the accelerating flat plate problem.

It should be pointed out that the present work is not favoring Brown-Michael model over El-dredge's impulse matching model or vice versa. The main outcome of this work is to provide a variational formulation for the dynamics of unsteady point vortices, which interestingly matches the momentum-based formulation of Brown and Michael. However, Wang and Eldredge [29] pointed out that either model alone is not sufficient for developing reduced-order models of two-dimensional unsteady aerodynamics. The Brown-Michael model (or equivalently its present variational version) or the impulse matching model represents only one part in the whole formulation that also includes a shedding criterion and an auxiliary condition (Kutta-like condition). So, the superiority of the Brown-Michael model and its variational version in predicting the lift in the accelerating plate case does not imply a true superiority and vice versa. To reflect more on the issues discussed in this paper, future work is recommended for other kinematics problems such as perching and plunging motions, and verifying them against experimental data [26, 47, 48]
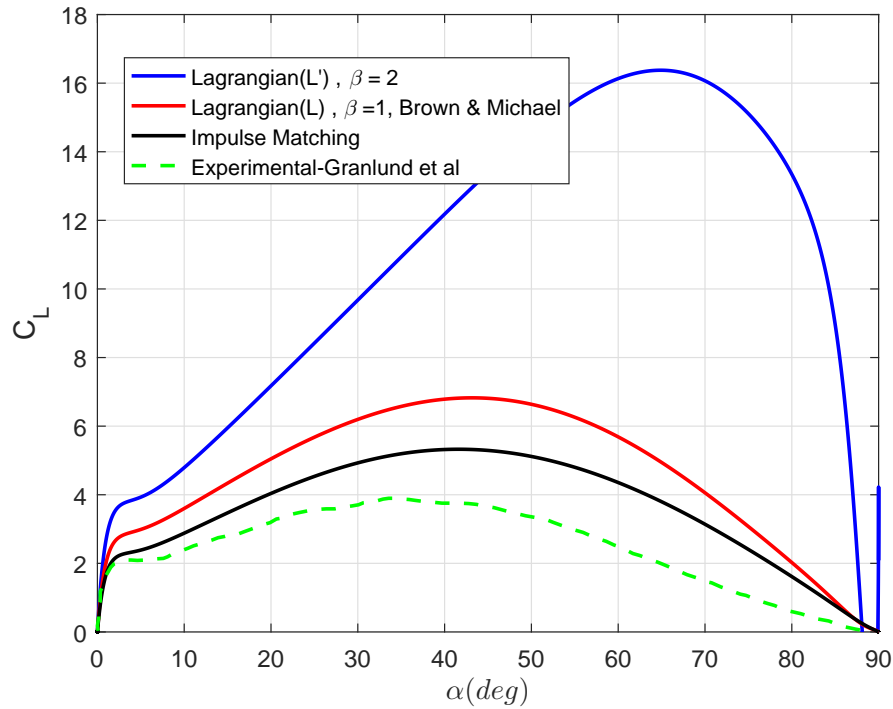
Figure 2.7: Lift coefficient versus angle of attack for pitching airfoil at reduced frequency $k = 0.2$ and Reynolds number $Re = 20,000$.

2.4 Conclusions

We investigated the potential of implementing variational principle to derive governing equations for the interaction of unsteady point vortices with a solid boundary. To do so, we postulated a new Lagrangian function for the dynamics of point vortices that is more general than Chapman's. We showed that this function is related to Chapman's Lagrangian via a gauge symmetry for the case of constant-strength vortices. In other words, both Lagrangian functions result in the same steady governing equation, i.e. the Biot-Savart law is directly recovered from the Euler-Lagrange equations corresponding to minimization of the action integral with these two Lagrangians. We also found that, unlike Chapman's Lagrangian, the principle of least action based on the proposed Lagrangian results exactly in the Brown-Michael model for the dynamics of unsteady point vor-

tices. We implemented the resulting dynamic model of time-varying vortices to the problem of an impulsively started flat plate as well as an accelerating and pitching flat plate. For the case of an accelerating flat plate, the resulting time history of the lift coefficient from the three models (variational based approach for the proposed Lagrangian and Chapman's, and the impulse matching model) was compared against the experimental results of Beckwith and Babinsky. The results showed a better agreement for the variation approach using the proposed Lagrangian. On the other hand, the results of the impulse matching model for the pitching flat plat agree better with experimental results than the those based on Chapmann's and the proposed Lagrangian (Brown-Michael model).

Chapter 3

Dynamic Stability of a Hingeless Rotor Blade in Hover using Padé Approximations

In this chapter, we aimed to examine the sensitivity of using different finite-state aerodynamic models on the flutter boundary of a helicopter rotor blade in hover. To achieve this goal, a set of time-domain approximations for the deficiency function $C'(k, m, h)$ are used. The flutter solution is obtained by assuming the deflections to be equal to a small perturbation about the nonlinear equilibrium deflections. The deficiency function $C'(k, m, h)$ is represented in terms of Laplace operator $\bar{s}$ in order to represent the aerodynamic loads in a state space form. Three different approximations for $C'(k, m, h)$ were used. The first one is Jones' [49] approximation, the second is obtained using Dowell's [50] method and the third is based on general nonlinear least square fitting for $C'(k, m, h)$ [51] obtained by imposing zero and infinite frequency limits and nonnegative poles constraints. The final results show a very good agreement with those obtained using numerical simulation models of the helical wake.

3.1 Analysis

3.1.1 Aerodynamic Model

The expressions for the aerodynamic lift and pitching moment per unit span acting on the blade cross section are calculated using Greenberg's [52] extension of Theodorsen's theory for a two-dimensional airfoil. This extension mainly accounts for the pulsating free stream velocity seen by blade cross-section. Figure 3.1 shows the coordinate system of the deformed blade and a section of the rotor blade undergoing general unsteady motion of pitching $\varepsilon(t)$, plunging $\dot{h}(t)$ and pulsating free stream motions.

(a) Coordinate system of the deformed rotor blade

(b) Unsteady forces and motions of rotor blade cross section
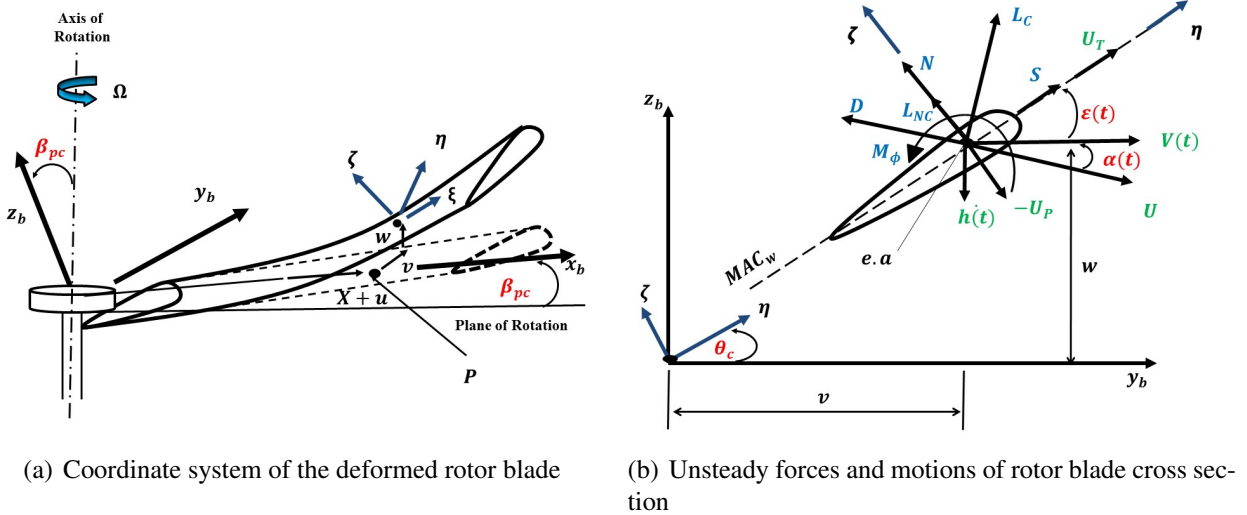
Figure 3.1: Coordinate system and aerodynamic forces acting on a rotating blade undergoing plunging, pitching and pulsating motions

Assuming a small angle of attack, a small pitching angle and $\frac{U_P}{U_T} \ll 1$, the expression for the aerodynamic loads L_w and L_v in the w and v direction respectively and the pitching moment M_ϕ

about ξ are written as [53, 54]:

$$
\begin{aligned}
L_v &= \rho a_o b[-\Omega X V_i(\phi + \theta_c) + V_i^2 + 2V_i \dot{w} - \Omega X(\phi + \theta_c)\dot{w} - V_i\dot{v}(\phi + \theta_c)]C(k) \\
&\quad + \frac{\rho b C_{D_o}}{2}[\Omega^2 X^2 + 2\Omega X \dot{v}] \\
L_w &= \rho a_o b[\Omega^2 X^2(\phi + \theta_c - \int_0^x v''w'dx) + 2\Omega X(\phi + \theta_c)\dot{v} - \Omega X V_i - \Omega X \dot{w} - V_i\dot{v} - \Omega^2 Xv(\beta_{pc} + w') \\
&\quad + \Omega^2 X(\beta_{pc} + w')b(\frac{1}{2} - a) + \Omega X \dot{\phi} b(\frac{1}{2} - a)]C(k) \\
&\quad + \frac{\rho b^2 a_o}{2}[-\ddot{w} + \Omega X \dot{\phi} - ba\ddot{\phi}] \\
M_\phi &= \rho a_o b^2(\frac{1}{2} + a)[\Omega^2 X^2(\phi + \theta_c) + 2\Omega X(\phi + \theta_c)\dot{v} - \Omega X V_i - \Omega X \dot{w} - \Omega^2 X \dot{w} \\
&\quad - \Omega^2 Xv(\beta_{pc} + w') - V_i\dot{v} + b(\frac{1}{2} - a)\Omega^2 X(\beta_{pc} + w') + b(\frac{1}{2} - a)\Omega X \dot{\phi}]C(k) \\
&\quad + \frac{\rho b^3 a_o}{2}[(a - \frac{1}{2})\Omega X \dot{\phi} - a\ddot{w} - b(\frac{1}{8} + a^2)\ddot{\phi} - \frac{1}{2}\Omega^2 X(\beta_{pc} + w')]
\end{aligned}
$$

$$(3.1)$$

where $C(k)$ denotes a general deficiency function [55].

3.1.2 Padé Approximations for the lift deficiency function

Loewy's [12] lift deficiency function, $C'(k, \bar{m}_e, \bar{h}_e)$, for collective mode case is given by [55] :

$$
C'(k, \bar{m}_e, \bar{h}_e) = \frac{H_1^{(2)}(k) + 2J_1(k)W(k, \bar{h}_e, \bar{m}_e)}{H_1^{(2)}(k) + iH_0^{(2)}(k) + 2[J_1(k) + J_0(k)]W(k, \bar{m}_e, \bar{h}_e)} = F'(k, \bar{m}_e, \bar{h}_e) + iG'(k, \bar{m}_e, \bar{h}_e)
$$

$$(3.2)$$

where $H_n^{(2)}$ is the Hankel function of the second type and J_n is the Bessel function of the first type evaluated at the local reduced frequency k. $W(k, \bar{m}_e, \bar{h}_e)$ is a weighting function used to account for the vorticity shed by previous blades or revolutions. It is given by :

$$
\begin{aligned}
W(k\bar{h}_e, \bar{m}_e) &= \frac{1}{e^{k\bar{h}_e}e^{2\pi i \bar{m}_e} - 1} \quad , \quad k > 0 \\
&= \quad 0 \quad\quad , \quad k = 0
\end{aligned}
$$

$$(3.3)$$

where $\bar{m}_e$ and $\bar{h}_e$ are the frequency and wake spacing respectively normalized with respect to the number of blades, i.e.

$$\bar{m}_e = \frac{\omega}{\Omega \ N_b} = \frac{\omega \ c/2}{\Omega \ r} \ \frac{r}{c/2} \ \frac{1}{N_b} = k\frac{\bar{r}}{\bar{c}/2 \ N_b} = k\bar{r}_e$$
$$\bar{h}_e = \frac{4\lambda_i}{\sigma}$$

(3.4)

Next, we find an approximation, $C_A = F_A + iG_A$, for $C'(k, \bar{m}_e, \bar{h}_e)$ in terms of $\bar{s}$. The first approximation is obtained by using Dowell's method [50] assuming C_A to be a rational function given as $C_A = \sum_{i=1}^{I} \frac{ika_i}{-b_i+ik}$. The method invokes the formulation of a least-squares problem as follows : $\min_{x} \sum_{j=1}^{N_p} |G'(i) - G_A(i)|^2$ subjected to $a_1 + a_2 + a_3 + ... = F'(\infty) = 1/2$, where the imaginary part and the zero frequency value are respectively defined as $G_A = -\sum_{i=1}^{I} \frac{a_ik^2}{b_i^2+k^2}$, $a_1 = F'(0)$.

Although Dowell's method is more accurate than Jones', it cannot capture the high oscillatory nature of Loewy's deficiency function as concluded by Dinyavari and Freidmann[55]. So, there is a need for a more general approximation. The second approximation presented here is obtained by imposing a general rational function with no further choice or enforcing the pole values [51]. The optimization problem is then modified in comparison to that of Ref. [51] as it is subjected to the constraint of nonnegative poles. This modification is important as the results obtained in Ref. [56] by using the model of Ref. [51] indicated that the problem posed without a constraint is not guaranteed to represent a stable flow,i.e. half of the poles are unstable. In other words, the aeroelastic system cannot be represented by a state-space model since part of the poles are already in the right-half plane.

The rational function defined herein is given as :

$$C_A = \sum_{i=0}^{I} \frac{b_i\bar{s}^i}{a_i\bar{s}^i}$$

(3.5)

The optimization problem whose objective is minimizing the square error of the magnitude and

phase is defined as follows :

$$\min_{x} \sum_{j=1}^{N_p} \left(|C'(j)| - |C_A(j)| \right)^2 + \sum_{j=1}^{N_p} \left(|\phi'(j) - \phi_A(j)| \right)^2 \qquad (3.6)$$

subjected to :

$$\frac{b_0}{a_0} - 1 = 0$$
$$\frac{b_I}{a_I} - 0.5 = 0 \qquad (3.7)$$
$$Re[\lambda_i(\sum_{i=1}^{I} a_i \bar{s}^i)] < 0, i = 0...I$$

where $|C'(j)|, \phi'(j)$ and $|C_A(j)|, \phi_A(j)$ are respectively the magnitudes and the phases of Loewy's and approximation functions. The vector of the design variables is denoted by x ; $x = b_i, ...b_0, ai, ...a_0$. The first and second constraints are imposed to satisfy unity value of C_A as the frequency k goes to zero and $1/2$ as the frequency approaches infinity. The third inequality constraint is introduced to ensure that the resulting approximation will represent a stable flow, i.e. no instability occurs. In other words, it has no meaning to examine the instability of our dynamical system if we introduce the approximation with unstable poles. This constraint was not utilized in Ref. [56] as the roots of the denominator had unstable poles. However, it perfectly fitted the exact function.

3.1.3 Structure Model

The static deformation equations are based on the model of Hodges and Dowell [53]. The blade before and after deformation is shown in Fig. 3.1. The strain energy is given by :

$$U = \int_V \frac{E}{2} (\epsilon_{xx})^2 dV + \int_V \frac{G}{2} [(\epsilon_{x\eta})^2 + (\epsilon_{x\zeta})^2] dV \qquad (3.8)$$

The equations of motion are then derived by applying Hamilton's principle [16, 57].

$$\int_{t_1}^{t_2} (\delta U - \delta T - \delta W)dt = 0 \tag{3.9}$$

Where δU, δT and δW the variations of the strain energy, kinetic energy and virtual work of external force. These variations are written as :

$$\delta U = \int_0^R \left(\int_A [\epsilon_{xx}\delta\epsilon_{xx} + \epsilon_{x\eta}\delta\epsilon_{x\eta} + \epsilon_{x\zeta}\delta\epsilon_{x\zeta}]d\eta d\zeta \right) dx \tag{3.10}$$

$$\delta T = \int_0^R \left(\int_A \rho\delta\vec{\mathbf{V}}.\vec{\mathbf{V}} \right) dA \tag{3.11}$$

$$\delta W = \int_0^R \left(L_v\delta v + L_w\delta w + M_\phi\delta\phi \right) dx \tag{3.12}$$

The expressions for the strains and velocity vector $\vec{\mathbf{V}}$ are given by

$$\epsilon_{xx} = u' + \frac{1}{2}v'^2 + \frac{1}{2}w'^2 - w''[\eta sin(\theta_c+\phi)+\zeta cos(\theta_c+\phi)] - v''[\eta cos(\theta_c+\phi)-\zeta sin(\theta_c+\phi)] + \frac{1}{2}[(\zeta)^2+(\eta)^2]\phi^2 \tag{3.13}$$

$$\epsilon_{x\eta} = -(\zeta + \frac{\partial\lambda}{\partial\eta})\phi' = -\hat{\zeta}\phi' \tag{3.14}$$

$$\epsilon_{x\zeta} = (\eta - \frac{\partial\lambda}{\partial\zeta})\phi' = \hat{\eta}\phi' \tag{3.15}$$

For small twist angle ϕ, $\vec{r}_p$ and $\vec{V}$ can be written as :

$$\vec{r}_p \approx (X + u)\hat{\boldsymbol{i}}_b + [v + \eta\{cos\theta_c - \phi sin\theta_c\} - \zeta\{sin\theta_c + \phi cos\theta_c\}]\hat{\boldsymbol{j}}_b$$

$$+ [w + \eta\{sin\theta_c + \phi cos\theta_c\} + \zeta\{cos\theta_c - \phi sin\theta_c\}]\hat{\boldsymbol{k}}_b$$

$$\vec{\mathbf{V}} = \frac{d\vec{\mathbf{r}_p}}{dt} = \frac{\partial\vec{\mathbf{r}_p}}{\partial t} + \vec{\omega}_b \times \vec{\mathbf{r}_p} = \frac{\partial\vec{\mathbf{r}_p}}{\partial t} + \left(\Omega sin\beta_{pc}\hat{\boldsymbol{i}}_b + \Omega cos\beta_{pc}\hat{\boldsymbol{k}}_b\right) \times \vec{\mathbf{r}_p} \qquad (3.16)$$

$$\approx \left(\dot{u} - \Omega v\right)\hat{\boldsymbol{i}}_b + \left((X + u)\Omega + \dot{v} - (\eta sin(\theta_c) + \zeta cos(\theta_c))\dot{\phi}\right)\hat{\boldsymbol{j}}_b$$

$$+ \left(\Omega\beta_{pc}v + \dot{w} + (\eta cos(\theta_c) - \zeta sin(\theta_c))\dot{\phi}\right)\hat{\boldsymbol{ks}}_b$$

3.1.4 Finite State Aeroelastic Model

In order to obtain the equations of motion in matrix form, the finite element approach was applied to Hamilton's principle (3.5). The resulting equations are nonlinear time varying equations of the form:

$$[\mathbf{M}]\{\ddot{\mathbf{q}}\} + [\mathbf{D}_1(\mathbf{q})]C'(k, \bar{m}_e, \bar{h}_e)\{\dot{\mathbf{q}}\} + [\mathbf{D}_2(\mathbf{q})]\{\dot{\mathbf{q}}\} + [\mathbf{K}(\mathbf{q})]\{\mathbf{q}\} + [\mathbf{K}_S(\mathbf{q})]\{\mathbf{q}\}C'(k, \bar{m}_e, \bar{h}_e) = \{\mathbf{F}\}$$

$$(3.17)$$

Where $[\mathbf{M}]$ is the mass matrix ,$[\mathbf{D}_1(\mathbf{q})]$ and $[\mathbf{D}_2(\mathbf{q})]$ are the damping matrices, $[\mathbf{K}_S(\mathbf{q})]$ and $[\mathbf{K}(\mathbf{q})]$ are the stiffness matrices, and $\{\mathbf{F}\}$ is the steady force vector containing terms that are independent of the nodal degrees of freedom $\mathbf{q}$. Hermite polynomials are used to represent the distribution of $\mathbf{q}$ over one element [16, 16] with five degrees of freedom at each node; two bending deflections, two slope defelctions and one twist angle.

The detailed expressions of $\mathbf{M}$, $\mathbf{D}_1$, $\mathbf{D}_2$, $\mathbf{K}$, $\mathbf{K}_S$ and $\mathbf{F}$ are given in Appendix A.1. In order to investigate the dynamic stability, the equilibrium conditions have to be determined first. Dropping the time dependent terms, the trim equations are

$$[\mathbf{K}(\mathbf{q}_0) + \mathbf{K}_S(\mathbf{q}_0)]\{\mathbf{q}_0\} = \{\mathbf{F}\} \qquad (3.18)$$

The solution of Eq. (3.18) is calculated using Newton-Raphson method. The initial solution is taken to be the linear one [16]. The divergence boundary is obtained for a certain blade configuration, when the determinant of the Jacobian of Eq. (3.18) is set equal to zero [54], i.e. $|J| = |\frac{\partial \{\mathbf{K}(\mathbf{q}).\mathbf{q} + \mathbf{K}_S(\mathbf{q}).\mathbf{q}\}}{\partial \mathbf{q}}| = 0$. The linearized dynamic equations of motion are obtained by assuming that $\mathbf{q}(t) = \mathbf{q}_0 + \tilde{\mathbf{q}}$:

$$[\mathbf{M}]\{\ddot{\tilde{\mathbf{q}}}\} + [\mathbf{D}_1(\mathbf{q}_0)]C'(k, \bar{m}_e, \bar{h}_e)\{\dot{\tilde{\mathbf{q}}}\} + [\mathbf{D}_2(\mathbf{q}_0)]\{\dot{\tilde{\mathbf{q}}}\} + [\mathbf{K}(\mathbf{q}_0)]\{\tilde{\mathbf{q}}\} + [\mathbf{K}_S(\mathbf{q}_0)]\{\tilde{\mathbf{q}}\}C'(k, \bar{m}_e, \bar{h}_e) = \{0\}$$

(3.19)

Introducing a new variable $\mathbf{y} = \begin{Bmatrix} \dot{\mathbf{q}} \\ \mathbf{q} \end{Bmatrix}$ and writing the deficiency function as $C'(k, \bar{m}_e, \bar{h}_e) = \frac{N(\bar{s})}{D(\bar{s})}$, Eq. (3.19) is rewritten as :

$$\dot{\mathbf{y}} = \mathbf{A}\,\mathbf{y} + \mathbf{B}\,\mathbf{y}\;C'(k, \bar{m}_e, \bar{h}_e) = \mathbf{A}\,\mathbf{y} + \mathbf{B}\,\mathbf{y}\frac{N(\bar{s})}{D(\bar{s})}$$

(3.20)

Using canonical reduction techniques [58], Eq. (3.20) can be written in a state space form as [59, 60] :

$$\dot{\mathbf{Z}} = \mathbf{H}\,\mathbf{Z}$$

(3.21)

The reduction steps of Eq. (3.20) to Eq. 3.21 are given in Appendix (A.2). The flutter boundary is determined when the real part of one of the eigenvalues of the matrix $\mathbf{H}$ crosses the imaginary axis. The method of normal modes is used to obtain the eigenvalues of the matrix $\mathbf{H}$. The number of the normal modes is chosen after calculating the time response for these modes.

3.2 Results and Discussion

3.2.1 Data

The blade properties are assumed to be uniform along the blade. The non-dimensional inflow velocity is set to be a constant equal to the value of the nonuniform flow at $0.75R$. A typical range

for the collective pitch is chosen including high thrust range($\theta_c > 15^o$). The center of gravity and the tension center of the cross section coincide with the elastic axis. Dividing the blade into six finite elements gives an acceptable accuracy for the square error resulting from solving the nonlinear steady equations of motion ,i.e. $\sum(Error)^2 < 10^{-5}$. Table 3.1 shows the square root of the normal modes after two different time intervals. Thus only five modes are used to transform the equations of motion to the modal space. The values of the parameters used are listed in Table 3.2.

Table 3.1: Normal modes magnitude at different time.

	$T_f = 5sec$	$T_f = 100sec$
3-Modes	3.1985	3.2077
4-Modes	3.1992	3.2084
5-Modes	3.1993	3.2085
6-Modes	3.1993	3.2085

Table 3.2: Rotor Blade Parameters.

ω_v	$= [0.5 \quad 2.5]$	θ_c	$= [0^o \ 25^o]$
ω_F	$= 1.15$	k_A^2/k_m^2	$= 1.5$
ω_ϕ	$= 2.5, 2.9, 3, 4, 5$	k_m/R	$= 0.025$
a_o	$= 2\pi$	$k_{m_1}^2/k_{m_2}^2$	$= 0$
C_{D_o}	$= 0.01$	c/R	$= \pi/40, 0.09722$
β_{pc}	$= [0^o \ 7^o]$	γ	$= 5, 6.308$

For the optimization problem, a rational polynomial of order eight is used, i.e. $i = 8$. This number is based on the Bode plot [58] of the approximation function as discussed in details in Ref. [51]. The approximation must have enough poles and zeros to capture the oscillatory part of the deficiency function at low reduced frequencies.

3.2.2 Results
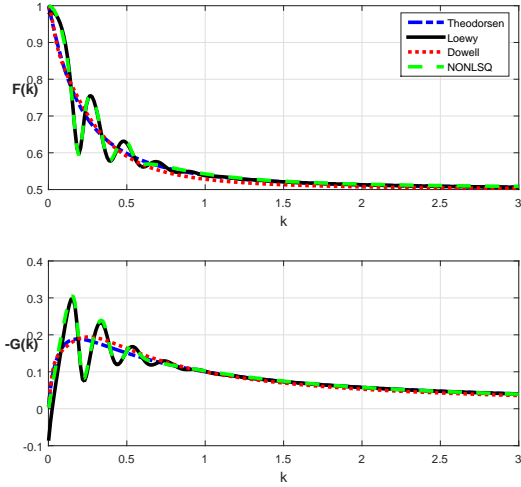
(a) Loewy's Function and it's Pade Approxiamtions for $\bar{r}_e = 5, \bar{h}_e = 5.43$
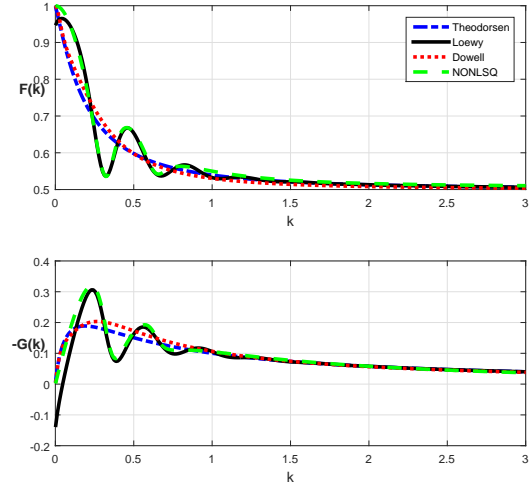
(b) $\bar{r}_e = 3, \bar{h}_e = 4$
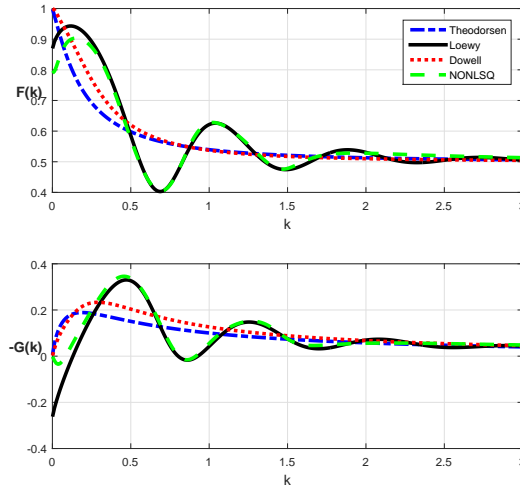
(c) $\bar{r}_e = 1.5, \bar{h}_e = 1.57$

Figure 3.2: Loewy's Function and it's Pade Approxiamtions

The results of the constrained optimization of Eq. (3.6) for three different cases of rotors are shown in Figure 3.2. The radial positions and the chord ratios used for evaluating the value of $C'(k, \bar{m}_e, \bar{h}_e)$ are $r = 0.75R, r = 0.8R, r = 0.3R$ and $c/R = 0.079, c/R = 0.1334, c/R = 0.01$

respectively. Because the optimization algorithm is so sensitive to the initial condition, the genetic algorithm is used to determine a good initial guess for the coefficients in order to start from a feasible point. Tables 3.3-3.5 list the poles and zeros for each rotor case. As seen from Figure 3.2, the rational polynomial is capable of capturing the oscillation at lower reduced frequency and the numerical values of poles and zeros indicates that the constraints are satisfied.
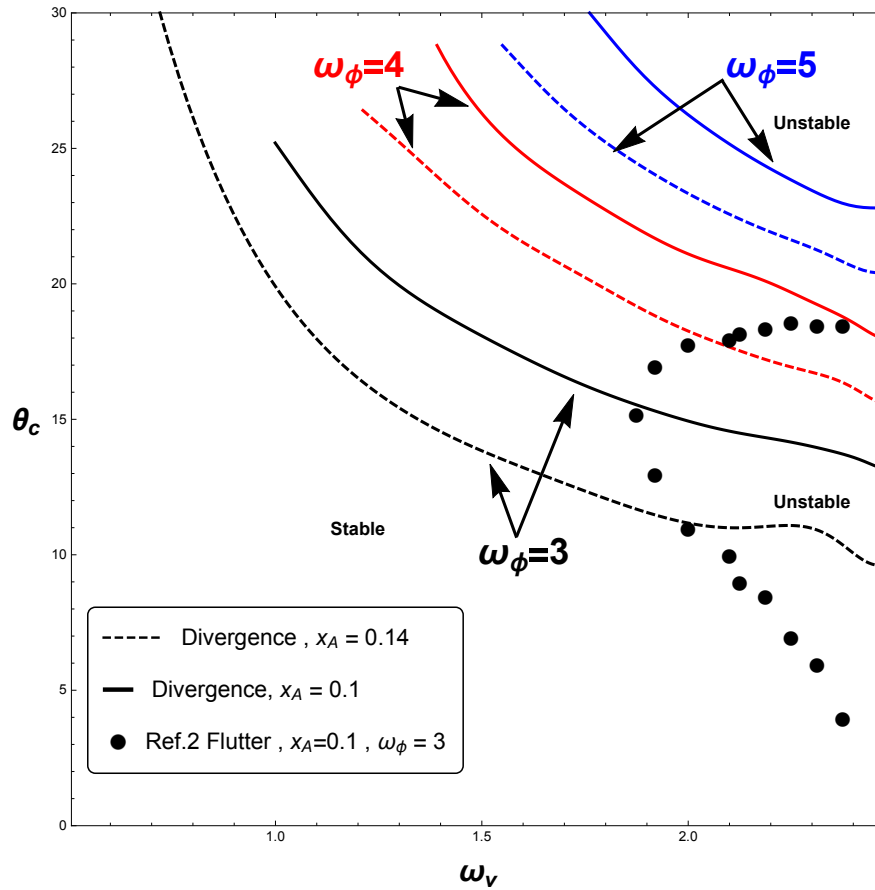
Figure 3.3: Divergence boundary represented as a collective pitch θ_c versus non-dimensional lead-lag frequency ω_v.

3.2.3 Discussions

Regarding the blade equilibrium, the trim deflections are obtained by solving the nonlinear steady equations of motion (3.18). Figure 3.3 represents the effect of varying the torsional stiffness and

the aerodynamic offset. The divergence phenomenon is observed to be more critical than flutter. The unstable region increases as the torsional stiffness decreases or the offset increases. The trends of the results for these divergence boundaries agree well with that of Ref. [54], although they used a slightly different blade parameters. The results in Ref. [16], shown in Fig. 3.3, indicated that for $\omega_\phi = 3$ and $x_A = 0.1$, which was based on a large defection theory, the domain of θ_c versus ω_v are statically stable and the flutter phenomenon is more critical. It means that the degree of nonlinearity of the structure model needs to be investigated.

Figure 3.4 depicts the flutter boundary for zero aerodynamic offset and for different approximations of the deficiency function. The quasi steady results are in good agreement with those of Ref.[53]. The slight difference between the present results and those of Ref. [16] is that because the structure model therein was based on large deflection theory. For collective pitch $\theta_c > 10^o$, the upper unstable region expands as the type of the approximation of the deficiency changes. In other words, the unsteady aerodynamics has a destabilizing effect at higher angles of attack.The three approximations yields the same upper branch as their real and imaginary values mostly coincide on the range $k > 0.5$ as seen in Fig. 3.2. Ref. [61] showed the same trend for the upper bound but for the case of $\beta_{pc} = 0, \;\; x_A = 0.2, \;\; \omega_\phi = 6.17$ and for a linearized static equilibrium conditions.

On the other hand at low collective pitch $\theta_c < 10^o$, the unstable bubble region arised from the dihedral effect β_{pc}, shrinks from both sides. The bubble region shrinks from the right side from $\omega_v = 1.75$ to $\omega = 1.48$ when any one of the approximations are used and shrinks from left side $\omega_v = 0.8$ to $\omega = 1.25$ only when NONLSQ approximation is used. The surprising result is that the unsteady aerodynamics has a stabilizing effect at low collective pitch.

At low collective pitch the behavior is quite different from that at a higher one. The shrinkage from the right side can be interpreted from Fig 3.2 as the unsteady aerodynamics predicts half the value of the unsteady loads compared to quasi steady case for $k > 0.5$. For the left part, the shrinkage may be interpreted as Jones' and Dowell's approximations can't capture the oscillatory nature of Loewy's function at low reduced frequency of $k < 0.5$. This means that the oscillatory behavior of Loewy's function at low reduced frequency has more stabilizing effect as the lead-lag

frequency approaches the soft stiffness limit. Similar trends, but reversed to that shown in the present analysis, for these two different effects of the unsteady aerodynamics as a function of the lead-lag frequency can be found in Ref. [62] for a simple coupled flap, lag rotor.
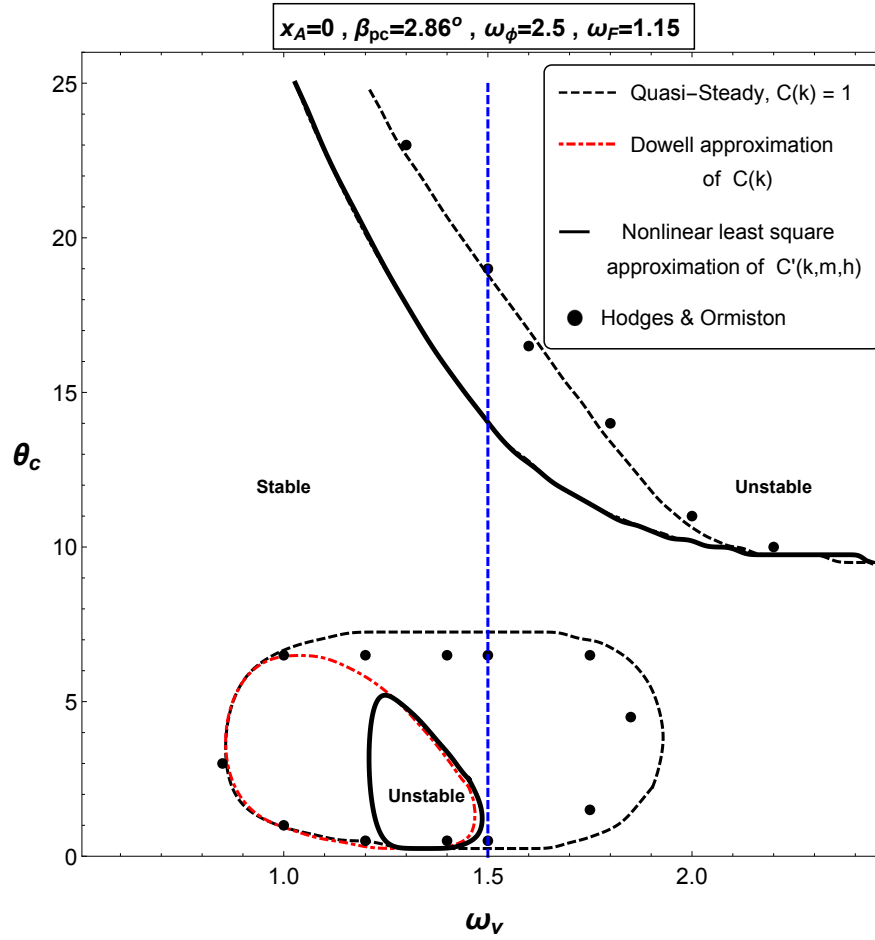
Figure 3.4: Flutter Boundary

(a) Modes for $\gamma = 5, c/R = \pi/40$

(b) Modes for $\gamma = 6.308, c/R = 0.09722$
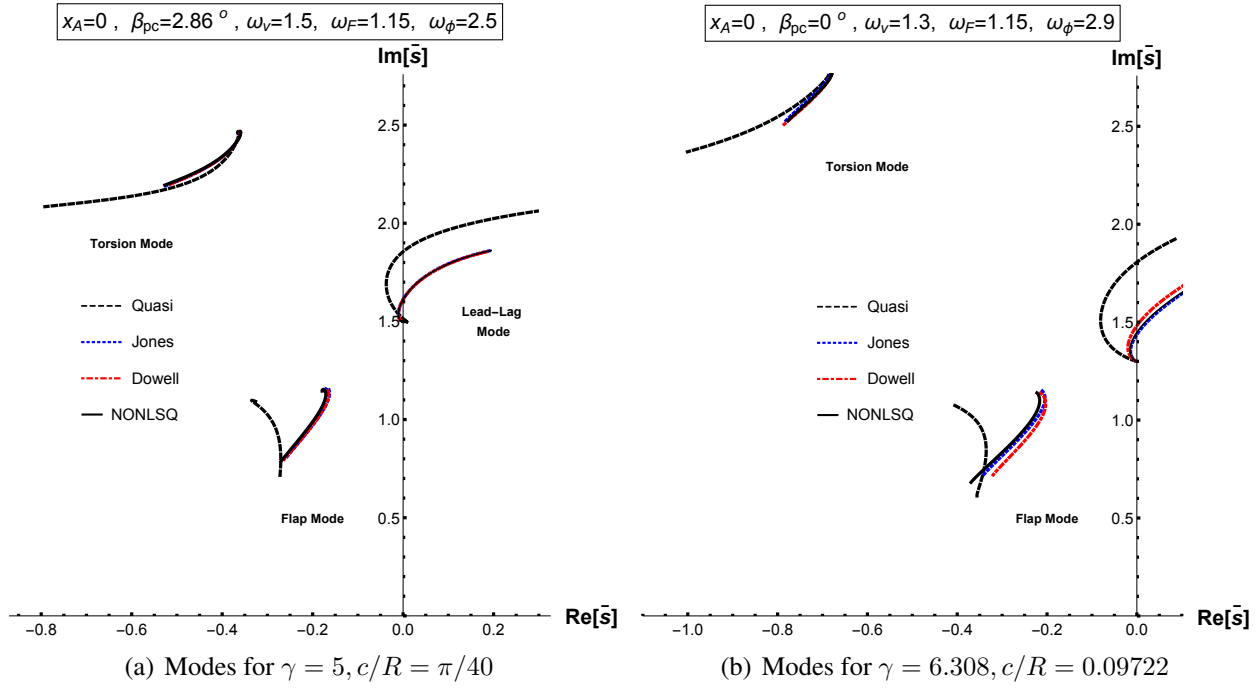
Figure 3.5: Flap, lead-Lag and torsion modes for two blade configurations
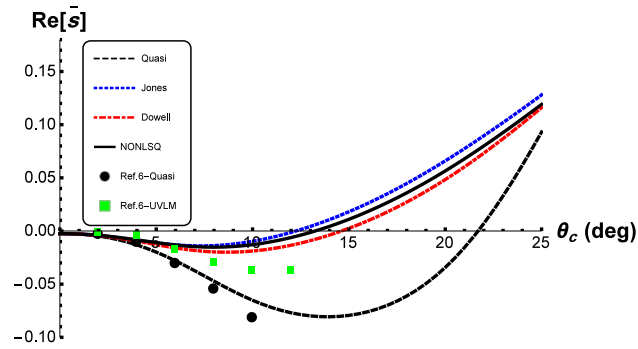
Figure 3.6: Lead-lag damping for four blade rotor, $\gamma = 6.308, c/R = 0.09722, \beta_{pc} = 0$
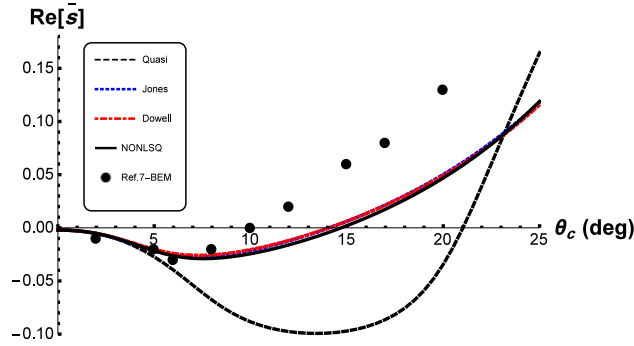
Figure 3.7: Lead-lag damping for two blade rotor,$\gamma = 5, c/R = \pi/40, \beta_{pc} = 0$

The root-locus of flap, lead-lag and torsion modes are depicted in Fig. 3.5 for the parameters shown on the top of the figure. The collective pitch θ_c is varied from 0° to 25°. The flapping mode develops a considerable change in the damping ratio but tends to approach the values obtained by the quasi steady approximation as collective pitch increases. This can be interpreted as the real part of the deficiency function F decreased to far values from the unity, the quasi steady limit, while having an oscillatory behavior at $k < 0.5$. This result agrees well that predicted by Loewy[12] for the two dimensional case, i.e.$\partial C_L/\partial(\dot{h}/U) = 2\pi F'$. Moreover, the torsion mode for the three unsteady approximations travels half the distance of the quasi-steady case. This means that the unsteady circulatory components of the pitching moment in Eq. (3.1) develop an additional positive torsional damping. This effect cannot be directly predicted as the moment arm is zero, i.e. $x_A = 0$. Furthermore, at higher collective pitch, the lead-lag mode for the three approximations enters the right half plane at earlier value of collective pitch compared to the quasi-steady case. It's also observed that the instability happens at low collective pitch vanishes when any type of the approximation is used for the case of $\beta_{pc} = 2.86^o$ as can be seen form Fig. 3.4 for the case of $\omega_\phi = 2.5$. Also the damping part calculated using $C'(k)$ decreased to a lower value in comparison to the quasi steady result, i.e. $\partial C_L/\partial(\dot{h}/U) = 2\pi F'$.

Figures 3.6 and 3.7 shows the damping part of the lead-lag mode versus collective pitch compared to the results obtained by Ref.[63] and Ref. [64] respectively. The present results calculated using any approximation matches well with those of Ref. [63, 64] for collective pitch below 6°. The data from Ref. [63] and Ref. [64] were available from 0° collective pitch up to 12° and 20° respectively.

From Fig.3.6, the difference between the quasi steady results is mainly because the structure model used in Ref. [63] was based on large deflection theory. The quasi-steady, Johns', Dowell's and NONLSQ approximations give an instability boundary at collective pitchs θ_I of 22°, 15°, 13° and 12° respectively. These instability values obtained using the three approximation rather than the quasi-steady one are more conservative than that observed by an extrapolation of the result of Ref. [63], which was obtained using the unsteady vortex lattice method (UVLM),i.e. $\theta_I = 17^o$.

For the two bladed rotor case shown in Fig. 3.7, the quasi-steady, Johns', Dowell's and NONLSQ approximations respectively gives 21°, 14°, 14° and 15° for the instability pitch value θ_I. The results of Ref. [64] were obtained using boundary element method (BEM) for predicting the unsteady loads. Their results showed to be more conservative than obtained by 2-D theory, i.e. $\theta_I = 10^o$, which reveals the power of the numerical technique used to model the unsteady aerodynamic loads.
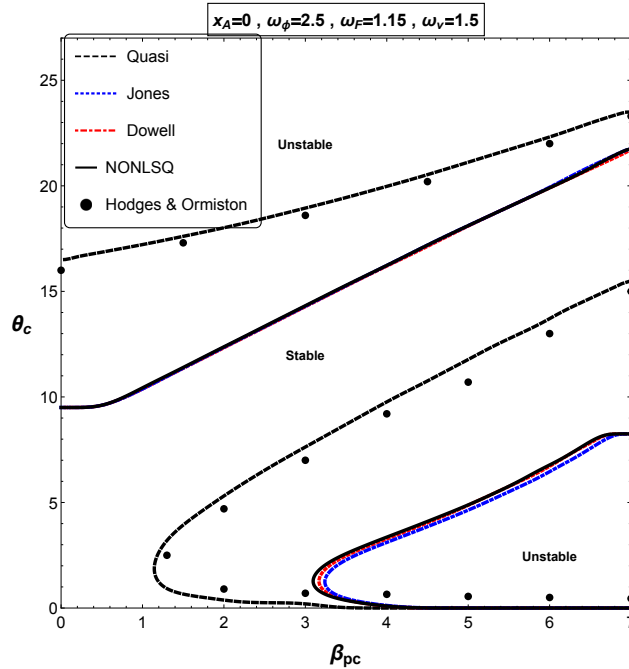
Figure 3.8: Beta Effect

Figure 3.8 shows the effect of varying the collective pitch θ_c versus the precone angle β_{pc} compared to Ref. [65]. The same behavior to that in Fig. 3.4 is obtained except that the three approximations for the deficiency function yields the same bubble region. This is because the effect of unsteady

aerodynamic approximation at low collective pitch is coupled with the lead-lag frequency ω_v. The stability boundary seems to be sensitive to the type of unsteady aerodynamics even if $x_A = 0$. This result contradicts with that of Ref.[16] as their boundaries, which were obtained using $p-k$ method, appeared to be insensitive to unsteady aerodynamics. The results from Fig .3.5-3.8 reveal the fact that using time-domain approximations of the deficiency function for predicting the dynamic instability boundaries is more reliable than p-k method.

Table 3.3: Poles and Zeros for $\bar{r}_e = 3, \bar{h}_e = 4$

Zeros $N(ik)$	Poles $D(ik)$
-0.0623 $\pm i$ 0.3324	-0.0934 $\pm i$ 0.3382
-0.0825 $\pm i$ 0.395	-0.4738 $\pm i$ 0.0266
-0.6394 $\pm i$ 0.2578	-0.0941 $\pm i$ 0.6349
-0.9725 $\pm i$ 25.515	-0.0515 $\pm i$ 25.395

Table 3.4: Poles and Zeros for $\bar{r}_e = 1.5, \bar{h}_e = 1.57$

Zeros $N(ik)$	Poles $D(ik)$
-0.1442 $\pm i$ 0.7251	-0.3848 $\pm i$ 0.4133
-0.6975 $\pm i$ i 0.5834	-0.2567 $\pm i$ 0.8313
-0.1746 $\pm i$ 1.4578	-0.2138 $\pm i$ 1.4558
-0.05247	-0.062
0	0

Table 3.5: Poles and Zeros for $\bar{r}_e = 5, \bar{h}_e = 5.43$

Zeros $N(ik)$	Poles $D(ik)$
-0.0309 $\pm i$ 0.1977	-0.0455 $\pm i$ 0.1986
-0.0555 $\pm i$ 0.3816	-0.082 $\pm i$ 0.3756
-0.0527 $\pm i$ 0.5403	-0.0527 $\pm i$ 0.5355
-0.5924	-0.2988
-4362	-4330.2

3.3 Conclusions

In this chapter, different Padé approximations for Loewy's deficiency function were used to investigate the dynamic stability of a hovering rotor blade. After linearizing the equations of motion about the nonlinear trim deflections, the flutter boundary was found in time domain by approximating the lift deficiency function as a rational polynomial in terms of Laplace operator. Next, the static stability results are summarized as :

1) For offsets $x_A > 0$, the divergence boundaries, obtained by solving the nonlinear trim equations are more critical than flutter. This result agrees with most of the previous work but highly differs from that obtained using large deflection theory. In other words, when the structure model is based on a moderate deflection theory the divergence boundary, obtained by solving the nonlinear trim equations, is found to be more critical than flutter. On the other hand, when the structure model is based on the a large deflection theory no divergence boundary exist and the flutter phenomenon due to torsional instability is more critical.

The results shown for the flutter boundaries are in good agreement following the same behavior obtained by numerical simulations. The time-domain unsteady aerodynamic model has different effects on the stability boundaries summarized as follow :

2) For the case of zero offset $x_A = 0$ and $\beta_{pc} = 2.86^o$, the unsteady aerodynamic has a two counter effects associated with varying both collective pitch and lead-lag frequency.

3) For lead-lag frequency $\omega_v \in [1.2 \ 2]$, the three aerodynamic approximations have the same effect of destabilizing and stabilizing the lead-lag mode at high and low collective pitchs respectively.

4) For $\omega_v < 1.2$, the NONLSQ approximation of Loewy's function has a stabilizing effect on the bubble region at low lead-lag frequency. This effect is not observed when using any approximation other than NONLSQ, because they didn't capture the oscillatory behavior as NONLSQ did.

5) For the case of zero offset $x_A = 0$, $\omega_v = 1.5$ and varying precone $\beta_{pc} \in [0 \ 7]$, the three approximations gives the same effect on stability boundary as result 3.

6) More flapping vibrations are induced as the damping part of the flapping mode decreased sig-

nificantly, i.e. $\partial C_L / \partial(\dot{h}/U) = 2\pi F'$.

7) The unsteady circulatory terms in the pitching moment equation augment a postive damping which decreases the overall torsional damping.

8) The damping part of the lead-lag mode decreased as the type of the aerodynamic approximation is used, leading to a lower values of instability limits. These values are in good agreement compared to that obtained by BEM and UVLM numerical solutions.

Chapter 4

Optimal Tail Kinematics for Fish-Like Locomotion using the Unsteady Vortex Lattice Method

4.1   Introduction

Motivated by the desire to understand and characterize fish, engineers have long considered modes of such motions to inspire the design and improvement technologies for human need. Earlier considerations of the nature of fish propulsion have been brought into attention by Lindsey [66], that was followed by more detailed work by Bozkurttas et al. [67]. The interest in understanding the generation of propulsive forces was mainly inspired by impressive structural and kinematic capabilities. Further detailed work since Borelli has been diversified, with descriptions shared by Sir James Gray (1933ac), Lighthill [68], Webb Blake [69], Maddock et al. [70], and Triantafyllou et al. [71] among others. Published literature included experimentally and analytically detailed analyses of patterns of body, morphological adaptations and their effects on flow patterns that have helped scientists understand how propulsion is produced.

In swimming, fish vary their shape to generate fluid dynamic forces needed for propulsion and control. The oscillating tails and fins are able to generate additional thrust, and may also be used to balance roll and yaw moments generated during locomotion. Our ultimate goal is to develop an understating of the underlying physics of fish locomotion based on a three-dimensional potential flow model that can be used to support a geometrically controlled framework for the design and control of pisciform swimmers. This would be achieved using periodically forced mechanical systems, and compromised of a series of rigid hydrofoils and flaps. The ultimate question to be answered is: For what parameter values (Reynolds number, frequency of oscillation, number of links, and model parameters) will the proposed unsteady flow model capture forces and moments with sufficient accuracy to support geometric control design and analysis?

Towards that objective, we investigate the optimal kinematics of fish-tail motion. We considered the oscillatory type of fish under the action of hydrodynamic loads based on two-dimensional theory. Later, we used the three-dimensional theory to verify the two-dimensional results. The base body is considered as a rigid part and the tail is allowed to flap either flexibly or rigidly. The flexible motion of the tail is modeled in a two different ways. The first one the flexible motion of the tail assumed to be a combination of a simple harmonic motions in time using the first two mode shapes of Euler-Bernoulli beam. The second one the flexible motion of the tail is determined by solving the fluid-structure coupled problem between the tail motion and the hydrodynamic loads acting upon it. The hydrodynamic loads are calculated using the two-dimensional and three-dimensional unsteady vortex lattice model (UVLM). The propulsive efficiency versus the Strouhal Number is depicted for the three cases.

4.2 Geometrical Model of the Tail

The two-dimensional fish is modeled as a two bodies connected at one point as shown in Fig. 4.1. The base body and tail are modeled as a rigid ellipse and a flexible beam respectively. The body and the tail are moving with the same uniform velocity U_∞. The input to the tail is angular

displacement $\theta(t)$, and is to be determined by minimizing the hydrodynamic power subjected to zero net thrust on the fish body. For the rigid beam case the deflection w is neglected, i.e. $w = 0$, while for the first flexible case, active flexibility, it is taken to be a simple harmonic combination of the first and second modes of the beam [3] as
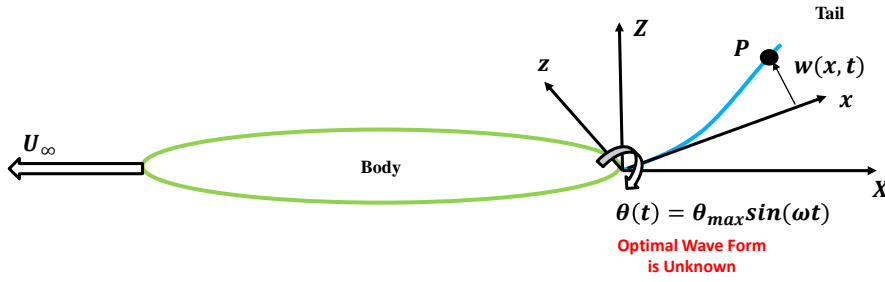
Figure 4.1: Simple model of the fish-tail of oscillatory type.

$$w(x,t) = A_1 sin(\omega t)\Psi_1(x) + A_2 sin(\omega t + \Phi)\Psi_2(x) \tag{4.1}$$

where A_1 and A_2 are the amplitude of the first and second mode respectively, and ω is the frequency of oscillation, i.e. $\omega = 2\pi f$. For the case of passive flexible beam, the tail deflection is determined as follows. The position of a general point P on the tail and the angular velocity of the tail can be defined as

$$\vec{r}_p = x\hat{i} + w\hat{k} \tag{4.2}$$

$$\vec{\omega} = \dot{\theta}\hat{\mathbf{j}} \tag{4.3}$$

The inertial velocity and accelration can be computed as follows :

$$\begin{aligned}
\vec{\mathbf{V}} &= \frac{d\vec{\mathbf{r}_p}}{dt} = \frac{\partial\vec{\mathbf{r}_p}}{\partial t} + \vec{\omega} \times \vec{\mathbf{r}_p} \\
&= \dot{\theta}w\hat{\boldsymbol{i}} + \left(\dot{w} - \dot{\theta}x\right)\hat{\boldsymbol{k}}
\end{aligned} \tag{4.4}$$

$$\begin{aligned}
\vec{\mathbf{a}} &= \frac{d\vec{\mathbf{V}}}{dt} = \frac{\partial\vec{\mathbf{V}}}{\partial t} + \vec{\omega} \times \vec{\mathbf{V}} \\
&= \left(\ddot{\theta}w + 2\dot{\theta}\dot{w} - \dot{\theta}^2 x\right)\hat{\boldsymbol{i}} + \left(\ddot{w} - \ddot{\theta}x - \dot{\theta}^2 w\right)\hat{\boldsymbol{k}}
\end{aligned} \tag{4.5}$$

Applying the equilibrium conditions on a general element centered at the point $\boldsymbol{P}$ in x and z directions, we get

$$T(x) = \frac{m\dot{\theta}^2}{2}(R^2 - x^2) + m\int_x^R \left(\ddot{\theta}w + 2\dot{\theta}\dot{w}\right)dx \tag{4.6}$$

$$\frac{\partial^2}{\partial x^2}\left(EI\frac{\partial^2 w}{\partial x^2}\right) - \frac{\partial}{\partial x}\left(T(x)\frac{\partial w}{\partial x}\right) + m\left(\ddot{w} - \ddot{\theta}x - \dot{\theta}^2 w\right) = F_H(w, \dot{w}) \tag{4.7}$$

The instantaneous tail dispacement $w(x,t)$ is determined by the solving the coupled equations of motion defined in Eq. (4.6) and Eq. (4.7) according to the flowchart shown in Fig. 4.6. $T(x)$ is the tension in the tail due to the angular rotation $\theta(t)$. E and I are the modulus of elasticity and moment of inertia of the tail respectively. $F_H(w, \dot{w})$ is the external hydrodynamic loads generated on the tail by the motion θ. The structural and hydrodynamic loads are coupled through the presence of the variable $w(x,t)$ in both sides. The hydrodynamic forces and moments generated by the tail motion are calculated using the unsteady vortex lattice method (UVLM) [18, 19, 72–76]. The calculation of these loads are defined in the next section.

4.3   Hydrodynamic Model

In the first two sub-sections the two and three-dimensional unsteady vortex lattice method are introduced. In the last subsection, the load and power calculations are discussed for a general three-dimensional case. The two-dimensional version of the loads are then just a special case of those expressions.

4.3.1   Two-Dimensional Unsteady Vortex Lattice Model

The tail section can move and rotate with a velocity $\boldsymbol{V}$ and angular velocity $\dot{\theta}$ respectively. As shown in Fig. 4.2, the tail is replaced by a vortex sheet of N bound vortices Γ_{b_i}. At each time step, a vortex is released from the trailing edge Γ_{w_k}. The Kutta condition is satisfied by placing the vortex at the quarter chord of each panel and applying the no-penetration boundary condition at the three quarter point of each panel [18, 19]. the strength of the shed vortex is determined by applying Kelvin circulation theorem at each time step, i.e. $d(\sum_{i=1}^{N} \Gamma_{b_i} + \sum_{k=1}^{N_w} \Gamma_{w_k})/dt = 0$. The no-penetration boundary condition is defined as

$$(\boldsymbol{V}_B + \boldsymbol{V}_W - \boldsymbol{V}_A).\boldsymbol{n}_i = 0 \tag{4.8}$$

where $\boldsymbol{n}_i$ is the normal vector to the body of panel i. $\boldsymbol{V}_B$, $\boldsymbol{V}_W$, and are the velocities induced by the bound vortices, wake vortices at panel i. $\boldsymbol{V}_A$ is absolute motion of the body at apnel i. From Figure 4.2, the absolute velocity of any point on the body is given by

$$\boldsymbol{V}_A = \boldsymbol{V} + \frac{\partial \boldsymbol{r}_i}{\partial t} + \dot{\theta}\boldsymbol{j}_b \times \boldsymbol{r}_i \tag{4.9}$$

The velocities induced by the body and wake vortices are calculated using the Biot-Savart law. In general, the induced velocity at point $\boldsymbol{r}_o$ by a vortex of strength Γ at a point $\boldsymbol{r}$ is given as

$$\begin{Bmatrix} u \\ w \end{Bmatrix} = \frac{\Gamma}{2\pi|(\boldsymbol{r} - \boldsymbol{r}_o)|^2} \begin{Bmatrix} z - z_o \\ -(x - x_o) \end{Bmatrix} \tag{4.10}$$

Using Eq. (4.10), the no-penetration boundary condition in Eq. (4.8) is re-written as

$$\begin{bmatrix} A \end{bmatrix} \begin{Bmatrix} \boldsymbol{\Gamma}_b \\ \Gamma_{w_k} \end{Bmatrix} = \begin{Bmatrix} \boldsymbol{V}_A.\boldsymbol{n} \end{Bmatrix} \tag{4.11}$$

where $A_{i,j} = (u, w)_{i,j}.\boldsymbol{n}_i$, is the normal component of the velocity induced by a vortex j of unit circulation at the control point of panel i. A is called the influence coefficient matrix. Equation (4.11) is an n equations in $n + 1$ unknowns. The $n + 1$ additional equation is given by the Kelvin condition defined as

$$\sum_{i=1}^{n} \Gamma_{b_i}^k + \Gamma_{w_k} = \sum_{i=1}^{n} \Gamma_{b_i}^{k-1} \tag{4.12}$$

Now Equations (4.11) and (4.12) are now a closed set of equations that are solved at each time step, $t = k\Delta t$, to determine the strength of the bound vortices $\Gamma_{b_i}^k$ and the shedding vortex Γ_{w_k}.
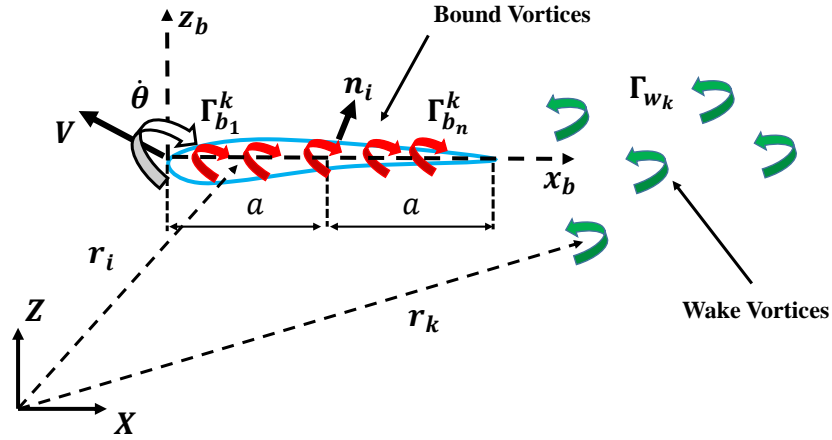
Figure 4.2: Discrete vortex model of fish tail using 2D UVLM.

Since the wake is force free, the wake vortices are allowed to move with the local fluid velocity. This is done prior to moving to the next time step. The change in the position of each wake vortex is calculated as

$$(\Delta X_k, \Delta Z_k) = (U_k, W_k)\Delta t \tag{4.13}$$

where (U_k, W_k) are the local velocity at each wake vortex induced by the presence of the body and other wake vortices. Then the new position of the wake vortex is given by a first order Euler time scheme as

$$\boldsymbol{r}_k(t + \Delta t) = \boldsymbol{r}_k(t) + (\Delta X_k, \Delta Z_k) \tag{4.14}$$

4.3.2   Three-Dimensional Unsteady Vortex Lattice Model

In three dimensional, the tail is represented by an $N_x \times N_y$ bound vortex rings. At each time step, the trailing vortex rings leave the tail. The boundary condition defined in Eq. (4.8) still holds as

$$(\boldsymbol{V}_B + \boldsymbol{V}_W - \boldsymbol{V}_A).\boldsymbol{n}_{ij} = 0 \tag{4.15}$$

where $\boldsymbol{n}_{ij}$ is the normal vector to the body of panel i, j and is calculated from Figure 4.4 as

$$\boldsymbol{n}_{ij} = \frac{\boldsymbol{r}_{12} \times \boldsymbol{r}_{14}}{|\boldsymbol{r}_{12} \times \boldsymbol{r}_{14}|} \tag{4.16}$$

$\boldsymbol{V}_B, \boldsymbol{V}_W$ are the velocities induced by the bound and wake vortex rings at panel i, j. $\boldsymbol{V}_A$ is absolute motion of the body at panel i, j. From Figure 4.5, the absolute velocity of any point on the body is given by
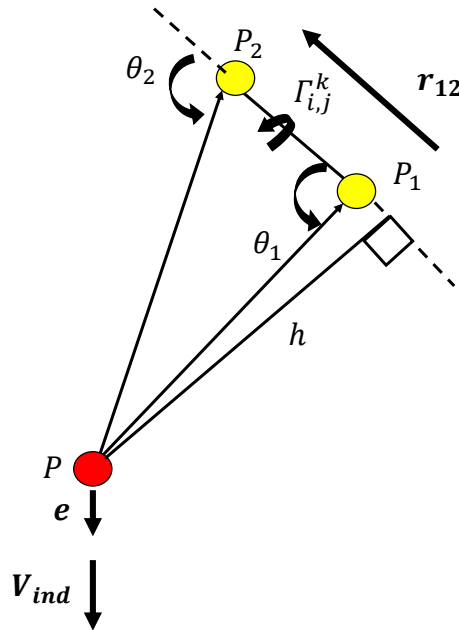
Figure 4.3: General Vortex Line in the three dimension.

$$\boldsymbol{V}_{A_{i,j}} = \boldsymbol{V}_{i,j} + \frac{\partial \boldsymbol{r}_{ij}}{\partial t} + (\dot{\phi}\boldsymbol{i}_b, \dot{\theta}\boldsymbol{j}_b, \dot{\psi}\boldsymbol{k}_b) \times \boldsymbol{r}_{ij} \tag{4.17}$$

The transformation of rigid body velocity of panel i, j, $\boldsymbol{V}_{i,j}$, between body and inertial frame is defined as

$$\begin{Bmatrix} U_b \\ V_b \\ W_b \end{Bmatrix} = \begin{bmatrix} cos\psi & sin\psi & 0 \\ -sin\psi & cos\psi & 0 \\ 0 & 0 & 1 \end{bmatrix} \begin{bmatrix} cos\theta & 0 & -sin\theta \\ 0 & 0 & 1 \\ sin\theta & 0 & cos\theta \end{bmatrix} \begin{bmatrix} 1 & 0 & 0 \\ 0 & cos\phi & sin\phi \\ 0 & -sin\phi & cos\phi \end{bmatrix} \begin{Bmatrix} U \\ V \\ W \end{Bmatrix} \tag{4.18}$$

where ϕ, θ, and ψ are the rotations about $\boldsymbol{i}_b$, $\boldsymbol{j}_b$, and $\boldsymbol{k}_b$ respectively. To calculate $\boldsymbol{V}_B$ and $\boldsymbol{V}_W$, the velocity induced by a general vortex line as defined in Figure 4.3 is given by

$$\boldsymbol{V}_{ind} = \frac{\Gamma_{i,j}^k}{2\pi h} (cos\theta_1 - cos\theta_2) \boldsymbol{e} \tag{4.19}$$

Then the velocity induced by a vortex ring, $\boldsymbol{V}_B$ or $\boldsymbol{V}_W$, will be the summation of four connected vortex lines as shown in Figure 4.4.
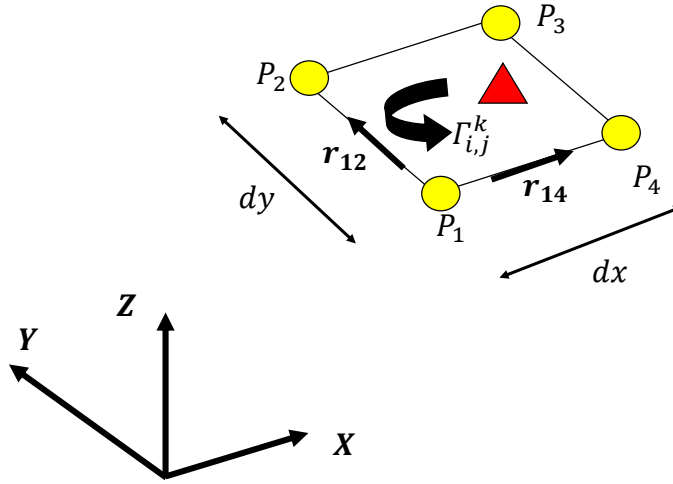
Figure 4.4: General Vortex Ring in the three dimension.

The Kutta condition in three dimension is satisfied by shedding the trailing edge vortices with the last time step value of the trailing bound vortices as shown in Figure 4.5. In addition, there is no need to introduce an additional equation to satisfy the Kelvin condition. This is due to the nature that vortex rings form a closed loop and each parallel lines that form this ring are of opposite and equal vorticity magnitude as seen in Figure 4.4. Using Eq. (4.19), the no-penetration boundary condition in Eq. (4.15) is re-written as

$$\left[A \right] \left\{ \Gamma_b \right\} = \left\{ V_A . n \right\} \tag{4.20}$$

where $A_{i,j} = (u, v, w)_{i,j} . n_{k,l}$ is the velocity induced by the vortex ring k, l of unit circulation at the control point of the vortex ring i, j. Equation (4.20) is an $N_x \times N_y$ equations in $N_x \times N_y$ which are the bound vortices, i.e. $\Gamma_{i,j}$. The vortex rings are allowed to move with the local fluid velocity since they are force free. The change in the position of the corner points of each wake vortex ring

is calculated as

$$(\Delta X_k, \Delta Y_k, \Delta Z_k) = (U_k, V_k, W_k)\Delta t \tag{4.21}$$

Then the new position of the vortex ring is given by a first-order Euler time scheme as

$$\boldsymbol{r}_{Nx,j}(t + \Delta t) = \boldsymbol{r}_{Nx,j}(t) + (\Delta X_k, \Delta Y_k, \Delta Z_k) \tag{4.22}$$
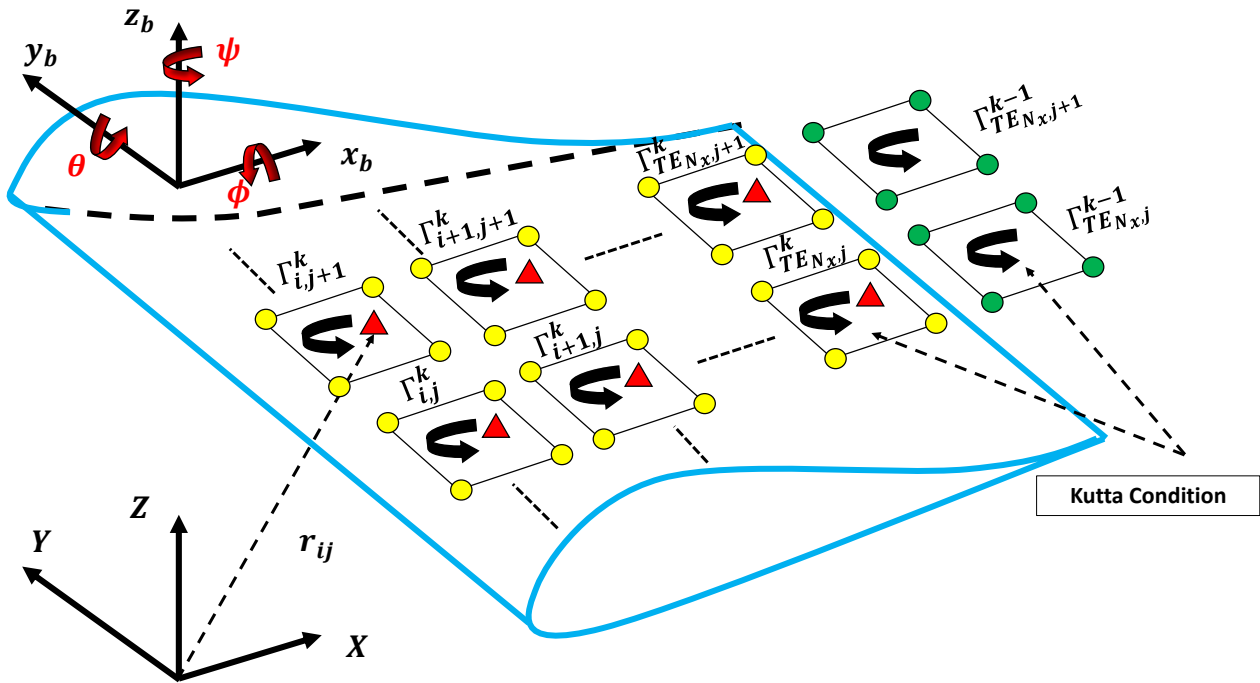
Figure 4.5: Discrete vortex model of fish tail using 3D UVLM

4.3.3 Loads and Power Calculation

The local lift and drag components at each panel are given by [19],

$$L_{i,j} = \rho dy \left(||\boldsymbol{V}_{A_{i,j}}||(\Gamma_{i,j} - \Gamma_{i-1,j}) + dx \frac{\partial}{\partial t}(\frac{\Gamma_{i,j} + \Gamma_{i-1,j}}{2}) \right) cos\alpha_{i,j} \tag{4.23}$$

$$D_{i,j} = \rho dy \left(-(W_{ind} + W_{wake})(\Gamma_{i,j} - \Gamma_{i-1,j}) + dx \frac{\partial}{\partial t} (\frac{\Gamma_{i,j} + \Gamma_{i-1,j}}{2}) sin\alpha_{i,j} \right) \qquad (4.24)$$

where $||\boldsymbol{V}_{A_{i,j}}||$ is the magnitude of the absolute velocity of the panel i, j, $\alpha_{i,j}$ is the angle of attack of the panel i, j relative to the free-stream direction, and W_{ind}, and W_{wake} are the induced velocity by the stream-wise vortex lines and wake vortices respectively. The angle of attack is calculated as

$$\alpha_{i,j} = tan^{-1} \left(\frac{\boldsymbol{V}_{A_{i,j}}.\boldsymbol{n}_{i,j}}{\boldsymbol{V}_{A_{i,j}}.\boldsymbol{\tau}_{i,j}} \right) \qquad (4.25)$$

These local lift and drag forces are acting along the local lift and drag unit vectors who are given by

$$\boldsymbol{e}_{lift_{i,j}} = \boldsymbol{T}_{i,j}.\boldsymbol{T}_{\alpha_{i,j}}^{T}.\boldsymbol{T}_{i,j}.\boldsymbol{n}_{i,j}$$
$$\boldsymbol{e}_{drag_{i,j}} = \boldsymbol{T}_{i,j}.\boldsymbol{T}_{\alpha_{i,j}}^{T}.\boldsymbol{T}_{i,j}.\boldsymbol{\tau}_{i,j} \qquad (4.26)$$

where the matrices $\boldsymbol{T}_{\alpha_{i,j}}$ and $\boldsymbol{T}_{i,j}$ are given by

$$\boldsymbol{T}_{\alpha_{i,j}} = \begin{bmatrix} cos\alpha_{i,j} & sin\alpha_{i,j} & 0 \\ -sin\alpha_{i,j} & cos\alpha_{i,j} & 0 \\ 0 & 0 & 1 \end{bmatrix} \qquad (4.27)$$

$$\boldsymbol{T}_{i,j} = \begin{bmatrix} \boldsymbol{\tau}_{i,j} & \boldsymbol{n}_{i,j} & \boldsymbol{q}_{i,j} \end{bmatrix} \qquad (4.28)$$

where $\boldsymbol{q}_{i,j}$ is calculated as

$$\boldsymbol{q}_{i,j} = \boldsymbol{\tau}_{i,j} \times \boldsymbol{n}_{i,j} \qquad (4.29)$$

The total force vector is then given as

$$\boldsymbol{F} = \sum_{i,j}^{N_x,N_y} \boldsymbol{F}_{i,j} = \sum_{i,j}^{N_x,N_y} \left(L_{i,j} \boldsymbol{e}_{lift_{i,j}} + D_{i,j} \boldsymbol{e}_{drag_{i,j}} \right) \qquad (4.30)$$

where the components in the $\boldsymbol{X}$ and $\boldsymbol{Z}$ are the total drag and lift force respectively. The input aerodynamic power in then calculated as

$$P_{in} = \sum_{i,j}^{N_x,N_y} \left((\boldsymbol{F}_{i,j}.\boldsymbol{n}_{i,j})(\boldsymbol{V}_{A_{i,j}}.\boldsymbol{n}_{i,j}) \right) \tag{4.31}$$

and the output power used to move the fish in forward motion is defined as

$$P_{out} = (\boldsymbol{F}.\boldsymbol{i}_x) \, U_\infty \tag{4.32}$$

The propulsive efficiency is then given as

$$\eta = \frac{\bar{P}_{out}}{\bar{P}_{in}} \tag{4.33}$$

where $\bar{()}$ is refers to the average over the number of tail flapping cycles. In the next section, we are discussing the finite-element approach that is used to solve the coupled problem between the tail structure and hydrodynamic loads generated by the tail motion.

4.4   Finite Element Model of the Coupled Problem

The finite element approach is applied to Eq. (4.7). The nonlinear term in the tension $T(x)$ is neglected [53], i.e. $T(x) \approx m\dot{\theta}^2(R^2 - x^2)/2$. The resulting equations are nonlinear time-varying of the form:

$$[\mathbf{M}]\{\ddot{\mathbf{q}}\} + [\mathbf{K}]\{\mathbf{q}\} = \{\mathbf{F}(\mathbf{q}, \dot{\mathbf{q}})\} \tag{4.34}$$

where $[\mathbf{M}]$ is the mass matrix $[\mathbf{K}]$ is the stiffness matrix, and $\{\mathbf{F}(\mathbf{q}, \dot{\mathbf{q}})\}$ is the time-dependent forcing vector containing terms that are dependent of the nodal degrees of freedom $\mathbf{q}$ resulting from the UVLM and the inertia loads. Hermite polynomials are used to represent the distribution of $\mathbf{q}$ over one element [16] with two degrees of freedom at each node, i.e. $\mathbf{q} = \{w \;\; \partial w/\partial x\}^T$. The

Mass and Stiffness matrices are calculated as follows:

$$[\boldsymbol{M}] = \int_0^1 (N_w)^T N_w d\xi$$

$$[\boldsymbol{K}] = \int_0^1 \left((N_w'')^T N_w'' + \frac{m\dot{\theta}^2}{2}(N_w')^T T(\xi + X_i)N_w' - \frac{m\dot{\theta}^2}{2}(N_w)^T N_w \right) d\xi \qquad (4.35)$$

$$\{\boldsymbol{F}(\boldsymbol{q}, \dot{\boldsymbol{q}})\} = \int_0^1 \left(N_w^T F_H(q, \dot{q}) + N_w^T \ddot{\theta}\, \xi \right) d\xi$$

where L is the element size, $\xi = x/L$ is the non-dimensional local position, m is the tail mass per unit length, $(\ )' = \partial/\partial\xi$ is the derivative with respect to ξ, and N_w is the Hermite polynomial shape function defined as

$$N_w = \{1 - 3\xi^2 + 2^3,\ L\xi(1 - xi)^2,\ \xi^2(3 - 2\xi),\ -L\xi^2(1 - \xi)\}^T \qquad (4.36)$$

The coupling between the structure and the hydrodynamic loads appears in $\boldsymbol{F}(\boldsymbol{q}, \dot{\boldsymbol{q}})$ which is determined using the UVLM. The equations of motion (4.34) are integrated using Newmark method [7]. The system of equations need to be solved for $\boldsymbol{q}$, and $\ddot{\boldsymbol{q}}$ at time $m + 1$ are defined as

$$[\boldsymbol{A}_1]\{q^{m+1}\} = \{\boldsymbol{R}_1(\boldsymbol{q}^{m+1}, \dot{\boldsymbol{q}}^{m+1})\}$$
$$[\boldsymbol{A}_2]\{\ddot{\boldsymbol{q}}\}^{m+1} = \{\boldsymbol{R}_2(\boldsymbol{q}^{m+1}, \dot{\boldsymbol{q}}^{m+1})\} \qquad (4.37)$$

where the matrices and right-hand side vectors are defined as

$$[\boldsymbol{A}_1] = [\boldsymbol{M}] + \alpha\Delta t[\boldsymbol{C}] + \frac{1}{2}\gamma(\Delta)^2[\boldsymbol{K}]$$
$$[\boldsymbol{A}_2] = [\boldsymbol{M}] + \alpha\Delta t[\boldsymbol{C}] \qquad (4.38)$$

$$\{\boldsymbol{R_1}\} = ([\boldsymbol{M}] + \alpha\Delta t[\boldsymbol{C}]) \left(\{\boldsymbol{q}\}^{m+1} + \{\dot{\boldsymbol{q}}\}^{m+1}\Delta t + \frac{1}{2}(1-\gamma)(\Delta)^2\{\ddot{\boldsymbol{q}}\}^{m+1}\right)$$

$$+ \frac{1}{2}\gamma(\Delta)^2 \left(\{\boldsymbol{F}(\boldsymbol{q^{m+1}}, \dot{\boldsymbol{q}}^{\boldsymbol{m+1}})\} - [\boldsymbol{C}](\{\dot{\boldsymbol{q}}\}^{m+1} + (1-\alpha)\Delta\{\ddot{\boldsymbol{q}}\}^{m+1}))\right) \quad (4.39)$$

$$\{\boldsymbol{R_2}\} = \{\boldsymbol{F}(\boldsymbol{q^{m+1}}, \dot{\boldsymbol{q}}^{\boldsymbol{m+1}})\} - [\boldsymbol{C}]\left(\{\dot{\boldsymbol{q}}\}^{m+1} + (1-\alpha)\Delta\{\ddot{\boldsymbol{q}}\}^{m+1}\right) - [\boldsymbol{K}]\{\boldsymbol{q}\}$$

The velocity term $\{\dot{\boldsymbol{q}}\}^{m+1}$ is calculated using the following

$$\{\dot{\boldsymbol{q}}\}^{m+1} = \{\dot{\boldsymbol{q}}\}^m + (1-\alpha)\Delta t\{\ddot{\boldsymbol{q}}\}^m + \alpha\Delta t\{\ddot{\boldsymbol{q}}\}^{m+1} \quad (4.40)$$

Equation (4.37) is re-written in terms of $\boldsymbol{q}$ and $\dot{\boldsymbol{q}}$ using Eq. (4.40) as

$$[\boldsymbol{A_1}]\{q^{m+1}\} = \{\boldsymbol{R_1}(\boldsymbol{q}^{m+1}, \dot{\boldsymbol{q}}^{m+1})\}$$

$$[\boldsymbol{A_2}]\{\dot{q}\}^{m+1} = \{\boldsymbol{R_3}(\boldsymbol{q}^{m+1}, \dot{\boldsymbol{q}}^{m+1})\} \quad (4.41)$$

where $\{\boldsymbol{R_3}(\boldsymbol{q}^{m+1}, \dot{\boldsymbol{q}}^{m+1})\}$ is defined as

$$\{\boldsymbol{R_3}(\boldsymbol{q}^{m+1}, \dot{\boldsymbol{q}}^{m+1})\} = \alpha\Delta t\{\boldsymbol{R_2}(\boldsymbol{q}^{m+1}, \dot{\boldsymbol{q}}^{m+1})\} + [\boldsymbol{A_2}]\left(\{\dot{\boldsymbol{q}}\}^m + (1-\alpha)\Delta\{\ddot{\boldsymbol{q}}\}^m\right) \quad (4.42)$$

The proof of the Newmark method are discussed in details in Refs [4, 7]. The loosely coupling can be defined as follows. At each time step, an initial position of the tail motion $\boldsymbol{q}(t_0^m)$ is assumed. Then the hydrodynamic loads, $\boldsymbol{R_1}$ and $\boldsymbol{R_3}$, are calculated based on this configuration. A local iteration is performed until the difference between two successive tail configurations are within the defined convergence criteria. On the other hand, to solve Eq. (4.41) using the strong coupling method, it is re-written as a system of algebraic equations as

$$\boldsymbol{F}(\boldsymbol{z}) = \begin{bmatrix} \boldsymbol{A_1} & 0 \\ 0 & \boldsymbol{A_2} \end{bmatrix} \begin{Bmatrix} \{\boldsymbol{q}\}^{m+1} \\ \{\dot{\boldsymbol{q}}\}^{m+1} \end{Bmatrix} - \begin{Bmatrix} \{\boldsymbol{R_1}\} \\ \{\boldsymbol{R_3}\} \end{Bmatrix} \quad (4.43)$$

where $\{\boldsymbol{z}\} = \{\{\boldsymbol{q}\}^{m+1}, \{\dot{\boldsymbol{q}}\}^{m+1}\}^T$. The local iteration is performed using the Newton-Raphson

method to solve for the variables at $k + 1$ local iteration as

$$\boldsymbol{z}_{k+1}^m = \boldsymbol{z}_{k+1}^m - \left(\frac{\partial \boldsymbol{F}_i}{\partial \boldsymbol{z}_j} |_{\boldsymbol{z}_k^m} \right)^{-1} F(\boldsymbol{z}_k^m) \tag{4.44}$$

The convergence criteria is defined by the displacement vector $\boldsymbol{q}$ for both loosely and strong coupling as

$$\frac{||\boldsymbol{q}_{k+1}^m - \boldsymbol{q}_k^m||}{||\boldsymbol{q}_{k+1}^m||} \leq \epsilon \tag{4.45}$$
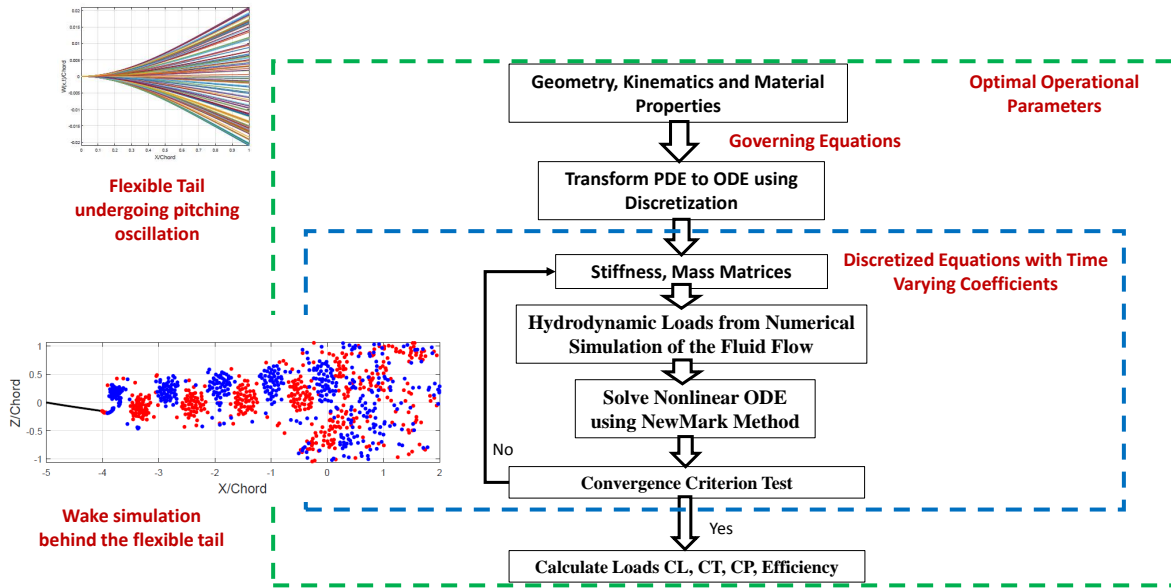
Figure 4.6: Flowchart for the solution of UVLM

When convergence is reached, the tail configuration at the next time step is set to be the one form the last local iteration, i.e. $\boldsymbol{q}(t_0^{m+1}) = \boldsymbol{q}(t_{k+1}^m)$. The procedure used for the local iteration and solving for the instantaneous tail position w is shown in Figure 4.6. A comparison between the rate of convergence between Newton-Raphson and loosely coupling with under relaxation factor $\Theta = 0.1$, is shown in Figure 4.7. It is clearly seen that the Newton-Raphson has much steeper rate of convergence than the loosely coupling method. In addition, the loosely coupling method

converges to a different steady-state value for the maximum deflection of the beam.
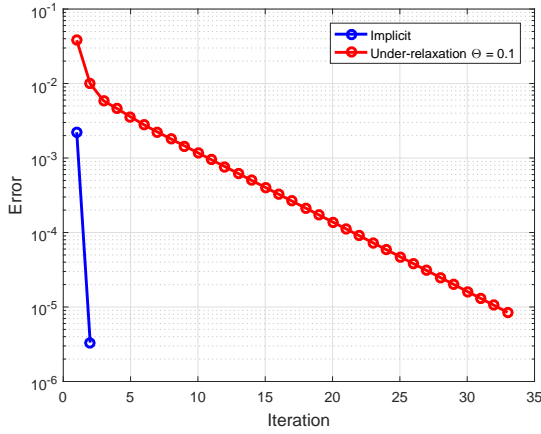
(a) Error history versus number of iterations.
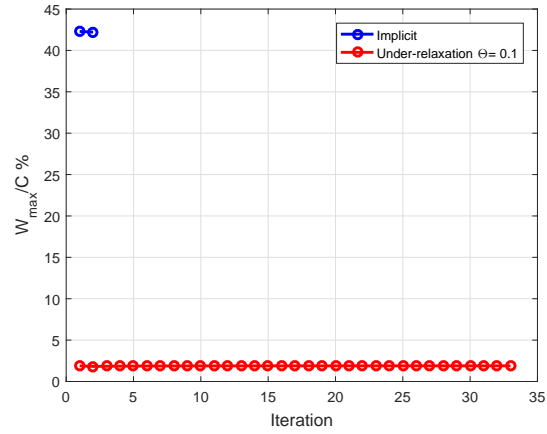
(b) Maximum deflection of the tail beam versus number of iterations.

Figure 4.7: Convergence history using 3D UVLM

4.5 Numerical Data and Results

The values of the tail geometry and material properties used in this study are defined in Table 4.1. The natural frequencies of different tail configurations are calculated in vacuum as given in Table 4.1. In this study, we made some assumptions to simplify the problem. The flexibility in the spanwise direction is neglected. For the 3D ULVM, no vortices are shed from the tail tips. This is not the situation in a general case, i.e. high angle of attack. In addition, only half of the tail is solved to use the symmetrical nature of the problem. We chose a five elements in the chordwise direction based on the efficiency convergence in Figure 4.8. A change of less than 1% in the efficiency is noticed which motivated the use of chordwise panels of $N_x = 5$ and time step of $\Delta t U_\infty / C = 1/(2N_x + 1)$. The code is written using **C++** and compiled to run on Windows platform. The code was run on a desktop computer of i5 processor and 4 GB Ram. The CPU time taken to solve the coupled problem and reach a steady-state to calculate the efficiency points in Figure 4.8 are $1, 2.5, 3, 4$ hours for N_x of $4, 5, 8,$ and 10 respectively.

Table 4.1: Tail Parameters

Parameter	Value
AR	1
$\theta_{max}(deg)$	8
$\omega_1(Hz)$	$85.55, 92.4, 98.78, 110.4$
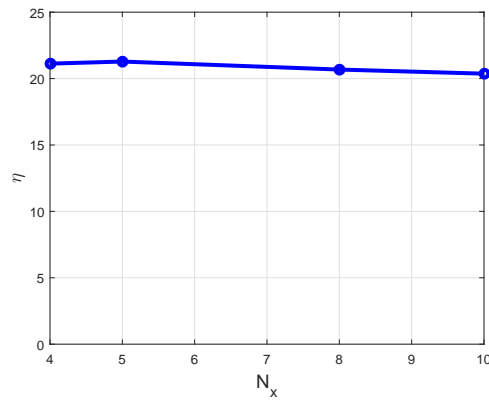
Figure 4.8: Propulsive efficiency versus number of chordwise panels with spanwise panels of $N_y = 10$.

Figure 4.9 shows the thrust and power coefficients, and propulsive efficiency versus Strouhal number for different cases of rigid and active and passive flexible tails using the 2D UVLM for the hydrodynamic load calculation. The thrust coefficient results show that the passive flexible case give more thrust than using mode 1 or 2 or a combination of both. On the other hand, the passive active flexible cases require more power to keep the almost the same propulsive efficiency. Looking at Figure 4.9c, the result suggested that the passive flexible case introduce a slight increase in the propulsive efficiency. However, the inconsistency between the passive and active flexible cases suggested that the two-dimensional UVLM is not suitable to model the chordwise distribution of the hydrodynamic loads at this low aspect ratio, i.e. $AR = 1$. To overcome this drawback, the three-dimensional UVLM is used to model the hydrodynamic loads.

(a) Thrust coefficient versus Strouhal number.

(b) Power coefficeint versus Strouhal number.

(c) Propulsive Efficiency versus Strouhal number.

Figure 4.9: Thrust, and power coefficients , and propulsive efficiency versus Strouhal number for the tail geometrical parameters given in Table 4.1 with grid of $N_x = 5$ using 2D UVLM. The passive flexible tail considered here is for $\omega_1 = 85.55 Hz$

Figure 4.10 shows the thrust and power coefficients, and propulsive efficiency versus Strouhal number for the rigid and passive flexible for different tail flexibilities using the 3D UVLM for the hydrodynamic load calculation.. The natural frequencies of these tails in vacuum are given in Table 4.1. The structural grid used is 4 elements, and the hydrodynamics grid are $Nx = 4$, $Ny = 5$. As seen from Figure 4.10c, the more the flexibility increases the more the propulsive efficiency increases. Unlike the results using the two-dimensional version of the UVLM, the thrust

and power coefficients shown in Figure 4.10(a,b) indicate that the flexible tail gives more thrust and requires slightly more power as the flexibility increases. The same results obtained for a grid of $N_x = 5$ and $N_y = 10$ are shown in Figure 4.11. The same behavior of efficiency improvement is noticed with slightly change in the values as discussed in Figure 4.8.

(a) Thrust coefficient versus Strouhal number.

(b) Power coefficeint versus Strouhal number.

(c) Propulsive Efficiency versus Strouhal number.
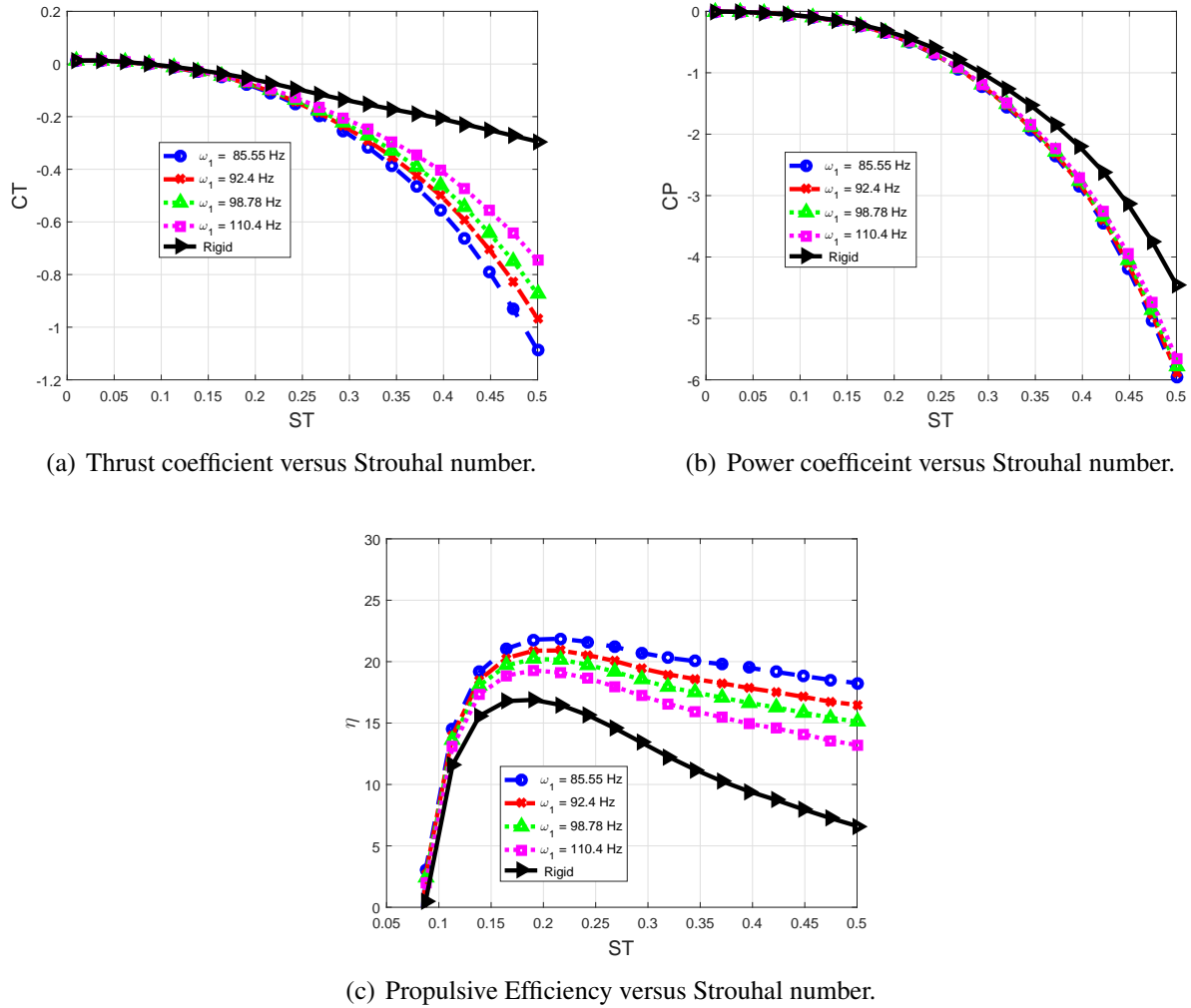
Figure 4.10: Thrust, and power coefficients , and propulsive efficiency versus Strouhal number for the tail parameters given in Table 4.1 with grid of $N_x = 4$, and $N_y = 5$ using 3D UVLM.
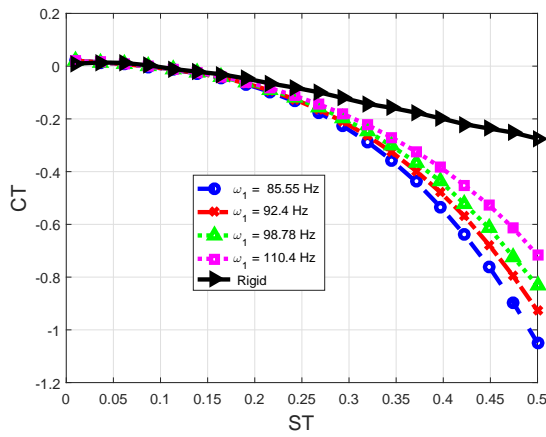
(a) Thrust coefficient versus Strouhal number.
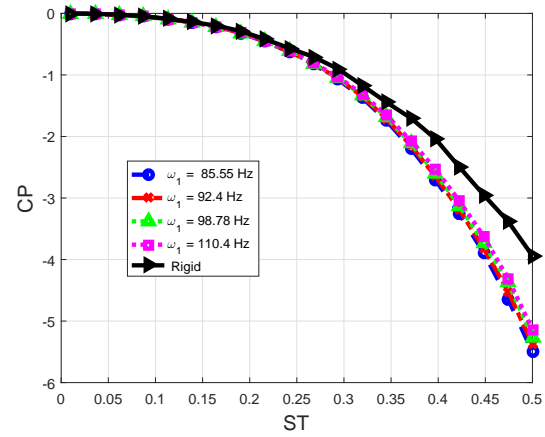
(b) Power coefficeint versus Strouhal number.
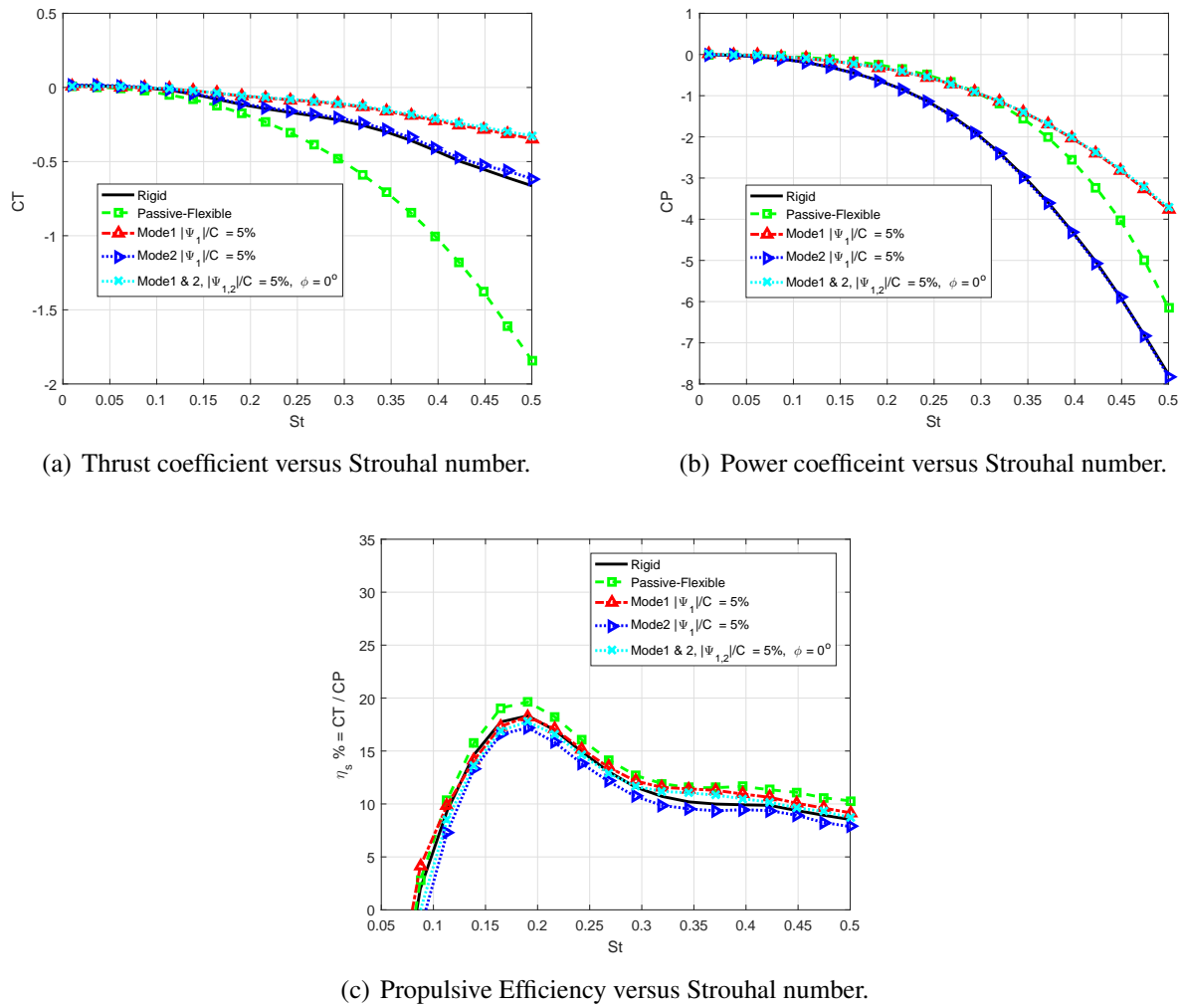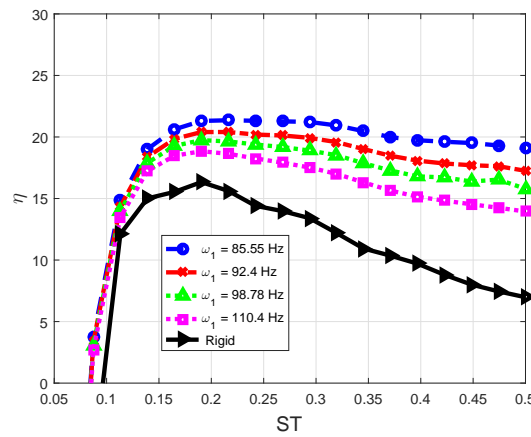

(c) Propulsive Efficiency versus Strouhal number.

Figure 4.11: Thrust, and power coefficients , and propulsive efficiency versus Strouhal number for the tail parameters given in Table 4.1 with grid of $N_x = 5$, and $N_y = 10$.

The time histories of the lift, thrust, and power coefficients at the optimal efficiency for the flexible tail of $\omega_1 = 85.55$ are depicted in Figure 4.12 using the 3D UVLM. As seen from the figure, the mean value of the lift coefficient is zero since the flapping of the tail is of a symmetrical value. The negative value of the mean thrust coefficient indicates that the net force in x direction is pointing to the left, i.e. positive thrust. The sign of the power coefficient is consistent with the thrust calculation such that it leads to a positive values of the propulsive efficiency.

The deflection and velocity of the trailing edge of the tail are shown in Figure 4.13. The maximum

deflection is about 0.7% of the chord length. Also, the maximum the trailing edge velocity does not exceed 5% of the fish traveling speed, i.e. $\dot{z}_{tip} < 5\% u_\infty$. As seen from Figure 4.13, even though there is an overshoot in the starting values of the deflection and velocity, the problem reached a steady-state solution in a few chord travels. This is attributed to the use of the strong coupling method, i.e. Newton-Raphosn method for the local-iteration. This fast convergence behavior is shown in Figure 4.7.
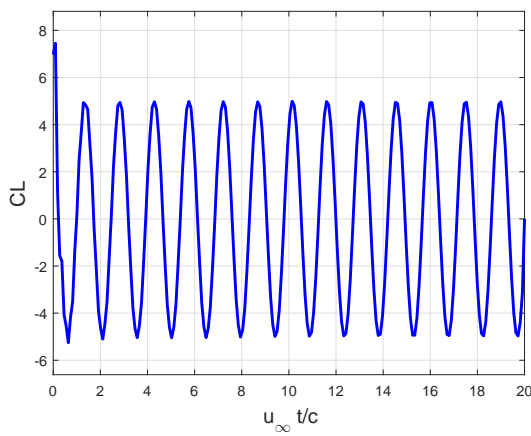
(a) Lift coefficient versus non-dimensional time.
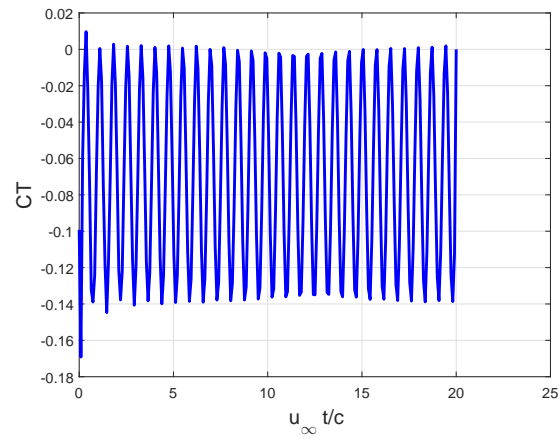
(b) Thrust coefficient versus non-dimensional time.
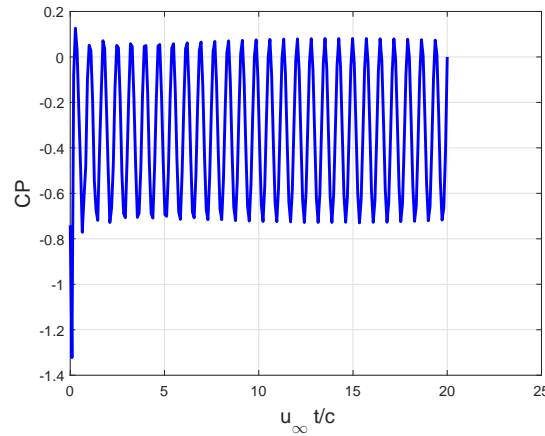
(c) Power coefficient versus non-dimensional time.

Figure 4.12: Time histories of lift, thrust, and power coefficients for the optimal Strouhal number, $St^* = 0.19$, with grid of $N_x = 5$, and $N_y = 10$.
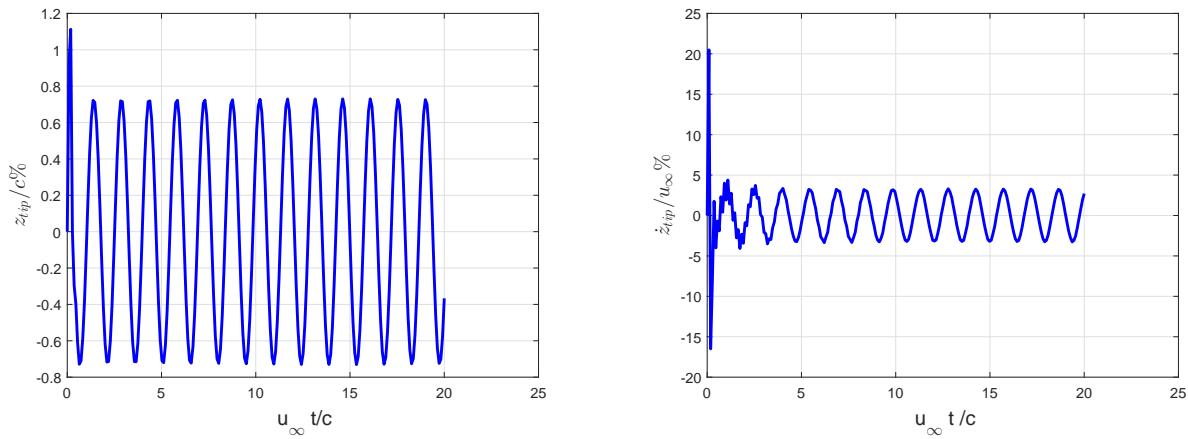
(a) Trailing edge deflection versus non-dimensional time.   (b) Trailing edge velocity versus non-dimensional time.

Figure 4.13: Time histories of deflection and velocity of the trailing edge for the optimal Strouhal number, $St^* = 0.19$, with grid of $N_x = 5$, and $N_y = 10$.

4.6   Conclusion

In this chapter, we solved the fluid-structure interaction problem described by the hydrodynamic loads generated by the motion of a flapping fish tail. We considered a three different cases when using the two-dimensional UVLM. The cases are rigid, active, and passive flexible. The results show that the passive flexible case introduce some enhancement in the propulsive efficiency. However, these improvement was not supported by those of the active flexible ones. To overcome this inconsistency, we used the three-dimensional UVLM to accurately model the hydrodynamics chordwise and spanwise load distributions on the tail. The results showed that the more the flexibility increases the more improvement in propulsive efficiency we have compared to a rigid tail.

Chapter 5

Optimal Transition of FWMAVs from Hovering to Forward Flight

5.1 Introduction

Unlike conventional airplanes, flapping-wing micro-air-vehicles (FWMAVs) move their wings continuously with respect to the body. These new degrees of freedom for the wings trigger questions about the best wing kinematics for optimal aerodynamic performance at specific equilibrium positions or configurations, and/ or maximum maneuverability for transition between these positions. This optimization objective is necessary because of the stringent weight, size, and power constraints imposed on the design of these miniature vehicles.

To date, most investigations regarding aerodynamic-optimum wing kinematics have aimed to optimize hovering or forward flight capabilities. Berman and Wang [77], Kurdi et al. [78], and Taha et al. [79] formulated optimization problems to determine the optimal time variations of the Euler angles, describing flapping kinematics, for hovering with minimum aerodynamic power. Stanford and Beran [80] and Ghommem et al. [81] solved similar problems for optimum aerodynamic performance in forward flight. Still the open literature lacks constructive techniques to determine

68

maneuverability- or control-optimum kinematics. The common approach has been to assume the shape of the kinematic functions from the outset and adapt such a shape to ensure controllability for the FWMAV, see Schenato et al. [82], Doman et al. [83], and Oppenheimer et al. [84]. That is, the kinematic functions are not derived.

Taha et al. [85] proposed a constructive approach for maneuverability-optimum kinematics. They used calculus of variations and optimal control to determine the optimum waveform for the back and forth flapping angle in a horizontal stroke plane and constant angle of attack that results in the maximum cycle-averaged forward acceleration from a hovering position. Since they considered the initial acceleration from a hovering equilibrium, they neglected the body dynamics and, as such, the problem was simplified to a one-degree-of-freedom kinematic optimization problem.

In this work, we formulate a minimum-time optimal control problem to determine the evolution of the optimum wing kinematics that steers the FWMAV dynamical system from a hovering configuration to a forward flight configuration with a prescribed averaged forward speed. The steering problem is investigated using averaged and time-periodic dynamics. In the averaged dynamics formulation, we rely on the large separation between the FWMAV system's two time scales, namely a fast time scale associated with flapping and a slow time scale associated with body motion dynamics, to justify the use of the averaging theorem to convert the time-periodic flapping flight dynamics into a time-invariant system. As such, the periodic orbits representing equilibria of the original time-periodic system are reduced to fixed points. The flapping periodic waveform is parametrized with some parameters that are considered as inputs to the time-averaged dynamics. The parametrization proposed by Berman and Wang [77, 86], which is capable of representing both square and sine functions, is used here. In contrast, the input to the time-periodic system is the flapping speed with no periodicity constraint on the flapping angle. The wing pitching angle η is assumed to be passively controlled with the back and forth flapping angle φ in such a way to maintain a constant angle of attack throughout each half stroke. In fact, this piecewise constant variation of the pitching angle (angle of attack) has been extensively used in the literature of hovering FWMAVs [79, 82–84, 87] as an approach to comply with minimum actuation requirements in FWMAVs, stressed as the main reason for the successful flapping flight of the Harvard

Robofly [88]. The layout of this chapter is as follows. In Section 5.2, the flight dynamical model is briefly discussed, and the averaging dynamics is introduced. In Section 5.3, the procedure for finding the periodic orbits for hovering and forward flight is detailed. The optimal control problem formulation for both averaged and time periodic dynamics is setup in Section 5.4. Results for transitioning between hovering and forward flights with three different speeds for both averaged and time periodic dynamics are presented and discussed in Section 5.5. The last Section 5.6 presents the summary and conclusions.

5.2   Flight Dynamic Model

We use a flight dynamic model that was developed in a previous work by Taha et al. [89, 90] and is based on a quasi-steady formulation that accounts for the dominant leading edge vortex contribution as well as rotational effects. A schematic diagram of the FWMAV performing a horizontal stroke plane is shown in Figure 5.1.

        (a) Top view of the FWMAV.   (b) Side view of the FWMAV.
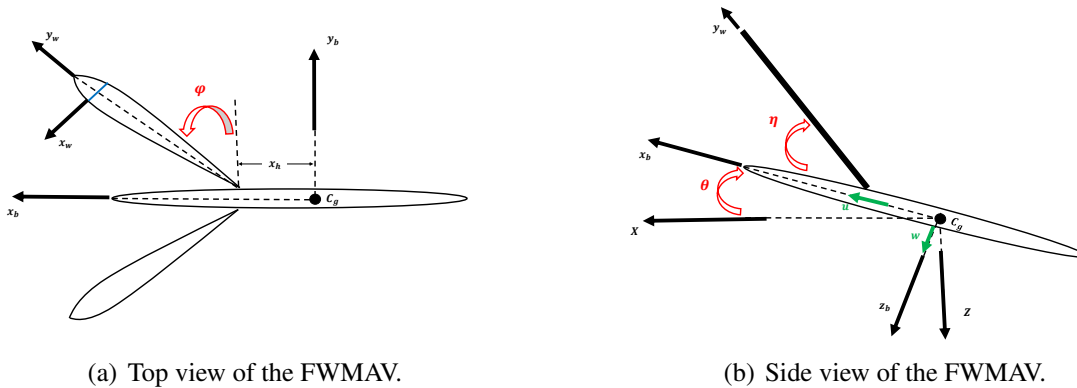
Figure 5.1: Schematic diagram showing the back-and-forth flapping angle φ and the pitching angle of the wing η of the FWMAV.

The time periodic dynamical model is written as

$$
\begin{pmatrix} \dot{u} \\ \dot{w} \\ \dot{q} \\ \dot{\theta} \end{pmatrix} = \begin{pmatrix} -qw - g\sin\theta \\ qu + g\cos\theta \\ 0 \\ q \end{pmatrix} + \begin{pmatrix} \frac{1}{m}X_o(t) \\ \frac{1}{m}Z_o(t) \\ \frac{1}{m}M_o(t) \\ 0 \end{pmatrix} + \begin{pmatrix} X_u(t) & X_w(t) & X_q(t) & 0 \\ Z_u(t) & Z_w(t) & Z_q(t) & 0 \\ M_u(t) & M_w(t) & M_q(t) & 0 \\ 0 & 0 & 0 & 0 \end{pmatrix} \begin{pmatrix} u \\ w \\ q \\ \theta \end{pmatrix}
\tag{5.1}
$$

where u is the forward velocity component along the body x axis, w is the normal velocity component along the body z axis, and θ and q are pitching angle and angular velocity of the body, respectively. In Eq. (5.1), X_0, Z_0 and M_0 are respectively the aerodynamic forces and pitching moment due to flapping that are given by:

$$
\begin{aligned}
X_0(t) &= -2K_{21}\dot{\varphi}(t)|\dot{\varphi}(t)|\cos\varphi(t)\sin^2\eta - \frac{1}{2}\bar{\rho}_bS_bC_{D_b}Vu \\
Z_0(t) &= -K_{21}\dot{\varphi}(t)|\dot{\varphi}(t)|\sin 2\eta - \frac{1}{2}\bar{\rho}_bS_bC_{D_b}Vw \\
M_0(t) &= 2\dot{\varphi}(t)|\dot{\varphi}(t)|\sin\eta(K_{22}\Delta\hat{x}\cos\varphi(t) + K_{21}x_h\cos\eta + K_{31}\sin\varphi(t)\cos\eta
\end{aligned}
\tag{5.2}
$$

where $K_{mn} = 1/2\rho AI_{mn}$, $I_{mn} = 2\int_0^R r^m c^n(r)dr$, $S_b = \pi D_b L_b$ and $D_b/L_b = (4m_b/(\pi\rho_b L_b^3))^{0.5}$. A is the aspect ratio correction defined by

$$
A = \frac{\pi AR}{2\left(1 + \sqrt{(\frac{\pi AR}{ao})^2 + 1}\right)}
\tag{5.3}
$$

The stability derivatives $\bar{X}_u$, $\bar{X}_w$, $\bar{X}_q$, $\bar{Z}_u$, $\bar{Z}_w$, $\bar{Z}_q$, $\bar{M}_u$, $\bar{M}_w$ and $\bar{M}_q$ represent the aerodynamic

loads due to body motion variables. They are given by

$$X_u(t) = -4\frac{K_{11}}{m}|\dot\varphi(t)|\cos^2\varphi(t)\sin^2\eta$$

$$X_w(t) = -\frac{K_{11}}{m}|\dot\varphi(t)|\cos\varphi(t)\sin 2\eta$$

$$X_q(t) = \frac{K_{21}}{m}|\dot\varphi(t)|\sin\varphi(t)\cos\varphi(t)\sin 2\eta - x_h.X_w(t)$$

$$Z_u(t) = 2X_w(t)$$

$$Z_w(t) = -2\frac{K_{11}}{m}|\dot\varphi(t)|\cos^2\eta$$

$$Z_q(t) = 2\frac{K_{21}}{m}|\dot\varphi(t)|\sin\varphi(t)\cos^2\eta - \frac{K_{rot_{12}}}{m}\dot\varphi(t)\cos\varphi(t) - x_hZ_w(t)$$

$$M_u(t) = 4\frac{K_{12}\Delta\hat x}{I_y}|\dot\varphi(t)|\cos^2\varphi(t)\sin\eta + \frac{m}{I_y}(2X_q - x_hZ_u(t))$$

$$M_w(t) = 2\frac{K_{12}\Delta\hat x}{I_y}|\dot\varphi(t)|\cos\varphi(t)\cos\eta + 2\frac{K_{21}}{I_y}|\dot\varphi(t)|\sin\varphi(t)\cos^2\eta - \frac{m.x_h}{I_y}Z_w(t)$$

$$\begin{aligned}M_q(t) = &-\frac{2\Delta x}{I_y}|\dot\varphi(t)|\cos\varphi(t)\cos\eta(K_{12}x_h + K_{22}\sin\varphi(t))\\ &+ \frac{1}{I_y}\dot\varphi(t)\cos\varphi(t)(K_{rot_{13}}\Delta\hat x\cos\varphi(t)\cos\eta + K_{rot_{22}}\sin\varphi(t))\\ &- \frac{2}{I_y}|\dot\varphi(t)|\cos^2\eta\sin\varphi(t)(K_{21}x_h + K_{31}\sin\varphi(t)) - \frac{K_v\mu_1 f}{I_y}\cos^2\varphi(t) - \frac{mx_h}{I_y}Z_q(t)\end{aligned}$$

where $K_{rot_{mn}} = \pi\rho(1/2 - \Delta\hat x)I_{mn}$ and $K_v = \pi/16\rho I_{04}$.

Equation (5.1) can be written in an abstract form as

$$\dot{\boldsymbol x} = \boldsymbol f(\boldsymbol x) + \boldsymbol g(\boldsymbol x, \varphi(t)) \tag{5.4}$$

where the state vector $\boldsymbol x = [u, w, q, \theta]^T$, $\boldsymbol f$ represents the inertial and gravitational forces, and $\boldsymbol g$ represents the time-periodic aerodynamic loads that are written affine in the state variables.

5.3   System Equilibrium Representations

Because FWMAVs are continuously subjected to oscillatory forces, their equilibrium states are described by by periodic orbits rather than fixed points. In this work, we use the optimized shooting method proposed by Botha and Dednam [91] to capture the different periodic solutions of the system (5.4). The method is described in detail in Appendix B. The resulting periodic states, inertial velocities, and trajectories are respectively shown in Figures 5.2 and 5.3. The periodic orbits for hovering and forward flight are represented in the state space (u, w, q) in Figure 5.4, and the red dots are the initial conditions presented in Table 5.1. The Floquet theorem used to assess the stability of the obtained periodic orbits is discussed in Appendix B.3 and applied to the cases in this work. On the other hand, very convenient way of transforming the NLTP system in Eq. (5.1) to a representative time-invariant system is the averaging approach. This approach is mainly based on the assumption that, due to the very fast flapping frequency relative to the body dynamics, the body only feels the average values of the aerodynamic loads. It should be noted that the ratio of the flapping frequency to the body natural frequency for the one of the slowest flapping insects (Hawkmoth) is about 30 [90]. For a man made FWMAVs (e.g., Harvard Robofly), this ratio may be as high as 120. In fact, the averaging approach is mathematically justified through the averaging theorem in Appendix B. This averaging approach greatly simplifies the trim (equilibrium) problem as the equilibrium periodic orbit is reduced to a fixed point for the averaged dynamics. Therefore, instead of finding a periodic solution $\chi(t)$ that satisfies the differential equation (5.1) such that it satisfies certain conditions (e.g., the mean velocities are zeros at hover), one has to solve an algebraic equation for the corresponding fixed point of the averaged dynamics.

(a) Velocity u versus non-dimensional time

(b) Velocity w versus non-dimensional time

(c) Angular velocity q versus non-dimensional time

(d) Orientation θ versus non-dimensional time
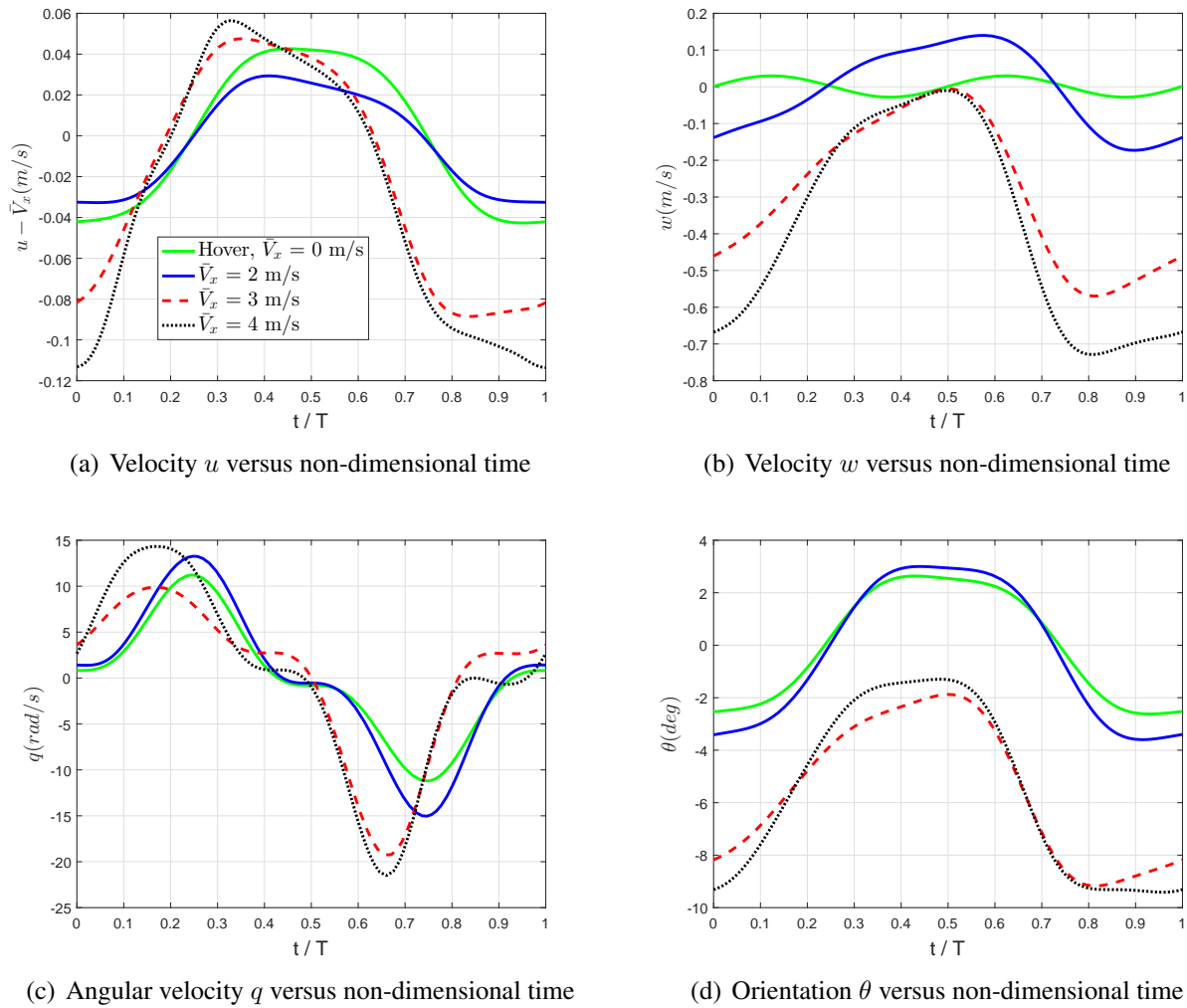
Figure 5.2: Time history of body variables for hovering and forward periodic orbits

With the C_g position aligned with the hinge location, symmetric flapping ($\alpha_d = \alpha_u$ and $a_0 = b_1 = 0$), ensures trim of the forward (X) force and pitching moment at hover with $\bar{\theta} = 0$ [84, 92], as shown in Figure 5.2 and Table 5.1. We also infer that the forward thrust force needed to propel the FWMAV/insect forward to overcome the body drag can be achieved by two mechanisms: (i) asymmetric-drag ($\alpha_d < \alpha_u$) [85] and (ii) forward body pitching like helicopters ($\bar{\theta} < 0$). To transition from hovering to to a small-speed forward flight in minimum time, the second approach might not be the best because of the time taken to pitch the inertia of the whole body; asymmetric drag is sufficient in this case and would achieve it faster. Therefore, the numerical shooting algorithm

yielded the first mechanism at smaller forward speeds (e.g., $\bar{V}_x = 2m/s$). However, because this mechanism would not be sufficient at larger forward speeds (e.g., $\bar{V}_x = 3, 4m/s$), the numerical shooting algorithm would opt for the second mechanism at these speeds.

(a) Inertial forward velocity V_x versus non-dimensional time

(b) Inertial downward velocity V_z versus non-dimensional time

(c) Trajectory for hovering orbit

(d) Trajectory for forward orbit
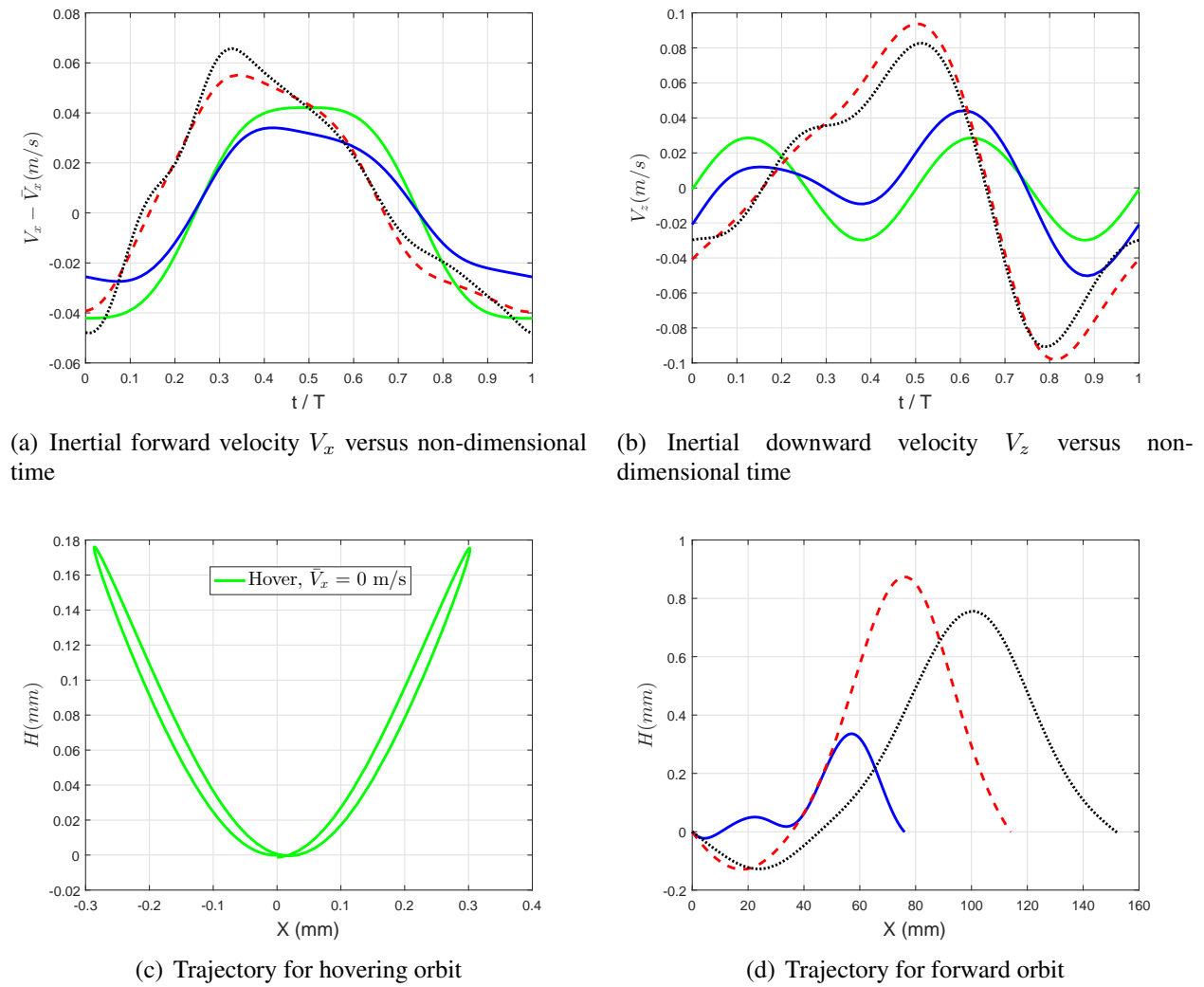
Figure 5.3: Inertial velocities and trajectories for hovering and forward periodic orbits
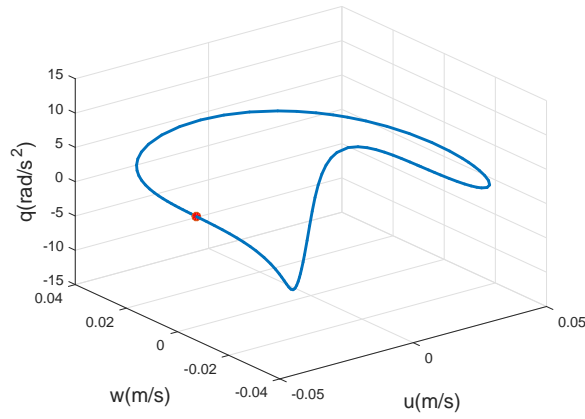
(a) Periodic orbit for hovering flight in the three dimensional state space
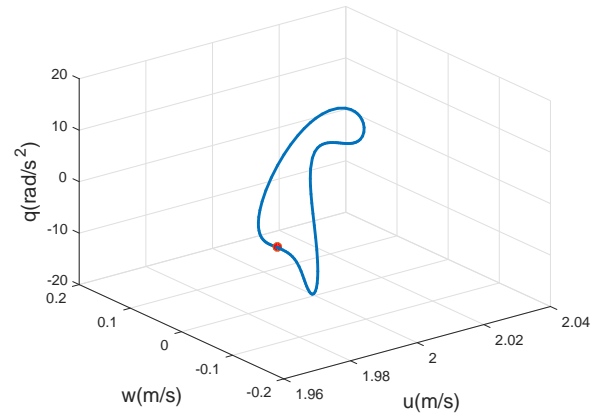
(b) Periodic orbit for forward flight of $\bar{V}_x = 2m/s$ in the three dimensional state space
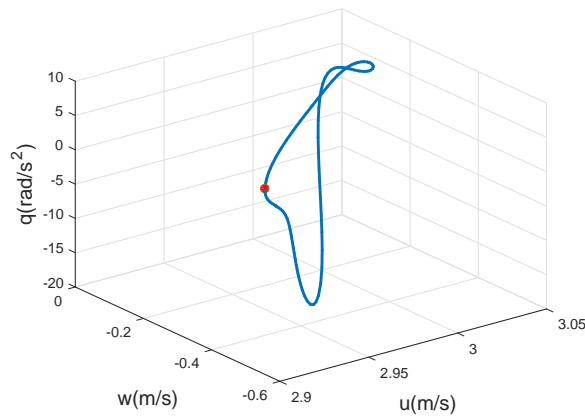
(c) Periodic orbit for forward flight of $\bar{V}_x = 3m/s$ in the three dimensional state space
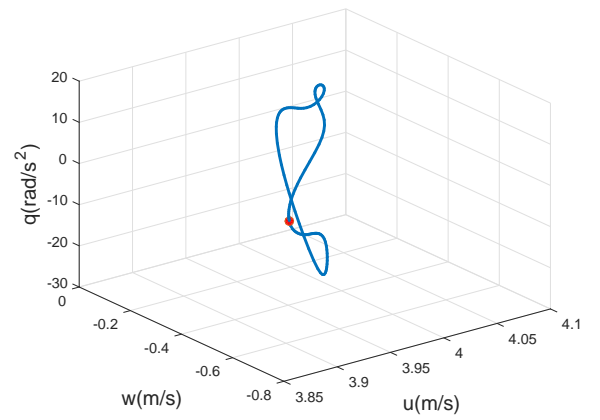
(d) Periodic orbit for forward flight of $\bar{V}_x = 4m/s$ in the three dimensional state space

Figure 5.4: Periodic orbits for hovering and forward flight for three different cases

Table 5.1: Initial conditions for periodic orbit.

State	**Hover,** $\bar{V}_x = 0m/s$	$\bar{V}_x = 2m/s$	$\bar{V}_x = 3m/s$	$\bar{V}_x = 4m/s$
$u(m/s)$	-0.0421	1.9257	2.9184	3.8869
$w(m/s)$	0.0011	-0.27214	-0.4608	-0.6678
$q(rad/s)$	0.8175	3.4996	0.0361	3.6231
$\theta(deg)$	-2.5361	-6.9204	-8.1791	-9.3161
$a_o(deg)$	0	0.2151	1.1571	2.3124
$a_1(deg)$	62.3225	59.451	70.8202	86.0717
$b_1(deg)$	0	-31.5079	-40.1817	-50.2671
$\alpha_u(deg)$	0.4659	63.7915	68.3635	72.6631
$\alpha_d(deg)$	0.4659	23.2384	15.9856	10.8691

To assess the stability of the periodic orbit, we solved the system of equations defined in Eqs. (5.4) and (B.25). The eigenvalues of the state transition matrix at $t = T$, $\Xi(T)$, are the Floquet multipliers z. They are tabulated in Table 5.2 for hovering and three different cases of forward flight.

Table 5.2: Floquet Multipliers z for Hovering and Forward Flight

$\bar{V}_x = 0$	$\bar{V}_x = 2m/s$	$\bar{V}_x = 3m/s$	$\bar{V}_x = 4m/s$
$\begin{Bmatrix} 1.0920 \\ 0.8416 \\ 0.8229 \\ 0.6501 \end{Bmatrix}$	$\begin{Bmatrix} 1.1301 \\ 0.8370 \\ 0.6922 \\ 0.4834 \end{Bmatrix}$	$\begin{Bmatrix} 1.0884 + 0.0000i \\ 0.8278 + 0.0000i \\ 0.6249 + 0.0755i \\ 0.6249 - 0.0755i \end{Bmatrix}$	$\begin{Bmatrix} 1.0649 + 0.0000i \\ 0.8363 + 0.0000i \\ 0.5589 + 0.1285i \\ 0.5589 - 0.1285i \end{Bmatrix}$

Looking at the Floquet multipliers, it is found that the periodic orbits for hovering and forward flight are unstable, consistent with previous studies on flapping flight stability [93]. To make it clearer, the Floquet multipliers are plotted versus the unit circle in the complex plane in Figure 5.5. It is shown that each case has a Floquet multiplier outside the unit circle.
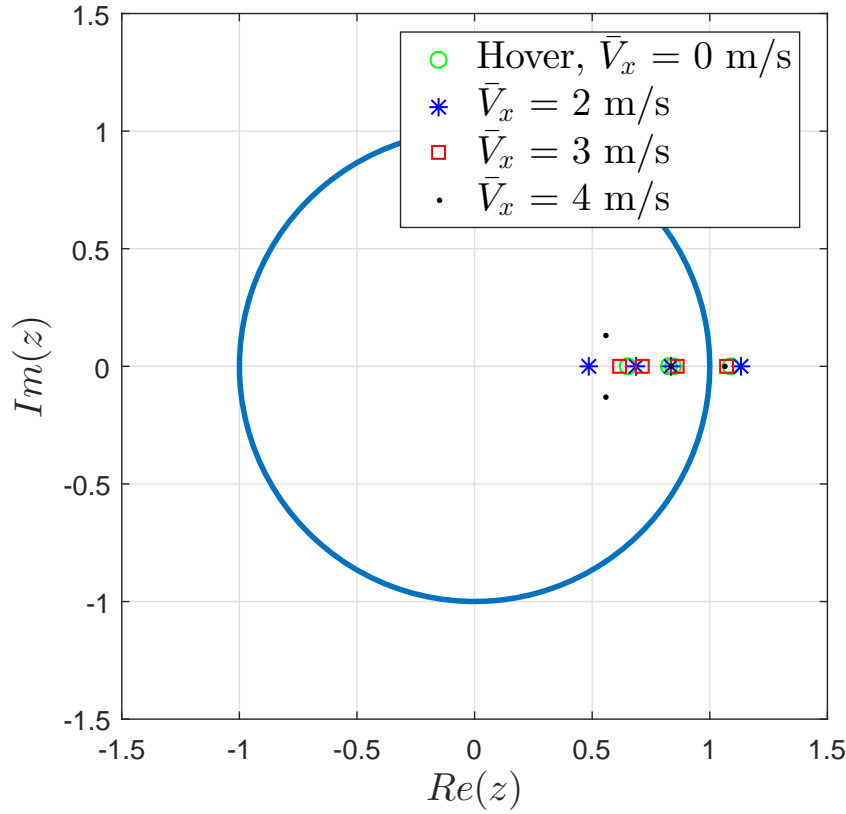
Figure 5.5: Floquet multipliers for hovering and forward flight periodic orbits in the complex plane with respect to the unit circle.

However, because the system is nonlinear, a desired equilibrium (e.g., hovering) may have different solutions, possibly with different stability characteristics. Figure 5.6 shows four different hovering periodic orbits along with their Floquet multipliers. Although the four orbits are close to each other, they possess qualitatively different stability characteristics; three are stable and one is unstable. The values of the Floquet multipliers are shown in Table 5.3.

Table 5.3: Floquet Multipliers z for Hovering flight for a different initial conditions

$$\begin{Bmatrix} 1.0925 \\ 0.6501 \\ 0.8222 \\ 0.8415 \end{Bmatrix} \begin{Bmatrix} 0.7135 \\ 0.9647 + 0.0922i \\ 0.9647 - 0.0922i \\ 0.8823 \end{Bmatrix} \begin{Bmatrix} 0.698 \\ 0.9838 + 0.1744i \\ 0.9838 - 0.1744i \\ 0.9154 \end{Bmatrix} \begin{Bmatrix} 0.7 \\ 0.9825 + 0.1699i \\ 0.9825 - 0.1699i \\ 0.9127 \end{Bmatrix}$$

(a) Floquet multipliers for hovering orbits

(b) Trajectories for the hovering orbits
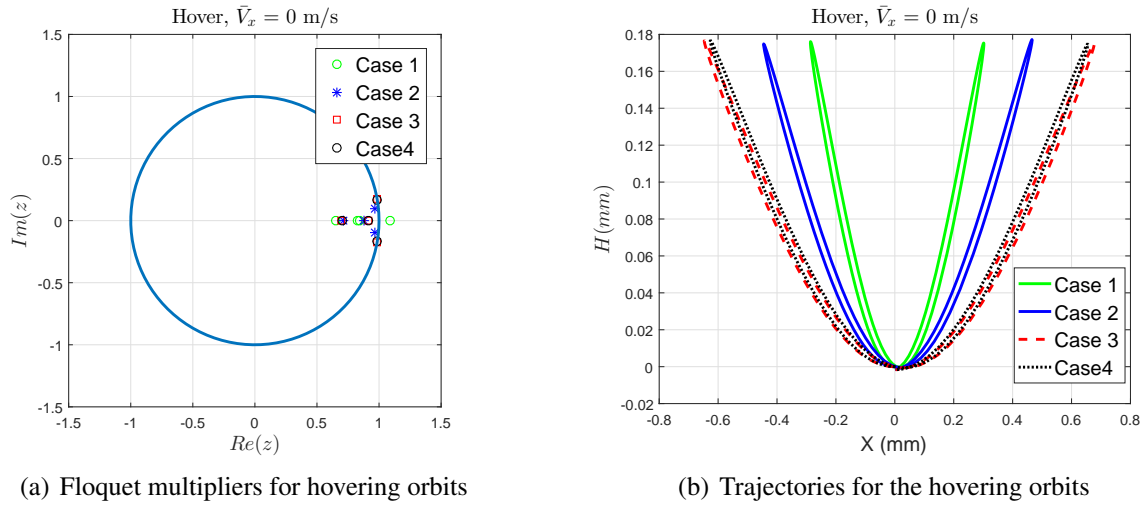
Figure 5.6: Floquet multipliers and trajectory for hovering orbit for different cases of initial conditions.

5.4 Optimal Control Formulation

In this section we introduce the optimal control problem formulation for both averaged and time-periodic dynamics.

5.4.1 Averaged Dynamics

The averaged dynamics are not affected by the full variation of the flapping angle over the cycle but some integrals of such a waveform φ. We use a parametrization for the flapping angle defined by Bhatia et al.[86]. This function was first introduced by Berman and Wang [77] for the symmetric flapping during hovering and was later modified by Doman et al. [94] to account for asymmetric flapping and continuity between cycles. We adopt the function of Bhatia et al. [86], which differs from Doman et al.[94] in how the continuity criteria is defined. The flapping angle without the continuity criteria of Bhatia et al.[94] is adopted at this stage as it will be shown later that no feasible solution is obtained when using this criteria. The flapping angle can be defined as follows:

$$\varphi(\tau) = \begin{cases} \phi_m \dfrac{sin^{-1}\{K_\phi sin[(\omega-\delta)\tau+\pi/2]\}}{sin^{-1}K_\phi} + \phi_0, & 0 \leqq \tau \leqq \frac{\pi}{\omega-\delta} \\[2em] \phi_m \dfrac{sin^{-1}\{K_\phi sin[\tilde{\omega}\tau+\tilde{\zeta}+\pi/2]\}}{sin^{-1}K_\phi} + \phi_0, & \frac{\pi}{\omega-\delta} \leqq \tau \leqq \frac{2\pi}{\omega} \end{cases} \tag{5.5}$$

where $\tilde{\omega} = \frac{\omega(\omega-\delta)}{\omega-2\delta}$, $\tilde{\zeta} = \frac{-2\pi\delta}{\omega-2\delta}$, and τ is the fast time scale. δ is the reduction in wing-stroke frequency during first half of stroke-cycle, and $\tilde{\zeta}$ is the phase shift with frequency $\tilde{\omega}$ during second half of stroke cycle. Equation (5.5) allows for more choices for the resulting shape of the flapping angle using only four inputs. The input that controls the shape of the waveform is K_ϕ. The value of $K_\phi = 1$ represents a triangular function while the case of $K_\phi \ll 1$ represents a sinusoidal function. In addition, the angle of attack η is defined as

$$\eta(\tau) = \begin{cases} \alpha_d & \dot{\varphi}(\tau) > 0 \\[1.5em] \pi - \alpha_u, & \dot{\varphi}(\tau) < 0 \end{cases} \tag{5.6}$$

If we substitute for φ from Eq. (5.5) and Eq. (5.6) into the aerodynamic loads (e.g., X_0-M_0 and stability derivatives) and then integrate the outcomes to obtain the corresponding cycle-averaged quantities (e.g., $\bar{X}_0$-$\bar{M}_0$ and cycle-averaged stability derivatives), the averaged dynamics (B.5) is written as

$$\dot{\bar{\boldsymbol{x}}}(t) = \boldsymbol{F}(\bar{\boldsymbol{x}}(t), \boldsymbol{U}(t)) \tag{5.7}$$

where $\boldsymbol{U} = [\delta, \ \phi_0, \ \phi_m, \ K_\phi, \ \alpha_u, \ \alpha_d]$ contains the coefficients of the flapping angle φ that are slowly time-varying for a varying waveform during a maneuver execution and angles of attack during the upstroke and down stroke respectively. That is, the parameters $\boldsymbol{U} = [\delta, \ \phi_0, \ \phi_m, \ K_\phi, \ \alpha_u, \ \alpha_d]$ are seen as virtual inputs to the averaged dynamics. The steering takes place between two fixed points, the origin and the final forward conditions. The minimum-time optimal control problem for the averaged dynamics is defined as follows :

$$min \ J(\boldsymbol{U}(.)) = \int_0^{t_f^*} 1dt = t_f^* \tag{5.8}$$

subjected to the control constraint

$$\boldsymbol{U}_l \leq \boldsymbol{U}(t) \leq \boldsymbol{U}_u \tag{5.9}$$

that satisfies the differential equation (5.7) subject to end constraints

$$\begin{aligned}
\bar{V}_x(t_f^*) &= V_f \\
\bar{V}_z(t_f^*) &= 0, \ \bar{q}(t_f^*) = 0
\end{aligned} \tag{5.10}$$

and path constraint

$$\varphi_l \leq \varphi \leq \varphi_u \tag{5.11}$$

to ensure a realistic flapping angle. The end constraint $\dot{\bar{\boldsymbol{x}}}(t_f^*) = 0$ is introduced to ensure equilibrium of the averaged dynamics at the final conditions. The final time is unknown and should be obtained along with the solution of the optimal control problem.

5.4.2   Time-Periodic Dynamics

Since the optimal control theory allows piecewise variation of the control input to achieve realistic flapping, the flapping speed $\dot{\varphi}$ and pitching angle of the wing η are considered as the inputs to the time-periodic dynamics. As such, the flapping angle is treated as one of the dynamics states. Recalling Eq. (5.1), the nonlinear time-periodic system (5.4) is rewritten as

$$\frac{d}{dt}\begin{bmatrix} \boldsymbol{x} \\ \varphi \end{bmatrix} = \begin{bmatrix} \boldsymbol{f}(\boldsymbol{x}) + \boldsymbol{g}(\boldsymbol{x}, \dot{\varphi}(t), \eta(t)) \\ \dot{\varphi} \end{bmatrix} \tag{5.12}$$

where $\dot{\varphi}$ is the input flapping velocity, and η is the input angle of attack. Equation (5.12) can be reduced to the form

$$\dot{\boldsymbol{\chi}}(t) = \boldsymbol{F}(\boldsymbol{\chi}(t), \boldsymbol{U}(t)) \tag{5.13}$$

where $\boldsymbol{\chi} = [u, w, q, \theta, \varphi]^T$, and $\boldsymbol{U} = [\dot{\phi}, \eta]^T$. The steering from hovering to forward flight now takes place between two periodic orbits rather than two fixed points as in the last subsection. The optimal control problem is to find a piecewise continuous control $\boldsymbol{U}(.) : [0, t_f^*] \rightarrow \boldsymbol{\Theta}$ (admissible control set), that steers the system (5.13) from the hovering orbit to the forward periodic orbit in a minimum time. The assumed initial conditions for the hovering and forward periodic orbits for different average forward speeds are presented in Table 5.1.The optimal control problem for the time periodic dynamics can be defined as follows :

$$min \ J(U(.)) = \int_0^{t_f^*} 1 dt = t_f^* \tag{5.14}$$

that satisfies the differential equation (5.12) subject to the initial and final constraints

$$\boldsymbol{\chi}(t_o) = [u_o, \ w_o, \ q_o, \ \theta_o, \ \varphi_o]$$
$$\boldsymbol{\chi}(t_f^*) = [u_f, \ w_f, \ q_f, \ \theta_f, \ \varphi_f] \tag{5.15}$$

subjected to the control constraint

$$\boldsymbol{\Theta}_l \leq \boldsymbol{U}(t) \leq \boldsymbol{\Theta}_u \tag{5.16}$$

and path constraints

$$\varphi_l \leq \varphi \leq \varphi_u \tag{5.17}$$

The end points at t_o and t_f^* are the initial conditions of the hovering and forward orbits respectively, i.e. the red dots in Figure 5.4. The bounds on the states and input are given in Table 5.4.

Table 5.4: Input and State Bounds

Variable	Lower Bound	Upper Bound
$\varphi_{min,max} (rad)$	$-\pi/2$	$\pi/2$
$[U_\varphi(= \dot{\varphi})] \ (rad/s)$	$-\pi^2 f$	$\pi^2 f$
$[\alpha_u, \ \alpha_d] \ (rad)$	$-\pi/2$	$\pi/2$

5.5   Solution of the Optimal Control Problem

The optimal control problem for time-periodic and averaged dynamics defined in the previous section is then solved using **ICLOCS** [1] software.We adopted hawkmoth morphological parameters presented in Table 5.5.

Table 5.5: Hawkmoth parameters

Constant	Value	Constant	Value
$\bar{r}_1$	0.44	m_b	$1.648(mg)$
$\bar{r}_2$	0.508	I_y	$2.08(g/cm^2)$
a_0	2π	f	$26.3(Hz)$
S_w	$947.8(cm^2)$	$\Delta\hat{x}$	0.05
R	$51.9(mm)$	Φ	60.5^o
$\bar{c}$	$18.3(mm)$	C_{D_b}	0.7
D_b/L_b	0.81	$\bar{\rho}_b$	$1100(Kg/m^3)$

Figure 5.7 shows the resulting optimal control inputs in terms of the flapping waveform and angles of attack during the upstroke and down stroke for the averaged dynamics. It shows a discontinuity in the flapping angle between the first two and last three cycles. It should be noted that no feasible solution that satisfies all the boundary and equilibrium constraints was obtained when imposing a continuity constraint. Furthermore, although the two side limits of the flapping speed at the end of the fourth cycle are equal (zero), the derivative ($\dot{\varphi}$) does not exist at this point because the function φ is not continuous. Figure 5.8 shows a comparison between the averaged-formulation minimum time transition between hovering and forward flight for $\bar{V}_x = 2m/s$ and the simulation of the time periodic system (5.4) using the obtained optimal flapping parameters. The discrepancy between the two results point out that averaging is not suitable for designing the steering controller. Because the transition occurs on a short time-scale (over few cycles), a fast variation (within the flapping cycle) in control inputs may be needed.

---

[1] Imperial College London optimal control software
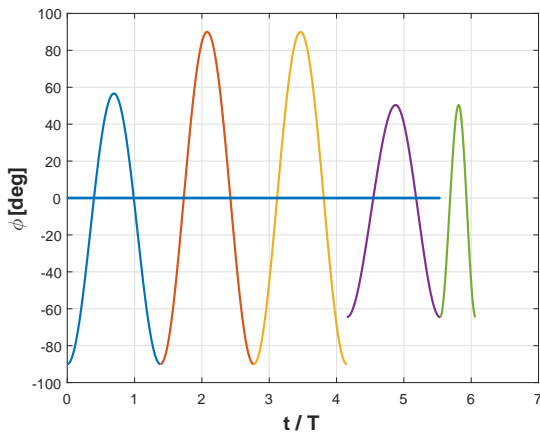
(a) Flapping angle ϕ versus non-dimensional time
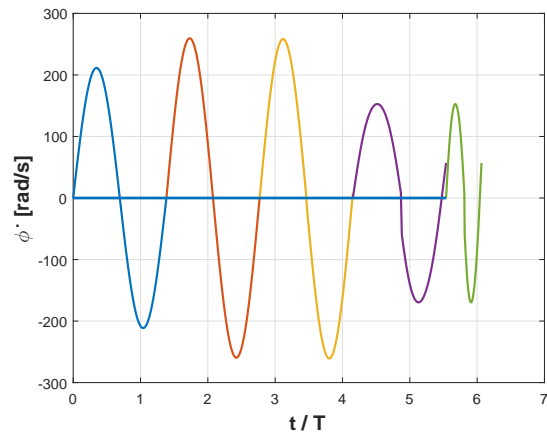
(b) Flapping speed $\dot{\phi}$ versus non-dimensional time
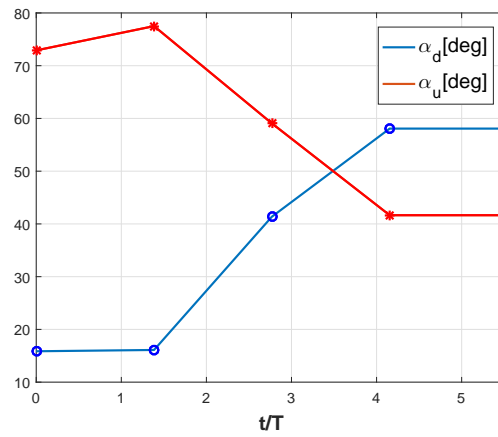
(c) Downstroke and upstroke angles of attack α_d, α_u versus non-dimensional time

Figure 5.7: Time history of flapping angle and speed during transition from hovering to forward flight of $\bar{V}_x = 2m/s$ using the average dynamics in Eq. (5.7)
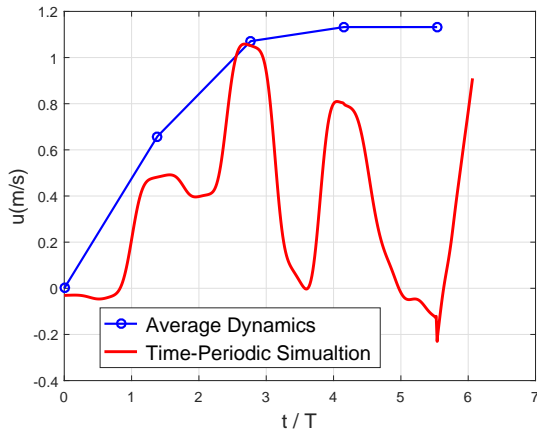
(a) Velocity U versus non-dimensional time
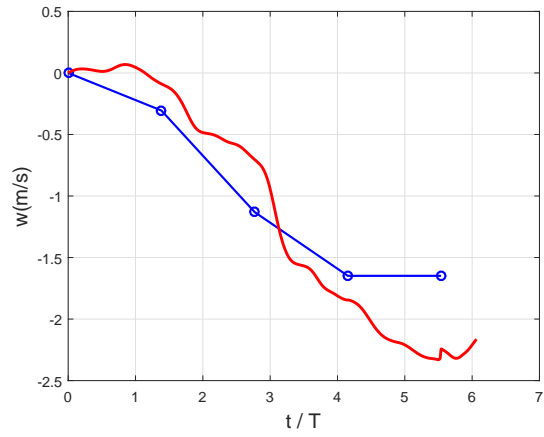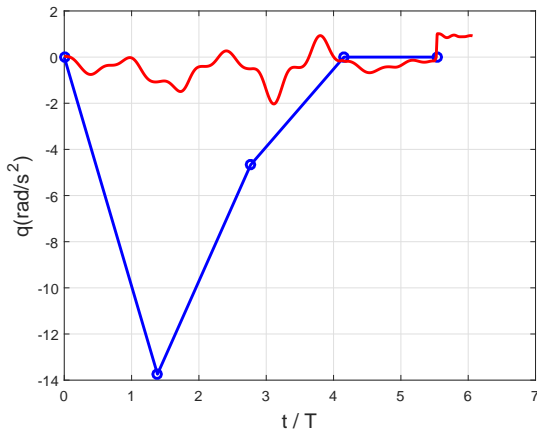
(b) Velocity W versus non-dimensional time

(c) Angular velocity q versus non-dimensional time
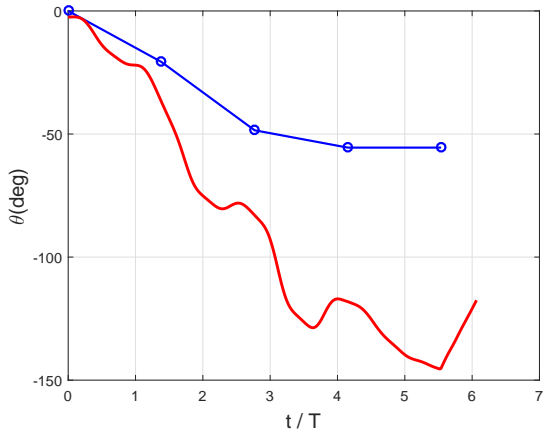
(d) Orientation θ versus non-dimensional time
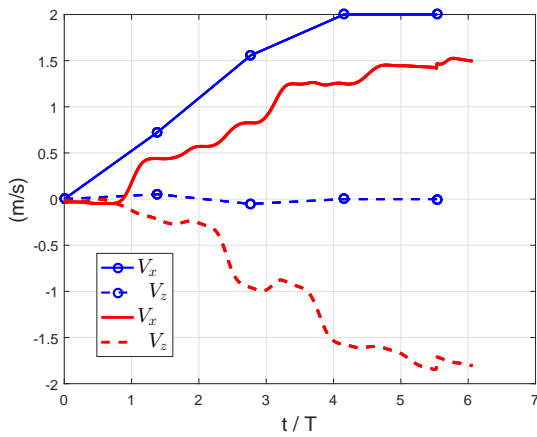
(e) Inertial velocities V_x and V_z versus non-dimensional time
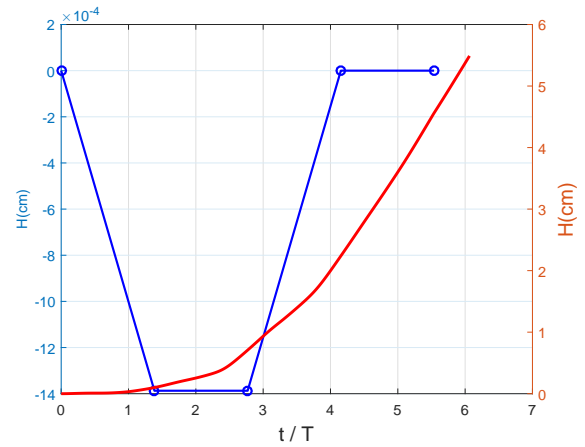
(f) Trajectory

Figure 5.8: Time history of inertial velocities, and trajectories during transition from hovering to forward flight of $\bar{V}_x = 2m/s$ using the average dynamics in Eq. (5.7)

Figure 5.9 depicts the time histories of the body states and trajectories using the time periodic dynamics obtained for three cases of average forward speed. As noted from Figure 5.9, the FWMAV needs more time to achieve the transition form hovering to forward flight as the average forward speed increases. As seen from Figure 5.9(b,d), the FWMAV chooses the same thrust mechanism discussed earlier during the transition between hovering and forward flight. In other words, the more forward speed, the more energy taken from pitching down the body like helicopters.

Figure 5.10 shows the inertial velocities and trajectories for transition from hovering to three cases of forward speeds. In Figures 5.10b, it is seen that the optimizer chose to gain the kinetic energy to move FWMAV with an average speeds of $\bar{V}_x = 2m/s, 3m/s$ through climbing and gaining the necessary potential energy. On the contrary, since the transition time is relativity higher in the case of $\bar{V}_x = 4m/s$, the optimizer oscillates between gaining kinetic and potential energy though descending and climbing. At the end, the FWMAV returns to the horizontal level it started from.

Figure 5.11 shows the time history of the input $\dot{\varphi}, \eta$ to the time periodic dynamics. The flapping angle φ is obtained by integrating the input $\dot{\varphi}$. Since the formulation of the problem is a minimum time control problem with upper and lower bounds on the controllers, we can see the bang-bang nature of the input signals. The frequency of the flapping angle φ is allowed to increase as long as the flapping speed does not exceed its bounds.
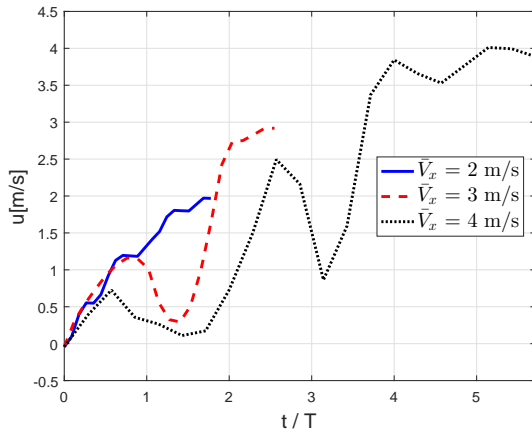
(a) Velocity U versus non-dimensional time
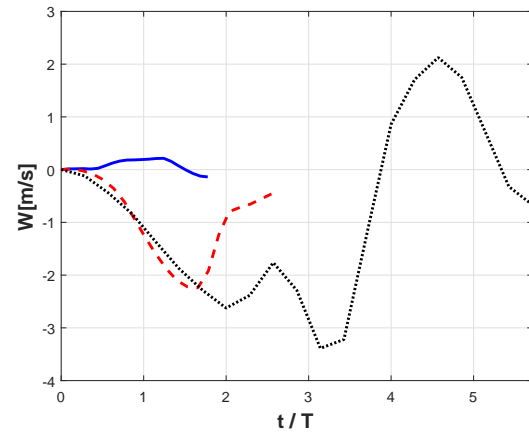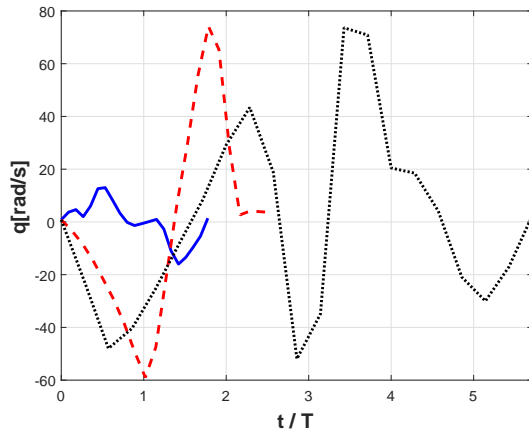
(b) Velocity W versus non-dimensional time

(c) Angular velocity q versus non-dimensional time
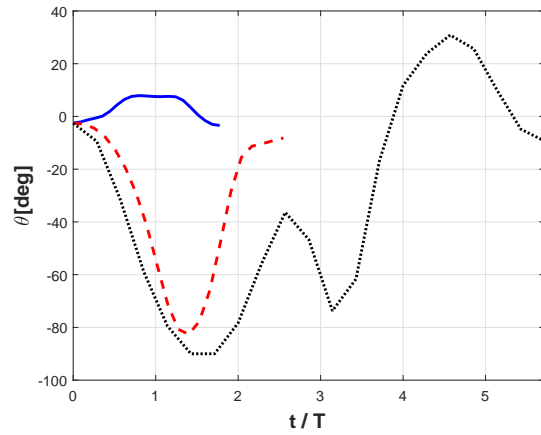
(d) Orientation θ versus non-dimensional time

Figure 5.9: Time history of body variables during transition from hovering to three different cases of forward flight using the time periodic dynamics in Eq.(5.4)
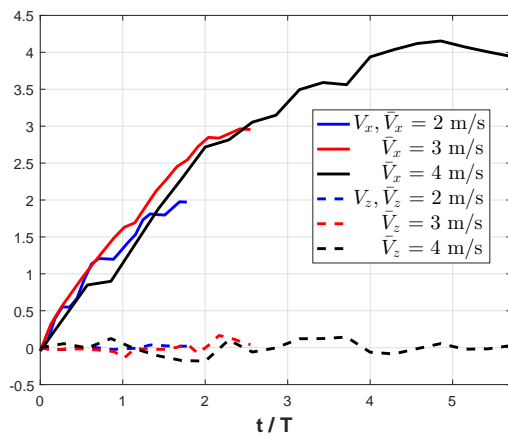
(a) Inertial velocities V_x and V_z versus non-dimensional time
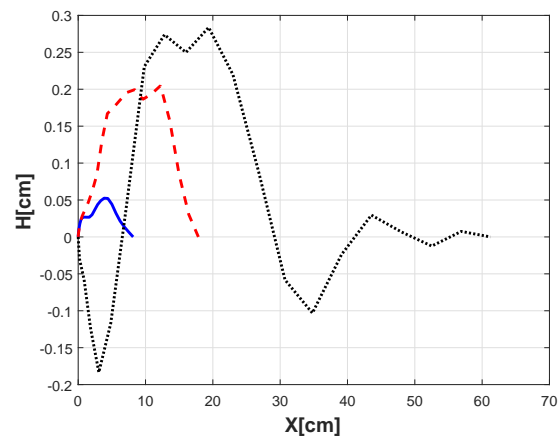
(b) Trajectory

Figure 5.10: Time history of inertial velocities, and trajectories during transition from hovering to three different cases of forward flight using the time periodic dynamics in Eq.(5.4)

(a) Flapping angle ϕ versus non-dimensional time

(b) Flapping speed $\dot{\phi}$ versus non-dimensional time

(c) Angle of attack η versus non-dimensional time
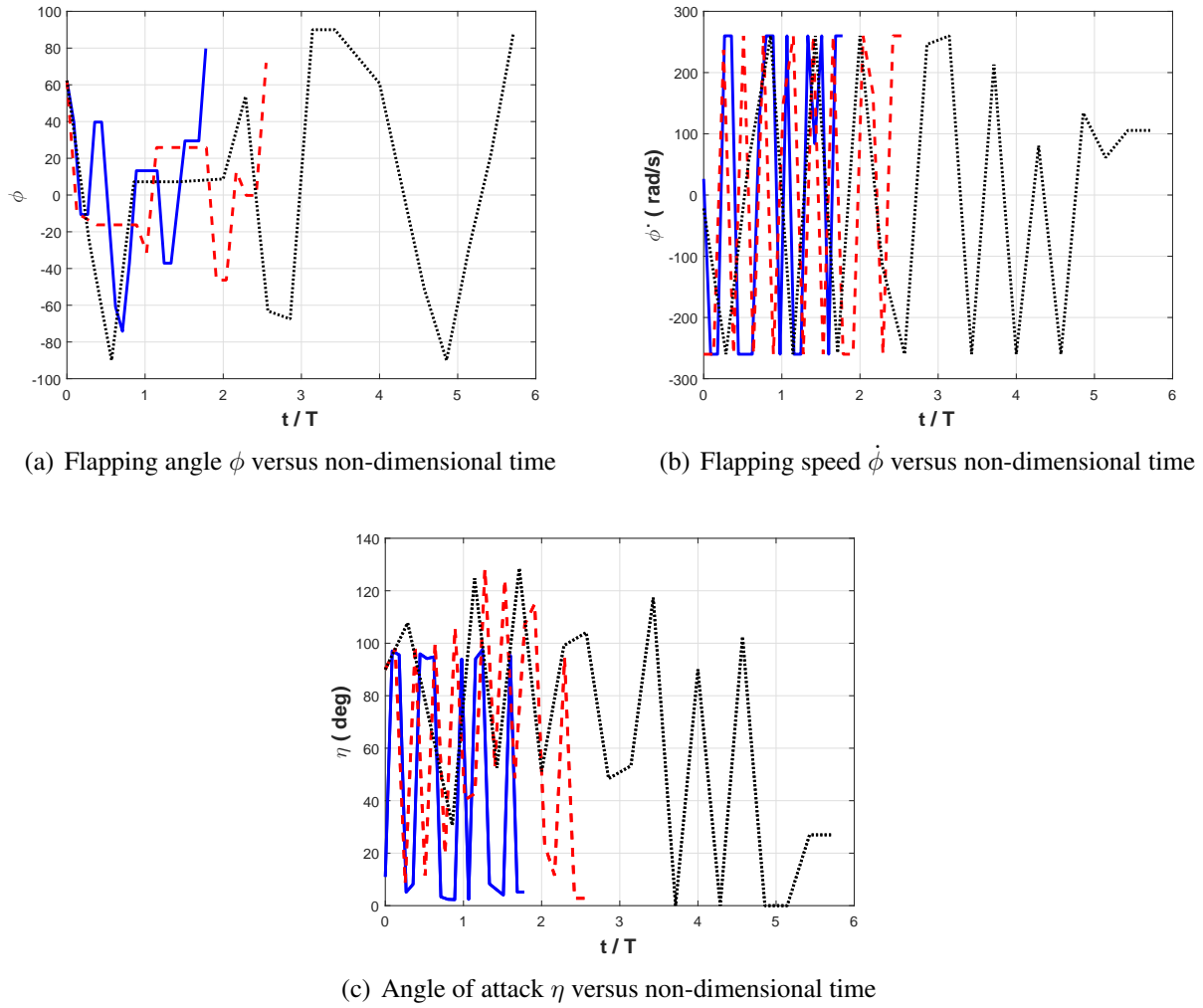
Figure 5.11: Time history of flapping angle, flapping speed , and angle of attack during transition from hovering to three different cases of forward flight using the time periodic dynamics in Eq.(5.4)

Figures 5.12, 5.13, 5.14 show the inertial velocities, the flapping angle and speed starting from the hovering cycle through the transition to the forward flight of average speed of $2m/s$, $3m/s$, and $4m/s$ respectively. The variation in the inertial velocity in X direction in Figure 5.12a, 5.13a, 5.14a shows a periodic oscillation around the nominal values in hover and forward flight, i.e. $0, 2, 3, 4m/s$, with ramp change in between. In addition, the variation in the flapping angle in φ direction in Figure 5.12c, 5.13c, 5.14c show a sinusoidal nature for the hovering and forward cycles with sawtooth nature in the transition phase. As noted from Figures 5.12c, 5.13c 5.14c ,the

continuity issue between the flapping cycles in transition is no longer noticed. However, the MAV needs to flap at much higher frequencies than in hover or forward flight. This can be seen from the time history of the flapping angles in Figures 5.12c, 5.13c, 5.14c. For the forward periodic orbits, a feedback controller is needed to stabilize the vehicle in case of any disturbance. This is not necessary in hovering as we noticed in Section 5.4.2 that different equilibrium orbits exist which some of them are stable as shown in Figure 5.6 and listed in Table 5.3.
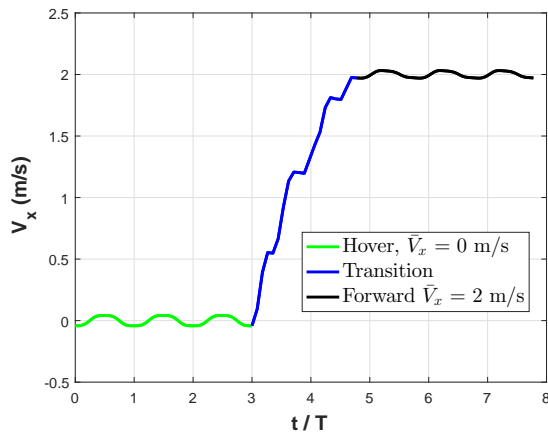
(a) Inertial velocity V_x versus non-dimensional time
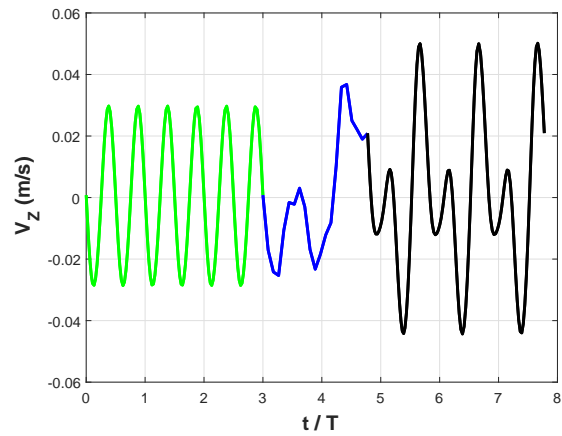
(b) Inertial velocity V_z versus non-dimensional time
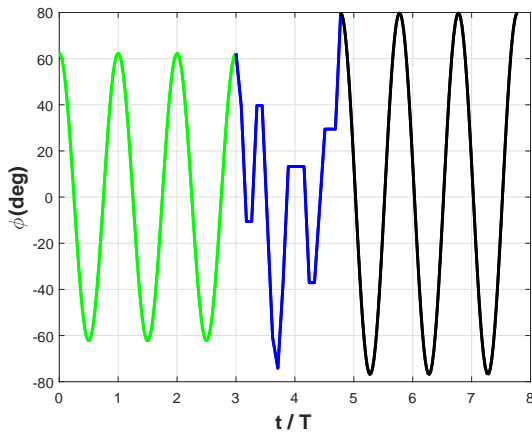
(c) Flapping angle ϕ versus non-dimensional time
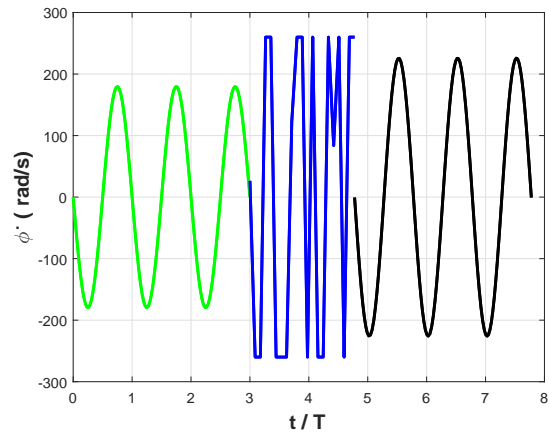
(d) Flapping speed $\dot{\phi}$ versus non-dimensional time

Figure 5.12: Time history of inertial velocities, flapping angles, and flapping velocities from hovering through transition to forward flight of $V_x = 2m/s$.
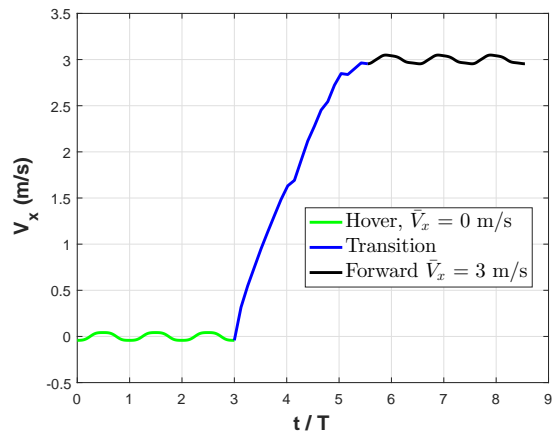
(a) Inertial velocity V_x versus non-dimensional time
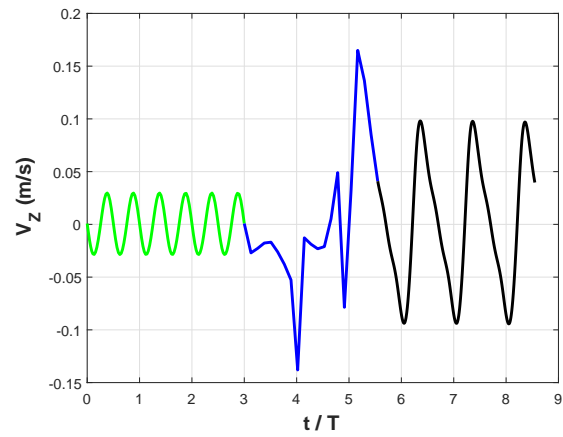
(b) Inertial velocity V_z versus non-dimensional time
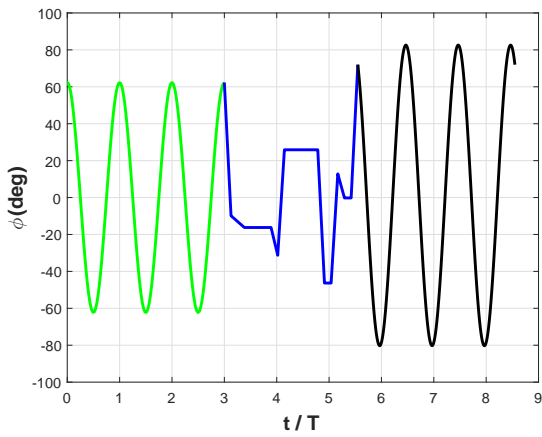
(c) Flapping angle ϕ versus non-dimensional time
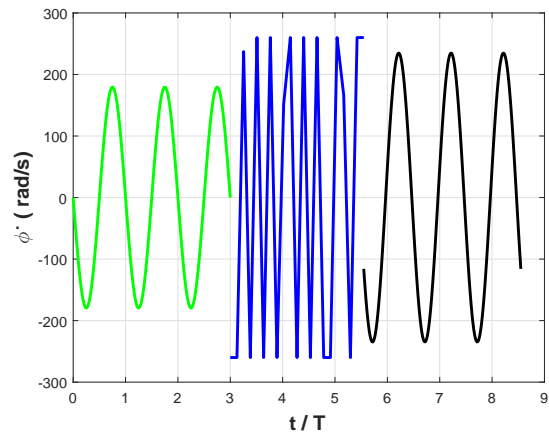
(d) Flapping speed $\dot{\phi}$ versus non-dimensional time

Figure 5.13: Time history of inertial velocities, flapping angles, and flapping velocities from hovering through transition to forward flight of $V_x = 3m/s$.
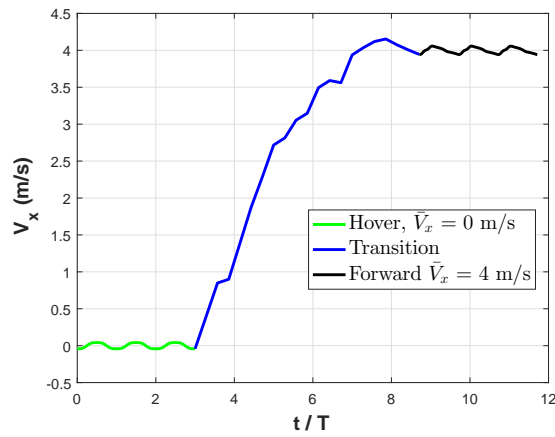
(a) Inertial velocity V_x versus non-dimensional time
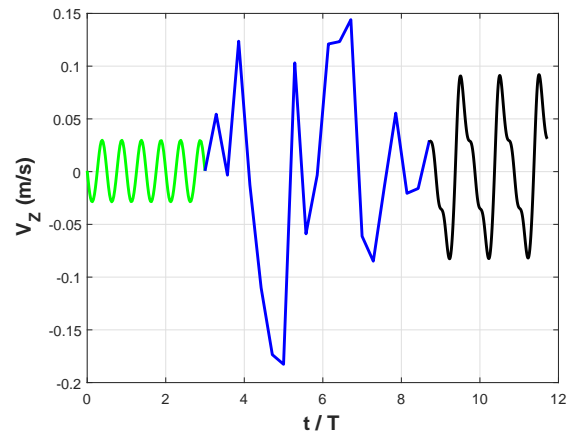
(b) Inertial velocity V_z versus non-dimensional time
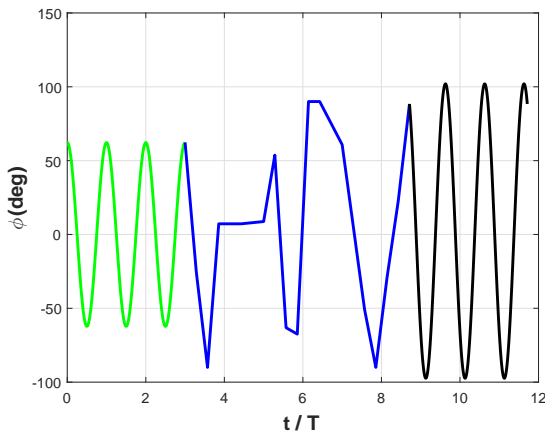
(c) Flapping angle ϕ versus non-dimensional time
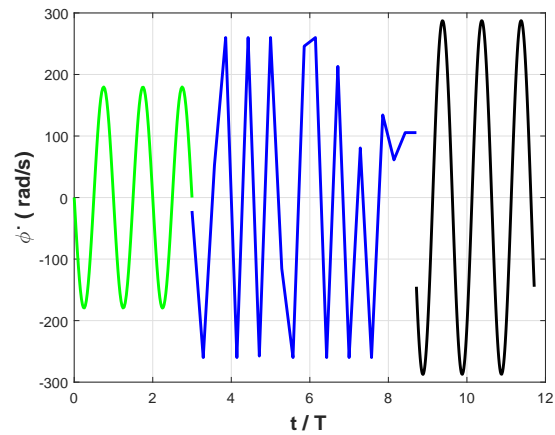
(d) Flapping speed $\dot{\phi}$ versus non-dimensional time

Figure 5.14: Time history of inertial velocities, flapping angles, and flapping velocities from hovering through transition to forward flight of $V_x = 4m/s$.

In Figure 5.15, the trajectory of the FWMAV from hovering through transition to forward flight, is shown for a three cases of the flight speeds. The hovering orbit is seen as point relative to the transition phase and forward one.The mechanism of gaining the thrust required to achieve the forward speed in highlighted in these Figures and the oscillation around the horizontal position is clearly seen at the end of the transition period.
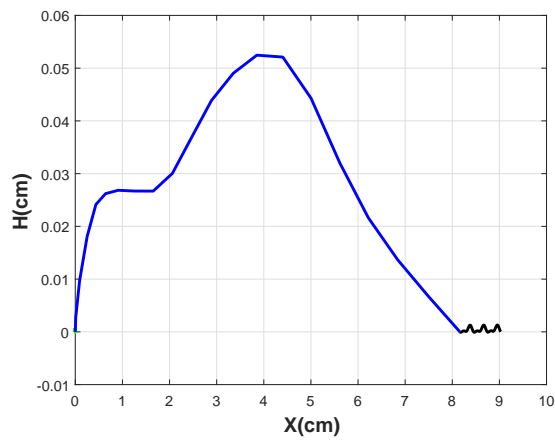
(a) Trajectory from hovering through transitioning to froward flight of $\bar{V}_x = 2m/s$
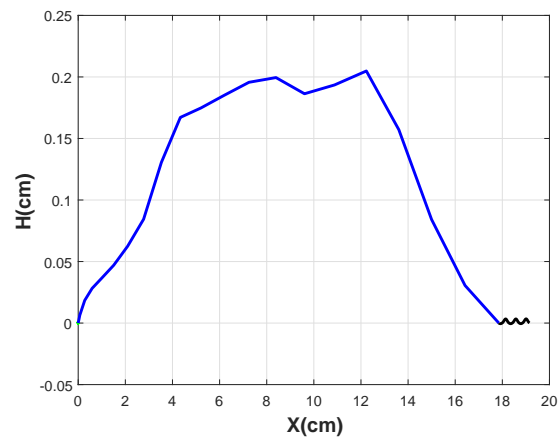
(b) Trajectory from hovering through transitioning to froward flight of $\bar{V}_x = 3m/s$
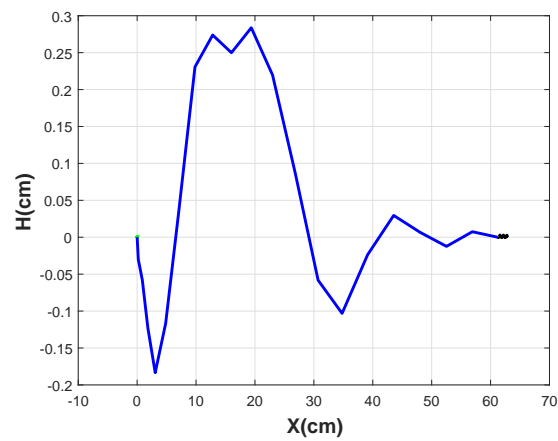
(c) Trajectory from hovering through transitioning to froward flight of $\bar{V}_x = 4m/s$

Figure 5.15: Trajectory from hovering through transitioning to froward flight for three different cases of forward flight.

(a) Flapping angle ϕ versus non-dimensional time

(b) Flapping speed $\dot\phi$ versus non-dimensional time
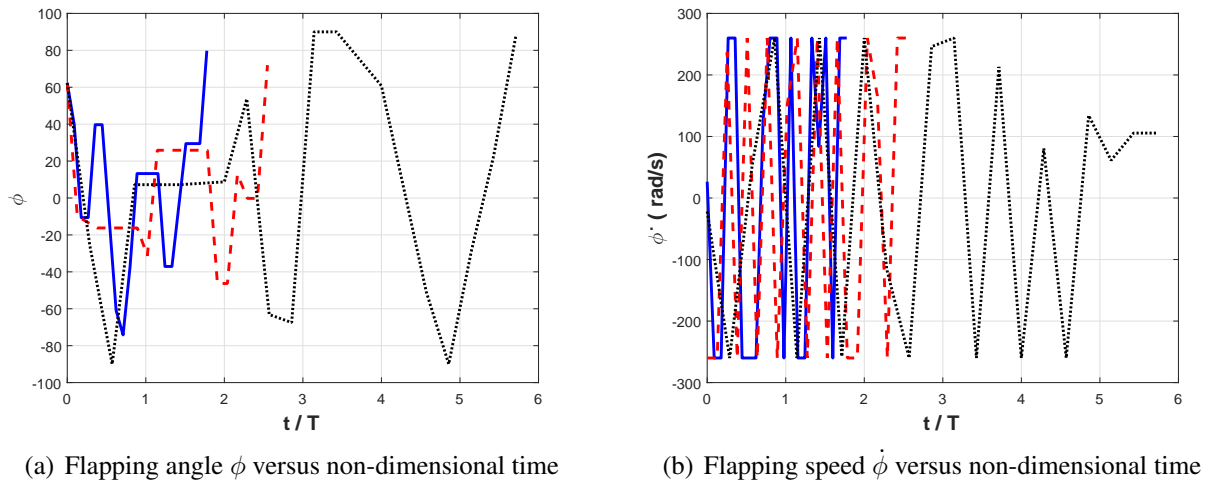
Figure 5.16: Time history of flapping angle and speed during transition from hovering to three different cases of forward flight using the time periodic dynamics in Eq.(5.4)

5.6   Conclusion

In this work, a simplified flight dynamic model for a flapping-wing micro-air-vehicle performing a horizontal stroke plane is considered. An optimal control problem is formulated to determine the evolution of the optimum waveform for the flapping angle in the horizontal plane that results in minimum-time transition from hovering to forward flight. We investigated the optimal control problem using time periodic and averaged dynamics. The averaging theorem is used to transform the nonlinear, time-periodic flapping flight dynamics into a time-invariant system. The flapping angle is the input to the averaged dynamics and is represented using a generic function, while the flapping speed and angle of attack of the wing are the inputs to the time periodic system. As such, the problem is formulated to determine the optimum evolution of the flapping angle that steers the averaged dynamics from a hovering equilibrium point to a forward flight equilibrium point, and the optimal evolution of the flapping speed and angel of attack that steers the time periodic dynamics from a hovering equilibrium orbit to a forward one. The results for the averaged dynamics can be summarized as follows:

1 - The simulation results of the time periodic system using the optimal flapping angle from the averaged dynamics optimization shows that the averaging is not suitable for designing the steering controller as the major dynamics is lost through averaging.

2- The discontinuity of the flapping angle during the transition maneuver makes it unreliable for practical implementation.

On the other hand, the transition results based on the time periodic dynamics shows that steering between the hovering and forward flight orbit is attainable. The results for the time periodic dynamics can be summarized as follows:

1- The time histories of the states for the forward flight periodic orbits showed that flight speeds between 0 and $4m/s$ lie in the attainable space.

2- The more the forward flight speed, the more time the MAV needs to perform the transition.

3- The more the forward flight speed, the more the FWMAV tends to choose the body pitching like helicopters to achieve the desired speed.

4- The flapping speed hits the upper and limit limits through the transition, i.e. Bang-Bang signal. This is expected due to the formulation of the optimal control problem as a minimum time transition.

5- The continuity of the flapping angle between the hovering through the transition to the forward flight shows that the time periodic dynamics is more suitable than the averaged dynamics for modeling the optimal control problem

Chapter 6

Stable, Planar Self Propulsion Using a Hinged Flap

6.1 Introduction

To swim, fish vary their shape to generate fluid dynamic forces needed for propulsion and control. Efforts to model these phenomena, whether to better understand biological locomotion or to engineer bioinspired devices, often rely on quasi-steady flow models that fail to capture the time-varying interactions between the body and the fluid. In this paper, we incorporate unsteady loads based on Theodorsen's well-known model for unsteady lift generation within a framework for the body motion to better understand the physics of pisciform ("fishlike") locomotion.

Biologists describe pisciform locomotion on a scale that ranges from "oscillatory" to "undulatory." At the "oscillatory" end of the spectrum, carangiform propulsion can be modeled by a three-body system in which a base body is propelled by a fin attached by a slender peduncle. A number of efforts have investigated the use of geometric control theory to construct gaits for engineered devices inspired by carangiform swimming [95–97].

At the "undulatory" end of the pisciform locomotion spectrum, [98] describes a number of aquatic

(and amphibious) snake robots developed to mimic the motion of eels. These include *HELIX* [99], *REEL I* and *II* [100], *ACM-R5* [101], and *Amphibots I, II,* and *III* [102]. Though she lists a variety of anguilliform robots, Kelasidi identifies only a few studies, beyond her own, that provide detailed locomotion analysis [100, 103, 104].

The focus of this paper is on the oscillatory end of the pisciform locomotion spectrum. In fact, we consider a case even simpler than that of carangiform propulsion: a simple two-body propulsion device comprising a forebody and a servo-actuated tail. The motion model for this four degree of freedom device accounts for unsteady flow effects using [13] well-known model.

The outline of this paper is as follows. In Section 6.2, we describe the kinematics and kinetics of the two-body propulsion body. In Section 6.3, we briefly discuss the theoretical work that provides the unsteady loads on an airfoil undergoing simple harmonic oscillations, and how we tailored those theories to apply them in the current model. The resulting equations of motion are nonlinear time periodic ordinanry differential equations. We use the optimized shooting method developed by [91] to find the periodic orbit. In Section 6.4, we assess the validity of the current model through investigating the stability of the saithe fish. In Section 6.5, we conclude by listing the capabilities of the current model and proposing planned future work.

6.2 Motion Model

6.2.1 Kinematic Relations

The forebody moves in the inertial X and Y directions with speed U and V, respectively, and it rotates around a vertical axis (parallel to the inertial Z axis) through the heading angle ψ. The tail is hinged at the end of the forebody and is forced to rotate about a vertical axis through angle θ relative to the body. The inertial velocity of the center of gravity of the forebody, as shown in Fig. 6.1, is given by

$$\vec{v}_B = U\vec{I} + V\vec{J} \tag{6.1}$$

where $\vec{I}$ and $\vec{J}$ are unit vectors in the inertial X and Y directions, respectively. The angular velocities of the body and tail are defined as

$$\vec{\omega}_B = \dot{\psi}\boldsymbol{K} \tag{6.2}$$

and

$$\vec{\omega}_t = (\dot{\psi} + \dot{\theta})\vec{K} = (\dot{\psi} + \dot{\theta})\boldsymbol{k}_t \tag{6.3}$$

where $\vec{K} = \vec{I} \times \vec{J}$ is aligned with the tail hinge defined by the unit vector $\boldsymbol{k}_t$.

6.2.2 Kinetic Relations

Using the representation of forces in Fig. 6.1, the equations of motion of the forebody are written as

$$
\begin{aligned}
m_B\dot{U} &= [T - N\sin(\psi) - N_\theta \sin(\psi + \theta) \\
&\quad - D_B \cos(\alpha_B)]\, S_{\text{Body}} \\
m_B\dot{V} &= [N\cos(\psi) + N_\theta \cos(\psi + \theta) \\
&\quad - D_B \sin(\alpha_B)]\, S_{\text{Body}} \\
I_B\dot{r} &= (M_\psi + M_\theta - N_\theta \frac{L_B}{2}\cos(\theta))S_{\text{Body}} \\
\dot{\psi} &= r
\end{aligned}
\tag{6.4}
$$

where N and N_θ are the unsteady normal forces generated by the body and tail, respectively, and M_ψ and M_θ are the unsteady moments generated by the body and tail. The forces T and D_B are the thrust and drag generated by the body and tail motion. The parameters m_B and I_B are the body mass and inertia and S_{Body} is the span of the fish body and tail out of the plane of motion. The details of these loads will be discussed in the next section.
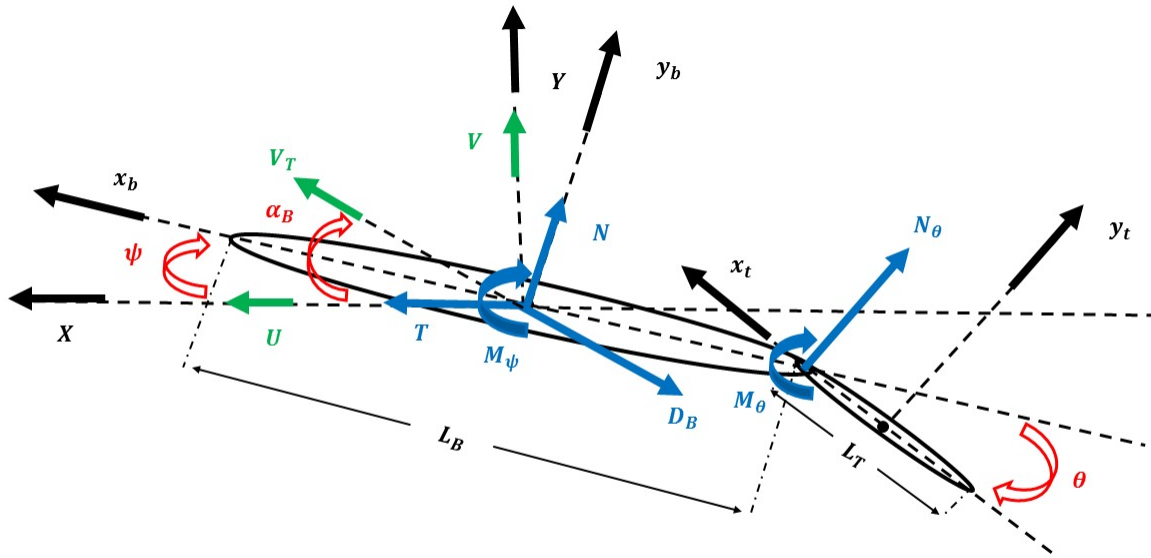
Figure 6.1: Annotated geometry of the two-body propulsion system. Velocity components are shown in green, angles are red, and forces and moments are blue.

6.3   Hydrodynamic Model

Analytical expressions were derived by [13] for the lift force and pitching moment for an airfoil undergoing simple harmonic pitching and plunging motion in a steady, free stream. Garrick [105] extended the model to an airfoil undergoing the same kinematics but with an oscillating, hinged flap. Garrick's goal was to investigate the effect of the unsteady kinematics on propulsive thrust and efficiency. Later, Greenberg [23] extended Theodorsen's work for an airfoil without a flap undergoing the same unsteady kinematic motion in a uniform free stream with time-varying velocity.
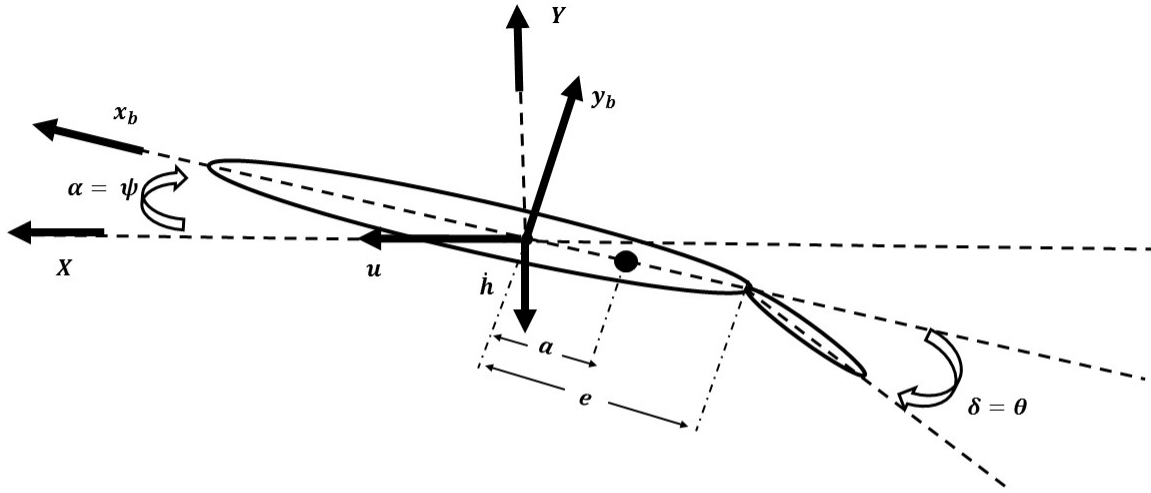
Figure 6.2: The given system is equivalent to an airfoil with flap in unsteady motion.

In this work, we adapt Greenberg's extension of Theodersen's work to Garrick's model. To use the expressions for the unsteady loads on a two-dimensional airfoil with a flap as defined by Garrick, we make the following assumptions. First, the two-body system is modeled as an airfoil with a flapping tail. Second, the flow around the body and tail is assumed to be two-dimensional. Finally, the mass and inertia of the tail are neglected, so that the center of mass of the two-body system is the center of mass of the forebody.

We let $u(t)$ denote the time-varying velocity of the free stream and we let $\delta(t)$ denote the flap deflection angle. Adopting the assumptions described above, and referring to Fig. 6.2, we give the following expressions for the normal forces N and N_θ, the thrust and suction forces T and S, and

the moments M_ψ and M_θ about a pivot point a and hinge e, respectively.

$$N = \rho b^2 \left[\pi(\ddot{h} + u\dot{\alpha} + \underline{\dot{u}\alpha} - ab\ddot{\alpha}) - T_4(u\dot{\delta} + \dot{u}\delta) - bT_1\ddot{\delta} \right]$$

$$N_\theta = \rho b^2 \left[T_4\ddot{h} + T_4(\underline{\dot{u}\alpha} + \dot{\alpha}u) - bT_9\ddot{\alpha} \right]$$
$$+ \frac{\rho b^2}{2\pi} \left[T_5(u\dot{\delta} + \underline{\dot{u}\delta}) + T_2b\ddot{\delta} \right]$$
$$+ \frac{\rho b}{\pi} u\sqrt{1-e^2} \left[\pi b(1-e)\dot{\alpha} + 2u\sqrt{1-e^2}\delta \right.$$
$$\left. + b(1-e)T_{10}\dot{\delta} \right] + 2\rho buT_{20}v_{3/4}C(k) \tag{6.5}$$

$$S = \frac{1}{\pi\sqrt{2}} [2v_{3/4c}C(k) - b\dot{\alpha} - 2\sqrt{1-e^2}u\delta + bT_4\dot{\delta}]$$

$$T = \pi\rho b^2 S^2 \tag{6.6}$$

$$M_\psi = \pi\rho b^3 \left[a\ddot{h} + (a - \frac{1}{2})u\dot{\alpha} + \underline{a\dot{u}\alpha} - b(a^2 + \frac{1}{8})\ddot{\alpha} \right]$$
$$- \rho b^2 \left[T_{15}u^2\delta + T_{16}b(u\dot{\delta} + \underline{\dot{u}\delta}) + 2T_{13}b^2\ddot{\delta} \right]$$
$$+ 2\pi\rho b^2 (a + \frac{1}{2})uv_{3/4}C(k)$$

$$M_\theta = \pi\rho b^3 \left[T_1\ddot{h} - T_{17}(u\dot{\alpha} + \underline{\dot{u}\alpha}) - 2T_{13}b\ddot{\alpha} \right]$$
$$+ \frac{\rho b^2}{\pi} \left[-T_{18}u^2\delta + \frac{T_{19}b}{2}(u\dot{\delta} + \dot{u}\delta) + T_3b^2\ddot{\delta} \right]$$
$$- \rho T_{12}b^2 uv_{3/4}C(k) \tag{6.7}$$

Underlined terms in these expressions arise due to time-variation of the free stream velocity. The parameter $C(k)$ is the deficiency function that accounts for periodic wake shedding at the trailing edge due to harmonic motion at reduced frequency k. The parameter b is the semi-chord of the combined body and tail (i.e., $b = (L_B + L_T)/2$). The parameters a and e denote the non-dimensional location of the pivot and hinge (i.e., measured in semi-chord lengths and positive aft

from the center of the body). The coefficients T_{1-20} are related to the hinge offset e and can be found in [105]. The normal velocity at the three-quarter chord line $v_{3/4}$ is given by

$$v_{3/4} = u\alpha + \dot{h} + b(\frac{1}{2} - a)\dot{\alpha} + \frac{T_{10}}{\pi}u\delta + \frac{bT_{11}}{2\pi}\dot{\delta} \tag{6.8}$$

The airfoil and flap variables are related to the body variables as follows:

$$\alpha = \psi \qquad u = U \qquad \dot{h} = -V \qquad \delta = \theta \tag{6.9}$$

Then $v_{3/4}$ is written in terms of body variables as

$$\begin{aligned}
v_{3/4c} &= U\psi - V + \frac{L_B + L_T}{2}(\frac{1}{2} - a)\dot{\alpha} \\
&+ \frac{T_{10}}{\pi}U\theta + \frac{(L_B + L_T)T_{11}}{4\pi}\dot{\delta}
\end{aligned} \tag{6.10}$$

Substituting the expressions in Eq. (6.9) into Eqs. (6.5), (6.6), and (6.7) yields

$$\begin{aligned}
N &= \rho b^2 \left[\pi(-\dot{V} + U\dot{\psi} + \dot{U}\psi - ab\ddot{\psi}) \right. \\
&\qquad \left. -T_4(U\dot{\theta} + \dot{U}\theta) - bT_1\ddot{\theta}\right] \\
N_\theta &= \rho b^2 \left[-T_4\dot{V} + T_4(\dot{U}\theta + \dot{\theta}U) - bT_9\ddot{\theta}\right] \\
&\quad + \frac{\rho b^2}{2\pi}\left[T_5(U\dot{\theta} + \dot{U}\theta) + T_2b\ddot{\theta}\right] \\
&\quad + \frac{\rho b}{\pi}U\sqrt{1-e^2}\left[\pi b(1-e)\dot{\psi} + 2U\sqrt{1-e^2}\theta \right. \\
&\qquad \left. + b(1-e)T_{10}\dot{\theta}\right] + 2\rho bUT_{20}v_{3/4}C(k)
\end{aligned} \tag{6.11}$$

$$\begin{aligned}
S &= \frac{1}{\pi\sqrt{2}}\left[2v_{3/4c}C(k) - b\dot{\psi} - 2\sqrt{1-e^2}U\theta + bT_4\dot{\theta}\right] \\
T &= \pi\rho b^2 S^2
\end{aligned} \tag{6.12}$$

$$M_\psi = \pi\rho b^3 \left[-a\dot{V} + (a - \frac{1}{2})U\dot{\psi} + a\dot{U}\psi - b(a^2 + \frac{1}{8})\ddot{\psi} \right]$$
$$- \rho b^2 \left[T_{15}U^2\theta + T_{16}b(U\dot{\theta} + \dot{U}\theta) + 2T_{13}b^2\ddot{\theta} \right]$$
$$+ 2\pi\rho b^2(a + \frac{1}{2})U v_{3/4}C(k)$$
$$M_\theta = \pi\rho b^3 \left[-T_1\dot{V} - T_{17}(U\dot{\psi} + \dot{U}\psi) - 2T_{13}b\ddot{\psi} \right]$$
$$+ \frac{\rho b^2}{\pi} \left[-T_{18}U^2\theta + \frac{T_{19}b}{2}(U\dot{\theta} + \dot{U}\theta) + T_3b^2\ddot{\theta} \right]$$
$$- \rho T_{12}b^2 U v_{3/4}C(k)$$

$$(6.13)$$

6.4   Results

To illustrate the model, we consider the geometry of a saithe, or pollock, and examine the body's propulsion and stability due to the flapping tail. The parameters of the geometry are presented in Table 6.1. The periodic solution in Fig. 6.3 is obtained using the shooting method discussed in [91] for a sinusoidal input of the form $\theta = a_o \sin(2\pi f t)$. A three-dimensional representation of this periodic orbit is shown in Figure 6.4.

Stability of the periodic orbit is assessed using Floquet theory. The multipliers of the state transition matrix associated with Eq. (6.4) are shown in Fig. 6.5 with respect to the unit circle. Their values are tabulated in Table 6.3. The maximum value of the multiplier lies inside the unit circle which implies that the system is stable. Figure 6.6 shows results from a simulation of Eq. (6.4) with zero initial state and with a tail flapping frequency and amplitude that correspond to a steady-state forward speed of $\bar{V}_x = 1.2$ m/s. To clarify the behavior of the system, the time simulation is also shown for time step of $\delta t = 50\Delta t$.

Table 6.1: Geometric Parameters

Parameter	Value
Body Length L_B	28 cm
Tail Length L_T	12 cm
Body Mass m_B	700 g
Pivot Point a	-0.75
Tail Hinge Point e	0.4

Table 6.2: Initial conditions for periodic orbit.

State	$\bar{V}_x = 1.2$ **m/s**
u (m/s)	1.2241
v (m/s)	-0.0345
r (rad/s)	0.3584
ψ (rad)	-0.0171
a_o (rad)	-0.1796
f (Hz)	4.2445
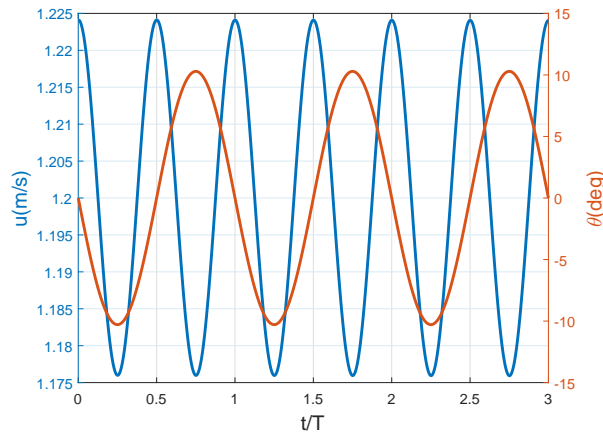
(a) Velocity U versus non-dimensional time
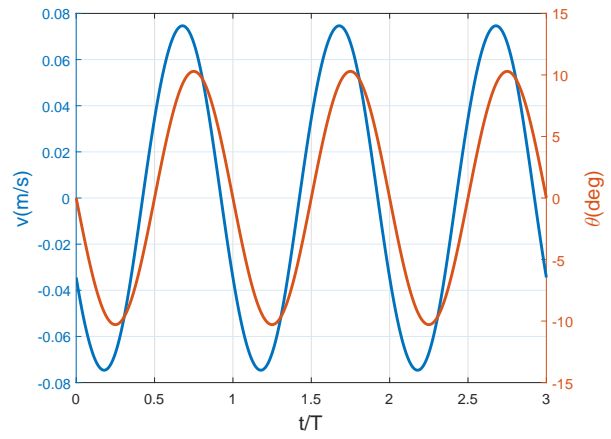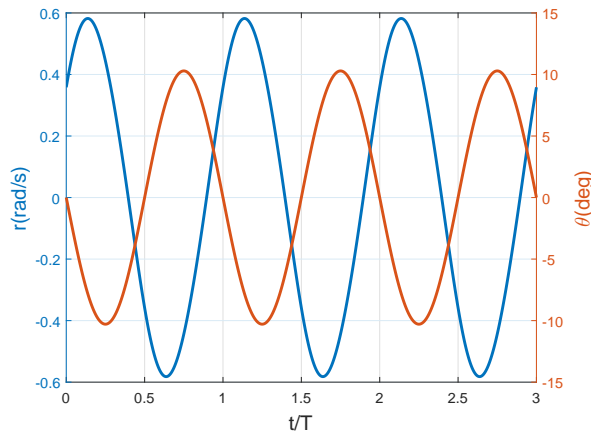
(b) Velocity W versus non-dimensional time

(c) Angular velocity r versus non-dimensional time
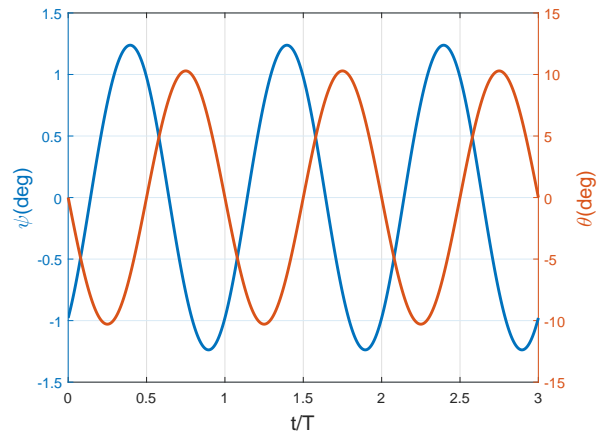
(d) Orientation ψ versus non-dimensional time

Figure 6.3: Time history of body variables for forward motion of $\bar{V}_x = 1.2$ m/s for three cycles.
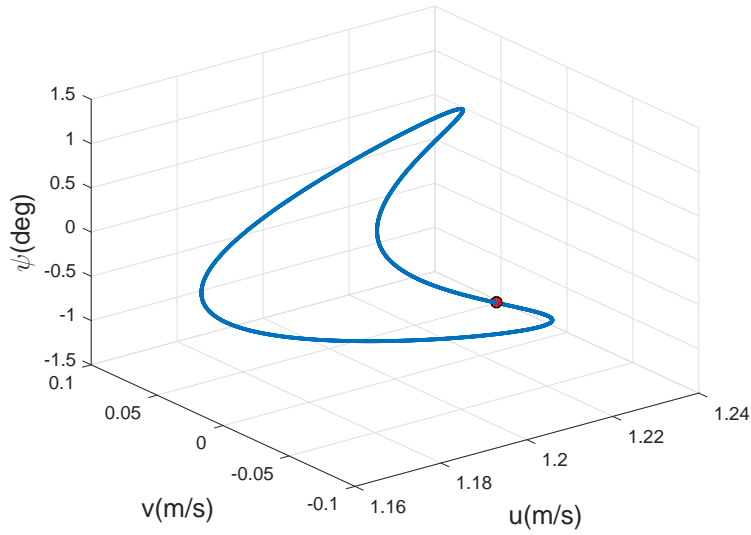
Figure 6.4: Periodic orbit for forward flight of $\bar{V}_x = 1.2 m/s$ in the three dimensional state space.

Table 6.3: Floquet multipliers z for a steady-state forward swimming of speed $\bar{V}_x = 1.2 m/s$ for the parameters in Table 6.1.

z
-0.0865 + 0.1252i
-0.0865 - 0.1252i
0.8296
0.9847
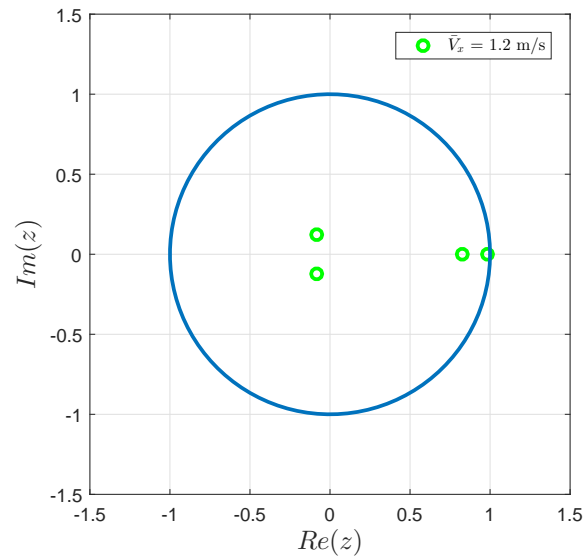
Figure 6.5: Floquet multipliers for the forward flight periodic orbit in the complex plane with respect to the unit circle for the parameters in Table 6.1.
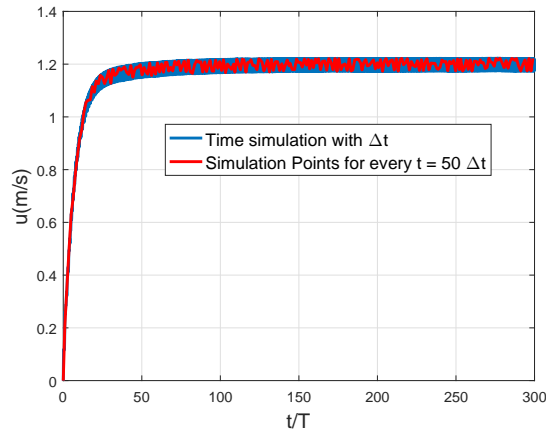
(a) Velocity U versus non-dimensional time
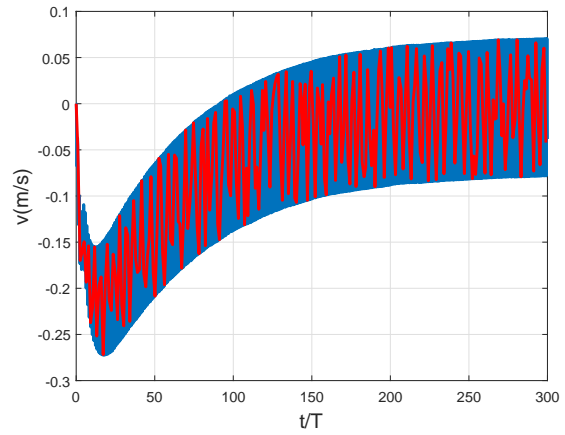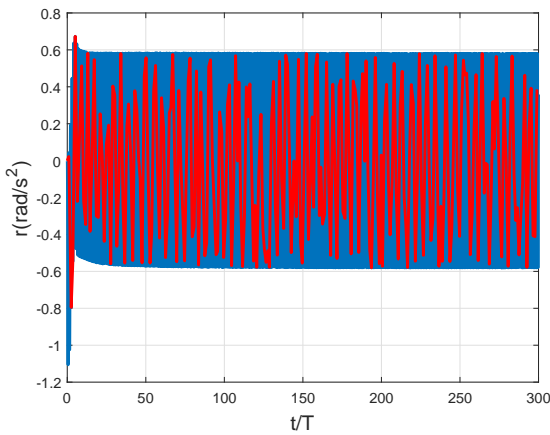
(b) Velocity W versus non-dimensional time

(c) Angular velocity r versus non-dimensional time
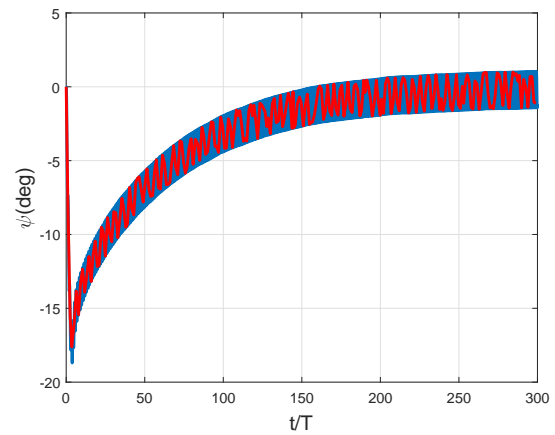
(d) Orientation ψ versus non-dimensional time

Figure 6.6: Simulation of equations of motion (6.4) using the input $\theta = -0.1796\sin(2\pi(4.2445)t)$.

To show the effect of the center of mass, the multipliers of the state transition matrix associated with Eq. (6.4) are shown in Fig. 6.7 with respect to the unit circle for the same parameters given in Table 6.1 but for $a = 0.75$, i.e. $a > 0$ implies that the center of mass lies behind the mid-point of the total length of the body and the tail. Their values are tabulated in Table 6.4. Unlike Fig. 6.5, the maximum value of the multipliers in Fig. 6.7 lies outside the unit circle which implies that the system is unstable.

Table 6.4: Floquet multipliers z for a steady-state forward swimming of speed $\bar{V}_x = 1.2 m/s$ for the parameters in Table 6.1 but for $a = 0.75$, i.e. $a > 0$.

z
1.2621 + 0.0000i
0.0396 + 0.0851i
0.0396 - 0.0851i
0.3653 + 0.0000i
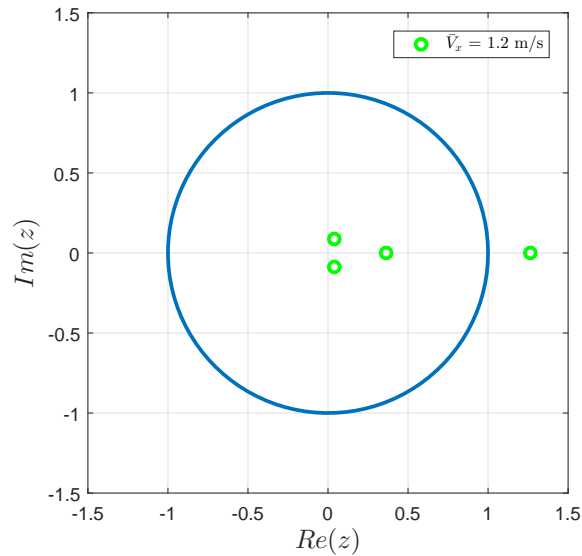
Figure 6.7: Floquet multipliers for the forward flight periodic orbit in the complex plane with respect to the unit circle for the parameters in Table 6.1 but for $a = 0.75$, i.e. $a > 0$.

6.5 Conclusion

We developed a coupled dynamic model for the motion of a simple two-body propulsion device comprising a forebody and a servo-actuated tail that is based on the geometry of the saithe or pollock. The unsteady loads were based on Theodorsen's unsteady lifting theory for sinusoidal flapping and were tailored for their application within the framework of the body motion. The

simulation results show variations of the body variables that are within the same range of measured values for a speed of $1.2 m/s$ in water. Stability analysis performed using Floquet thoery shows that the system is stable if the center of mass is ahead of the mid-point of the body and tail. If this is not the case, the system become unstable. Future research will be performed to expand the ranges of considered speeds and stability parameters in addition to conducting a few experiments using a prototype for the two-body system.

Chapter 7

Conclusions

7.1 Conclusions

We implemented different dynamical system representations of unsteady flow and fluid-structure interaction systems with the objective of either developing a reduced-order formulation or assessing their performance or stability. In Chapter 2, we investigated the potential of implementing variational principles to derive governing equations for the interaction of unsteady point vortices with a solid boundary. To do so, we postulated a new Lagrangian function for the dynamics of point vortices that is more general than Chapmans. We showed that this function is related to Chapmans Lagrangian via a gauge symmetry for the case of constant-strength vortices. In other words, both Lagrangian functions result in the same steady governing equation, i.e. the Biot-Savart law is directly recovered from the Euler-Lagrangeequations corresponding to minimization of the action integral with these two Lagrangians. We also found that, unlike Chapmans Lagrangian, the principle of least action based on the proposed Lagrangian results exactly in the Brown-Michael model for the dynamics of unsteady point vortices. We implemented the resulting dynamic model of time-varying vortices to the problem of an impulsively started flat plate as well as an accelerating and pitching flat plate. For the case of an accelerating flat plate, the resulting time history of the lift coefficient from the three models (variational based approach for the proposed Lagrangian

and Chapmans, and the impulse matching model) was compared against the experimental results of Beckwith and Babinsky. The results showed a better agreement for the variation approach using the proposed Lagrangian. On the other hand, the results of the impulse matching model for the pitching flat plat agree better with experimental results than the those based on Chapmanns and the proposed Lagrangian (Brown-Michael model).

In Chapter 3, we used different Padé approximations for Loewys deficiency function to investigate the dynamic stability of a hovering rotor blade. After linearizing the equations of motion about the nonlinear trim deflections, the flutter boundary was found in time domain by approximating the lift deficiency function as a rational polynomial in terms of Laplace operator. This formulation yielded a new stability region that could not be determined under the assumption of a quasi-steady flow.

In Chapter 4, we solved for the hydrodynamic loads generated by the motion of a flapping fish tail. We modeled the cases of rigid, passive and actively actuated flexible tails using the two-dimensional unsteady vortex lattice method. The results showed that the passive flexible case introduce some enhancement in the propulsive efficiency. However, these improvements were not observed in the case of the actively flexible tails. To overcome this inconsistency, we used the three-dimensional UVLM to accurately model the hydrodynamics chordwise load distribution. The results showed that flexibility enhances the performance of flapping tails.

In Chapter 5, we formulated the evolution of the optimum waveform for the flapping angle in the horizontal plane that would result in minimum-time transition from hovering to forward flight. We investigated the optimal control problem using time periodic and averaged dynamics. The averaging theorem was used to transform the nonlinear, time-periodic flapping flight dynamics into a time-invariant system. The flapping angle was used as the input to the averaged dynamics and was represented using a generic function, while the flapping speed was used as the input to the time periodic system. As such, the problem was formulated to determine the optimum evolution of the flapping angle that steers the averaged dynamics from a hovering equilibrium point to a forward flight equilibrium point, and the optimal evolution of the flapping speed that steers the

time periodic dynamics from a hovering equilibrium orbit to a forward one. The results showed that averaged-dynamics optimization is not suitable for designing the steering controller as the major dynamics is lost through averaging and the resulting discontinuity of the flapping angle during the transition maneuver makes it unreliable for practical implementation. On the other hand, the transition results based on the time periodic dynamics shows that steering between the hovering and forward flight orbit is attainable.

In Chapter 6, we developed a coupled dynamical model for the motion of a simple two-body propulsion device comprising a forebody and a servo-actuated tail that is based on the geometry of the saithe or pollock. The unsteady loads were based on Theodorsens unsteady lifting theory for sinusoidal flapping and were tailored for their application within the framework of the body motion. The simulation results show variations of the body variables that are within the same range of measured values for a speed of $1.2m/s$ in water. Stability analysis performed using Floquet theory showed that the system is stable if the center of mass is ahead of the mid-point of the body and tail and unstable if the center of mass is behind this mid-point.

Results presented in this dissertation provide a basis for expanded use of different approaches based on dynamical system approaches for reduced-order modeling of unsteady flows and fluid structure interaction problems.

Appendix A

Finite Element Model and Finite-State Unsteady Aerodynamics

A.1 Mass Damping and Stiffness Matrices of the Aeroelastic Model

Mass Matrix :

$$M = \mathbf{E}_I + \mathbf{A}_I$$

Where $\mathbf{E}_I$ and $\mathbf{A}_I$ are the mass matrices of inertia and aerodynamic loadings respectively.

Damping Matrix :

$$\mathbf{D}_1 = -\mathbf{A}_{d_1}$$

$$\mathbf{D}_2 = -\mathbf{A}_{d_2} + \mathbf{E}_D + \mathbf{C}_T$$

Where $\mathbf{A}_{d_1}$ and $\mathbf{A}_{d_2}$, $\mathbf{E}_D$ and $\mathbf{C}_T$ are the damping matrices of aerodynamic, inertia and structure loadings restrictively.

Stiffness Matrix :

$$\mathbf{K} = \mathbf{E}_S + \mathbf{K}_{LT} - \frac{\partial\{\boldsymbol{K}_{NL}.\mathbf{q}\}}{\partial\mathbf{q}}$$

$$\mathbf{K}_S = -\mathbf{A}_S - \frac{\partial\{\mathbf{A}_{S_{NL}}.\mathbf{q}\}}{\partial\mathbf{q}}$$

$$\mathbf{K}_{LT} = \mathbf{K}_L + \mathbf{T}$$

Where $\mathbf{A}_S$ and $\mathbf{A}_{\mathbf{S}_{NL}}$, $\mathbf{E}_S$, $\mathbf{K}_{LT}$($\mathbf{K}_L$ and $\mathbf{T}$) and $\mathbf{K}_{NL}$ are the stiffness matrices of aerodynamic, inertia and structure loadings restrictively.

Free Vector :

$$\mathbf{F} = \mathbf{A}_F - \mathbf{E}_F$$

Where $\mathbf{A}_F$ and $\mathbf{E}_F$ are the free vectors of aerodynamic and inertia loadings respectively.

$$
\begin{aligned}
\mathbf{K}_{NL}\mathbf{q} = &-(\Lambda_z - \Lambda_y)sin(2\theta_c)\int_0^L (\mathbf{N}_v'')^T\mathbf{N}_\phi\mathbf{q}\mathbf{N}_v''\mathbf{q}dx - (\Lambda_z - \Lambda_y)cos(2\theta_c)\int_0^L (\mathbf{N}_v'')^T\mathbf{N}_\phi\mathbf{q}\mathbf{N}_w''\mathbf{q}dx \\
&+ (\Lambda_z - \Lambda_y)cos(2\theta_c)\int_0^L (\mathbf{N}_w'')^T\mathbf{N}_\phi\mathbf{q}\mathbf{N}_v''\mathbf{q}dx + (\Lambda_z - \Lambda_y)sin(2\theta_c)\int_0^L (\mathbf{N}_w'')^T\mathbf{N}_\phi^T\mathbf{q}\ \mathbf{N}_w''\mathbf{q}dx \\
&+ (\Lambda_z - \Lambda_y)\frac{sin(2\theta_c)}{2}\int_0^L (\mathbf{N}_w''\mathbf{q}\mathbf{N}_w'' - \mathbf{N}_v''\mathbf{q}\mathbf{N}_v'')\,\mathbf{q}dx \\
&+ (\Lambda_z - \Lambda_y)cos(2\theta_c)\int_0^L \mathbf{N}_v''\mathbf{q}\mathbf{N}_w''\mathbf{q}dx
\end{aligned}
$$

$$\text{(A.1)}$$

$$
\begin{aligned}
\mathbf{K}_L = &(\Lambda_z cos^2\theta_c + \Lambda_y sin^2\theta_c)\int_0^L (\mathbf{N}_v'')^T\mathbf{N}_v''dx + (\Lambda_z - \Lambda_y)\frac{sin(2\theta_c)}{2}\int_0^L (\mathbf{N}_v'')^T\mathbf{N}_w''dx \\
&+ (\Lambda_z - \Lambda_y)\frac{sin(2\theta_c)}{2}\int_0^L (\mathbf{N}_w'')^T\mathbf{N}_v''dx + (\Lambda_z cos^2\theta_c + \Lambda_y sin^2\theta_c)\int_0^L (\mathbf{N}_w'')^T\mathbf{N}_w''dx \quad \text{(A.2)} \\
&+ \kappa \int_0^L (\mathbf{N}_\phi')^T\mathbf{N}_\phi'dx
\end{aligned}
$$

$$F_A = R^2 \int_{\bar{X}}^1 (\bar{X} + 2\dot{v})d\bar{X} = \frac{R^2}{2}\left(1 - \bar{X}^2\right) + R^2 \int_{\bar{X}}^1 (2\dot{v})d\bar{X} \qquad \text{(A.3)}$$

$$\mathbf{T} = \int_0^L F_A \left((\mathbf{N}_w')^T \mathbf{N}_w' + (\mathbf{N}_v')^T \mathbf{N}_v' + (\mathbf{N}_\phi')^T \mathbf{N}_\phi' \right) dx$$

$$= \int_0^L \frac{1}{2} \left(1 - (\bar{X}_i + x)^2 \right) (\mathbf{N}_w')^T \mathbf{N}_w' dx$$

$$+ \int_0^L \frac{1}{2} \left(1 - (\bar{X}_i + x)^2 \right) (\mathbf{N}_v')^T \mathbf{N}_v' dx \tag{A.4}$$

$$+ \int_0^L \frac{1}{2} \frac{k_A^2}{R^2} \left(1 - (\bar{X}_i + x)^2 \right) (\mathbf{N}_\phi')^T \mathbf{N}_\phi' dx$$

$$\mathbf{C}_T = \int_0^L F_A \left((\mathbf{N}_w')^T \mathbf{N}_w' + (\mathbf{N}_v')^T \mathbf{N}_v' + (\mathbf{N}_\phi')^T \mathbf{N}_\phi' \right) dx$$

$$= \int_0^L \left(\int_{\bar{X}}^1 (2\dot{\bar{v}}) d\bar{X} \right) (\mathbf{N}_w')^T \mathbf{N}_w' dx \tag{A.5}$$

$$+ \int_0^L \left(\int_{\bar{X}}^1 (2\dot{\bar{v}}) d\bar{X} \right) (\mathbf{N}_v')^T \mathbf{N}_v' dx$$

$$\mathbf{E}_I = \int_0^L (\mathbf{N}_v')^T \mathbf{N}_v dx + \int_0^L (\mathbf{N}_w')^T \mathbf{N}_w dx + \mu^2 \int_0^L (\mathbf{N}_\phi')^T \mathbf{N}_\phi dx \tag{A.6}$$

$$\mathbf{E}_D = -2\beta_{pc} \int_0^L (\mathbf{N}_v')^T \mathbf{N}_w dx + 2\beta_{pc} \int_0^L (\mathbf{N}_w')^T \mathbf{N}_v dx - 2 \int_0^L (\mathbf{N}_v')^T (\mathbf{N}_v \mathbf{q} \mathbf{N}_v + \mathbf{N}_w \mathbf{q} \mathbf{N}_w) dx \tag{A.7}$$

$$\mathbf{E}_S = -\int_0^L (\mathbf{N}_v')^T \mathbf{N}_v dx + (\mu_z^2 - \mu_y^2) cos2\theta \int_0^L (\mathbf{N}_\phi')^T \mathbf{N}_\phi dx \tag{A.8}$$

$$\mathbf{E}_F = -\beta_{pc} \int_0^L (\mathbf{N}_w')^T \bar{X} dx - (\mu_z^2 - \mu_y^2) \frac{sin2\theta_c}{2} \int_0^L (\mathbf{N}_\phi')^T \mathbf{N}_\phi dx \tag{A.9}$$

$$\mathbf{A}_I = \frac{-\gamma \bar{c}}{24} \int_0^L (\mathbf{N}_w')^T \mathbf{N}_w dx - \frac{\gamma \bar{c}^3}{96} \left(\frac{1}{8} + a^2 \right) \int_0^L (\mathbf{N}_\phi')^T \mathbf{N}_\phi dx \tag{A.10}$$

$$
\begin{aligned}
\mathbf{A}_{d_1} = &\; \frac{-\gamma\lambda_i}{6}\int_0^L (\mathbf{N}_v)^T(\mathbf{N}_\phi q + \theta_c)\mathbf{N}_v dx + \frac{\gamma}{6}\int_0^L (\mathbf{N}_v')^T(2\lambda_i - (x + \bar{X}_i)(\mathbf{N}_\phi q + \theta_c))\mathbf{N}_v dx \\
&- \frac{\gamma}{6}\int_0^L (x + \bar{X}_i)(\mathbf{N}_w)^T\mathbf{N}_w dx + \frac{\gamma}{6}\int_0^L (\mathbf{N}_w)^T(2(x + \bar{X}_i)(\mathbf{N}_\phi q + \theta_c) - \lambda_i)\mathbf{N}_v dx \\
&+ \frac{\gamma\bar{c}}{12}(\frac{1}{2} - a)\int_0^L (\mathbf{N}_w)^T(x + \bar{X}_i)\mathbf{N}_\phi dx + \frac{\gamma\bar{c}^2}{24}(\frac{1}{2} + a)(\frac{1}{2} - a)\int_0^L (\mathbf{N}_\phi)^T(x + \bar{X}_i)\mathbf{N}_\phi dx \\
&+ \frac{\gamma\bar{c}}{6}(\frac{1}{2} + a)\int_0^L (N_\phi)^T(x + \bar{X}_i)(N_\phi q + \theta_c)N_v dx - \frac{\gamma\bar{c}}{12}(\frac{1}{2} + a)\int_0^L (N_\phi)^T(x + \bar{X}_i)N_w dx \\
&- \frac{\gamma\bar{c}\lambda_i}{12}(\frac{1}{2} + a)\int_0^L (\mathbf{N}_\phi)^T\mathbf{N}_v dx
\end{aligned}
$$

$$(A.11)$$

$$
\begin{aligned}
\mathbf{A}_S = &\; -\frac{\gamma}{6}\int_0^L (x + \bar{X}_i)(\mathbf{N}_v)^T\mathbf{N}_\phi dx + \frac{\gamma}{6}\int_0^L (x + \bar{X}_i)^2(\mathbf{N}_w)^T\mathbf{N}_\phi dx \\
&- \frac{\gamma\beta_{pc}}{6}\int_0^L (x + \bar{X}_i)(\mathbf{N}_w)^T\mathbf{N}_v dx + \frac{\gamma\bar{c}}{12}(\frac{1}{2} - a)\int_0^L (x + \bar{X}_i)(\mathbf{N}_w)^T\mathbf{N}_w dx \\
&+ \frac{\gamma\bar{c}}{12}(\frac{1}{2} + a)\int_0^L (x + \bar{X}_i)^2(\mathbf{N}_\phi)^T\mathbf{N}_\phi dx - \frac{\gamma\bar{c}\beta_{pc}}{12}(\frac{1}{2} + a)\int_0^L (x + \bar{X}_i)^2(\mathbf{N}_\phi)^T\mathbf{N}_v dx \\
&+ \int_0^L \left(\frac{\gamma\bar{c}^2\beta_{pc}}{24}(\frac{1}{2} + a)(\frac{1}{2} - a)(x + \bar{X}_i) - \frac{\gamma\bar{c}^2}{96}(x + \bar{X}_i) \right)(\mathbf{N}_\phi)^T\mathbf{N}_w dx
\end{aligned}
$$

$$(A.12)$$

$$
\mathbf{A}_{S_{NL}} = -\frac{\gamma}{6}\int_0^L \left((\mathbf{N}_v)^T(x + \bar{X}_i)^2 \left(\int_0^{x + \bar{X}_i} (\mathbf{N}_v)''(\mathbf{N}_w)' dX \right) \right) dx \qquad (A.13)
$$

$$\mathbf{A}_F = \int_0^L \mathbf{N}_v^T \frac{\gamma}{6} \left(-\frac{C_{D_o} \left(\bar{X}_i + x \right)^2}{a_o} - \theta_c \lambda_i \left(\bar{X}_i + x \right) + \lambda_i^2 \right)$$

$$+ \int_0^L \mathbf{N}_w^T \frac{\gamma}{6} \left(\frac{1}{2} \left(\frac{1}{2} - a \right) \bar{c} \beta_{pc} \left(\bar{X}_i + x \right) - \lambda_i \left(\bar{X}_i + x \right) + \theta_c \left(\bar{X}_i + x \right)^2 \right)$$

$$+ \int_0^L \mathbf{N}_\phi^T \frac{1}{12} \left(a + \frac{1}{2} \right) \gamma \bar{c} \left(\frac{1}{2} \left(\frac{1}{2} - a \right) \bar{c} \beta_{pc} \left(\bar{X}_i + x \right) - \lambda_i \left(\bar{X}_i + x \right) + \theta_c \left(\bar{X}_i + x \right)^2 \right)$$

$$- \frac{1}{96} \gamma \bar{c}^2 \beta_{pc} \left(\bar{X}_i + x \right)$$

$$(A.14)$$

The shape functions $\mathbf{N}_w$, $\mathbf{N}_v$ and $\mathbf{N}_\phi$ are defined in Ref. [57]. Also the section integrals Λ_z, Λ_y, κ, k_A^2, μ_z^2 and μ_y^2 can be found in Ref. [53].

A.2   State Space Representation of the Equations of Motion

The following procedure aims to familiarize the reader of how the equations of motion can be written in state space form, if we can represent the deficiency function $C(k)$ as a fractional polynomial $\frac{N(p)}{D(p)}$ in Laplace operator p .

Recalling (3.20)

$$\dot{y} = Ay + By \frac{N(p)}{D(p)} \tag{A.15}$$

Let $L_C = y \frac{N(p)}{D(p)}$,   where $L_1 = y_1 \frac{N(p)}{D(p)}, ...L_{Ny} = y_{Ny} \frac{N(p)}{D(p)}$ and N_y is the length of y.

Introducing intermediate variable h such that :

$$\frac{L_1}{h} \frac{h}{y_1} = \frac{N(p)}{D(p)} \tag{A.16}$$

Let $\frac{L_1}{h} = N(p)$ and $\frac{h}{y_1} = \frac{1}{D(p)}$, expanding N and D in terms of p leads to :

$$y_1 = h[p^n + d_{n-1}p^{n-1} + ...d_0] \tag{A.17}$$

$$L_1 = h[a_m p^m + a_{m-1}p^{m-1} + ...a_0] \tag{A.18}$$

Equation (A.17) can be written in state space form as :

$$
\begin{bmatrix} \frac{d^n h}{dt^n} \\ \frac{d^{n-1}h}{dt^{n-1}} \\ . \\ . \\ . \\ \frac{dh}{dt} \end{bmatrix} = \begin{bmatrix} -d_{n-1} & -d_{n-2} & ..... & d_0 \\ 1 & 0 & ..... & 0 \\ 0 & 1 & ..... & 0 \\ . & . & 1 & 0 \\ . & . & . & 0 \\ . & . & . & 0 \end{bmatrix} \begin{bmatrix} \frac{d^{n-1}h}{dt^{n-1}} \\ \frac{d^{n-2}h}{dt^{n-2}} \\ . \\ . \\ . \\ h \end{bmatrix} + \begin{bmatrix} 1 \\ 0 \\ . \\ . \\ . \\ 0 \end{bmatrix} y_1 \tag{A.19}
$$

In matrix form :

$$\dot{H} = A_c H + B_c y_1 \tag{A.20}$$

From eq A.17 : $\frac{d^n h}{dt^n} = y_1 - d_{n-1}\frac{d^{n-1}h}{dt^{n-1}} - d_{n-2}\frac{d^{n-2}h}{dt^{n-2}}........ - d_0 h$

for the case of $n = m$ (it's always the case), substitute in (A.18)

$$L_1 = \begin{bmatrix} (a_{m-1} - a_m d_{n-1}) & (a_{m-2} - a_m d_{n-2}) & ...... & (a_0 - a_m d_0) \end{bmatrix} \begin{bmatrix} \frac{d^{n-1}h}{dt^{n-1}} \\ \frac{d^{n-2}h}{dt^{n-2}} \\ . \\ . \\ . \\ h \end{bmatrix} + [a_m]y_1 \tag{A.21}$$

In matrix form :

$$L_1 = C_c H + D_c y_1 \tag{A.22}$$

(A.22) and (A.20) is repeated N_y times such that :

$$
\begin{bmatrix} \dot{H} \\ . \\ . \\ \dot{H} \end{bmatrix} =
\begin{bmatrix} A_c & [0] & ... & [0] \\ [0] & A_c & ... & [0] \\ . & .. & .. & [0] \\ [0] & .. & .. & A_c \end{bmatrix}
\begin{bmatrix} H \\ . \\ . \\ H \end{bmatrix} +
\begin{bmatrix} B_c & [0] & ... & [0] \\ [0] & B_c & ... & [0] \\ . & .. & .. & [0] \\ [0] & .. & .. & B_c \end{bmatrix}
\begin{bmatrix} y_1 \\ y_2 \\ . \\ y_{N_y} \end{bmatrix} \tag{A.23}
$$

$$
\begin{bmatrix} L_1 \\ . \\ . \\ L_{N_y} \end{bmatrix} =
\begin{bmatrix} C_c & [0] & ... & [0] \\ [0] & C_c & ... & [0] \\ . & .. & .. & [0] \\ [0] & .. & .. & C_c \end{bmatrix}
\begin{bmatrix} H \\ . \\ . \\ H \end{bmatrix} +
\begin{bmatrix} D_c & [0] & ... & [0] \\ [0] & D_c & ... & [0] \\ . & .. & .. & [0] \\ [0] & .. & .. & D_c \end{bmatrix}
\begin{bmatrix} y_1 \\ y_2 \\ . \\ y_{N_y} \end{bmatrix} \tag{A.24}
$$

In matrix form :

$$\dot{M} = A_C M + B_C y \tag{A.25}$$

$$L_C = C_C M + D_C y \tag{A.26}$$

Combining (A.2) and (A.26) with (A.15) leads to :

$$
\begin{bmatrix} \dot{y} \\ \dot{M} \end{bmatrix} =
\begin{bmatrix} A + B.D_C & B.C_C \\ B_C & A_C \end{bmatrix}
\begin{bmatrix} y \\ M \end{bmatrix} \tag{A.27}
$$

Introducing a new variable $Z = \begin{bmatrix} y \\ M \end{bmatrix}$, eq (A.27) can be written as :

$$\therefore \dot{Z} = A_{new} Z \tag{A.28}$$

Where :

$$A_{new} = \begin{bmatrix} A + B.D_C & B.C_C \\ B_C & A_C \end{bmatrix}$$

(A.29)

Appendix B

System Equilibrium Representations

B.1 Averaged Dynamics

Equation (5.4) is a nonlinear time-periodic (NLTP) system whose stability analysis and control design are quite challenging. A very convenient way of transforming the NLTP system in Eq. (5.1) to a representative time-invariant system is the averaging approach. This approach is mainly based on the assumption that, due to the very fast flapping frequency relative to the body dynamics, the body only feels the average values of the aerodynamic loads. It should be noted that the ratio of the flapping frequency to the body natural frequency for the one of the slowest flapping insects (Hawkmoth) is about 30 [90]. For a man made FWMAVs (e.g., Harvard Robofly), this ratio may be as high as 120. In fact, the averaging approach is mathematically justified through the following theorem.

For a nonlinear, time-periodic system in the form

$$\dot{\boldsymbol{\chi}} = \epsilon \boldsymbol{Y}(\chi, t, \epsilon) \tag{B.1}$$

where $\boldsymbol{Y}$ is T-periodic and ϵ is small enough, the averaged dynamics are defined by [106]

$$\dot{\bar{\boldsymbol{\chi}}} = \epsilon \bar{\boldsymbol{Y}}(\bar{\boldsymbol{\chi}}) = \epsilon \frac{1}{T} \int_0^T \boldsymbol{Y}(\bar{\boldsymbol{\chi}}, t).dt \quad \text{where } \epsilon \ll 1 \tag{B.2}$$

If the averaged system (B.2) has a *hyperbolic* fixed point, then the original NLTP system (B.1) will have a hyperbolic periodic orbit of the same stability type [106, 107]. That is, the averaged dynamics is representative of the time-periodic system as long as ϵ is small enough. To write the abstract form of the flight dynamics represented by Eq. (5.4) in the form of (B.1), that is amenable to the averaging theorem, we introduce a new time variable $\tau = \omega t$, where ω is the flapping frequency. The system (5.4) is then written as

$$\frac{d\boldsymbol{\chi}}{d\tau} = \frac{1}{\omega}(\boldsymbol{f}(\boldsymbol{\chi}) + \boldsymbol{g}(\boldsymbol{x}, \varphi(\tau))) \tag{B.3}$$

which is in the form (B.1) with $\epsilon = \frac{1}{\omega}$. That is, if flapping is performed with a high enough frequency that ϵ would be small enough to justify the application of the averaging theorem.

Averaging the system (B.3) and transforming it back to the original time variable, we obtain

$$\dot{\bar{\boldsymbol{\chi}}} = \boldsymbol{f}(\bar{\boldsymbol{\chi}}) + \bar{\boldsymbol{g}}(\bar{\boldsymbol{\chi}}) \tag{B.4}$$

where $\bar{\boldsymbol{g}}(\boldsymbol{\chi}) = \frac{1}{T} \int_0^T \boldsymbol{g}(\boldsymbol{\chi}, \varphi(t))dt$ represents the cycle-averaged aerodynamic loads. As such, the averaged dynamics of the system (5.1) is written as

$$\begin{pmatrix} \dot{\bar{u}}(t) \\ \dot{\bar{w}}(t) \\ \dot{\bar{q}}(t) \\ \dot{\bar{\theta}}(t) \end{pmatrix} = \begin{pmatrix} -\bar{q}(t)\bar{w}(t) - g\sin\bar{\theta}(t) \\ \bar{q}\bar{u}(t) + g\cos\bar{\theta}(t) \\ 0 \\ \bar{q}(t) \end{pmatrix} + \begin{pmatrix} \frac{1}{m}\bar{X}_o(t) \\ \frac{1}{m}\bar{Y}_o(t) \\ \frac{1}{m}\bar{Z}_o(t) \\ 0 \end{pmatrix} + \begin{pmatrix} \bar{X}_u(t) & \bar{X}_w(t) & \bar{X}_q(t) & 0 \\ \bar{Z}_u(t) & \bar{Z}_w(t) & \bar{Z}_q(t) & 0 \\ \bar{M}_u(t) & \bar{M}_w(t) & \bar{M}_q(t) & 0 \\ 0 & 0 & 0 & 0 \end{pmatrix} \begin{pmatrix} \bar{u}(t) \\ \bar{w}(t) \\ \bar{q}(t) \\ \bar{\theta}(t) \end{pmatrix} \tag{B.5}$$

where the over bar is used to denote an averaged quantity. It should be noted that although the variables in the averaged system (B.5) are averaged over the flapping cycle (fast time-scale), they

are still slowly time-varying, which allows for maneuvering of the FWMAV, e.g. transition from one equilibrium configuration to another.

B.2   Time Varying-Dynamics-Periodic Orbits

The periodic orbit for both hovering and forward flight is obtained using the optimized shooting method proposed by Botha and Dednam [91] as an extension to the general shooting method to solve for periodic solutions of both autonomous and non-autonomous nonlinear systems. This method is based on the Levenberg Marquart Algorithm (LMA), which is a non-linear least squares optimization scheme. The main idea of this method is the minimization of the residue vector, which is the difference between a point at a specific $T + \Delta\tau$ and another one at $\Delta\tau$. We consider the nonlinear dynamical system

$$\dot{\chi} = f(\chi, t, \epsilon) \tag{B.6}$$

where $\chi, f \in \mathbb{R}^n$. This system is a non-autonomous system because it depends explicitly on time. For a periodic solution

$$\chi(t) = \chi(t + T) \quad \forall \quad t \geq 0 \tag{B.7}$$

where $T > 0$ is the period. LMA is a method for solving nonlinear least squares problems [108]. Suppose that it is desired to fit a function $\hat{y}(t; \mathbf{p})$ to a set of m data points (t_i, y_i), where the independent variable is t and $\mathbf{p}$ is a vector of n parameters. For this problem it is necessary to minimize the sum of the weighted squares of the errors between the measured data and the curve fit function

$$\chi^2(\mathbf{p}) = \left[\sum_{i=1}^{m} \frac{y(t_i) - \hat{y}(t_i; \mathbf{p})}{w_i} \right]^2 \tag{B.8}$$
$$= y^T W y - 2y^T W \hat{y} + \hat{y}^T W \hat{y}$$

where W is the diagonal weighting matrix. Based on the gradient descent method, the perturbation h that moves the parameters in the direction of steepest descent is,

$$h_{gd} = \alpha J^T (y - \hat{y}) \tag{B.9}$$

where J is the Jacobian matrix and α is the step size. In the same manner, it can be shown that the Gauss-Newton perturbation is given by

$$[J^T W J]h_{gn} = J^T W (y - \hat{y}) \tag{B.10}$$

Since LMA adaptively varies the parameter updates between Gradient Descent and Gauss Newton methods, the resulting perturbation is given by

$$[J^T W J + \lambda I]h_{lm} = J^T W (y - \hat{y}) \tag{B.11}$$

The optimized shooting method can be applied to any system that can be expressed in the form of Eq. (B.6). In the original work, Botha used the period of the system to normalize the system by letting $\tau = t/T$ which yielded

$$\dot{x} = Tf(x, \alpha, T\tau) \tag{B.12}$$

The new variable τ allows for the simplification of the boundary conditions in Eq. (B.7) with $\tau = 1$ implying a full cycle. The residual is then written as

$$R = T \int_0^1 f(x, \alpha, \tau t) \tag{B.13}$$

Furthermore, the number of quantities to be optimized impact the residual. As such, we write

$$R = (x(1) - x(0), x(1 + \Delta\tau) - x(\Delta\tau), ..., x(1 + (p-1)\Delta\tau) - x((p-1)\Delta\tau)) \tag{B.14}$$

where $\Delta\tau$ is the integration step size. The natural number p in the residual equation is a requirement of the LMA and has to be chosen so that the number of components of the residual is greater than or equal to the number of quantities to be optimized. The main goal now is to minimize the residue vector to get the right initial conditions that will put the system in periodic equilibrium.

To capture a periodic orbit that ensures hovering or forward flight, the averaged inertial velocities should be set to zero or the required averaged forward speed, i.e. $\bar{V}_x = 0, 2m/s$. This can be achieved in several ways. In previous work [109], it was done by introducing new states $V_z = wcos(\theta) - usin(\theta)$ and $V_x = ucos(\theta) + wsin(\theta)$, where V_x and V_z are the inertial forward and vertical speeds. This will require the integration of these two states to the differential equations, which means a $2p$ more elements in the reside vector. This will increase the time required to minimize the residue. To reduce the computation time, we will require the average inertial velocities in the X and Z directions to be prescribed, i.e. for hover $\bar{V}_x = 0$, $\bar{V}_z = 0$, for forward, $\bar{V}_x = V_f$, $\bar{V}_z = 0$. This can be done by adding these two entires to the residue vector.

The system is subjected to a harmonic variation of the flapping angle

$$\varphi(t) = a_o + a_1 cos(2\pi ft) + b_1 sin(2\pi ft) \tag{B.15}$$

with a variation of the wing pitching angle

$$\eta(\tau) = \begin{cases} \alpha_d & \dot{\varphi}(\tau) \geq 0 \\ \pi - \alpha_u & \dot{\varphi}(\tau) \leq 0 \end{cases} \tag{B.16}$$

The objective of the optimization algorithm is to minimize the difference between the averaged inertial velocities and the desired ones along with other elements of the residue vector. For example,

if three elements are chosen for each state, i.e. $p = 3$, the residue vector will be as follows

$$
\boldsymbol{R} =
\begin{bmatrix}
u(1) - u(0) \\
u(1 + \Delta\tau) - u(\Delta\tau) \\
u(1 + 2\Delta\tau) - u(2\Delta\tau) \\
w(1) - w(0) \\
w(1 + \Delta\tau) - w(\Delta\tau) \\
w(1 + 2\Delta\tau) - w(2\Delta\tau) \\
q(1) - q(0) \\
q(1 + \Delta\tau) - q(\Delta\tau) \\
q(1 + 2\Delta\tau) - q(2\Delta\tau) \\
\theta(1) - \theta(0) \\
\theta(1 + \Delta\tau) - \theta(\Delta\tau) \\
\theta(1 + 2\Delta\tau) - \theta(2\Delta\tau) \\
\bar{V}_x - \bar{V}_{x_d} \\
\bar{V}_z - \bar{V}_{z_d}
\end{bmatrix}
\tag{B.17}
$$

where $\bar{V}_{x,z} = \frac{1}{T} \int_0^T V_{x,z}(\tau)d\tau$. The residual is minimized using the nonlinear square function in Matlab, **lsqnonlin**, with the **Levenberg-Marquardt** algorithm. $\Delta\tau$ was set equal to 10^{-2}. The output of the minimization process are the initial conditions that put the system in periodic equilibrium and are given in Table 5.1. The equations of motion (5.1) are integrated using **ODE45** with the initial conditions in Table 5.1.

B.3   Stability of Periodic Orbits

Stability of Linear Time Periodic (LTP) systems can be assessed using Floquet Theory[110]. Looking at Floquet multipliers of small systems of ODEs. These multipliers are the eigenvalues of the

monodromy matrix which is the solution at $t = T$ for the variational equation

$$\frac{d\Xi(t)}{dt} = \left.\frac{\partial F}{\partial x}\right|_{x(t)} \Xi(t) \tag{B.18}$$

where

$$\Xi(t) = \begin{pmatrix} m_{11} & m_{12} & m_{13} & m_{14} \\ m_{21} & m_{22} & m_{23} & m_{24} \\ m_{31} & m_{32} & m_{33} & m_{34} \\ m_{41} & m_{42} & m_{43} & m_{44} \end{pmatrix} \tag{B.19}$$

where $\Xi(t)$ is the state transition matrix and $\Xi(0)$ is the identity matrix. The initial conditions are the result of the optimization problem in subsection B.2. Using this initial condition will ensure that the system is in the periodic orbit and the values of Floquet multipliers will not change. The asymptotic stability of the solution can be assessed by checking whether the other Floquet multipliers are less than one. The periodic orbit is said to be asymptotically unstable if at least one of the Floquet multipliers lie outside the unit circle in the complex plane. Recall the system in Eq. (5.4), calculating its Jacobian

$$\frac{\partial F}{\partial \chi} = \frac{\partial f(\chi)}{\partial \chi} + \frac{\partial g_a(\chi, t)}{\partial \chi} \tag{B.20}$$

where

$$\frac{\partial f(\chi)}{\partial \chi} = \begin{pmatrix} 0 & -q & -w & -g\cos(\theta) \\ q & 0 & u & -g\sin(\theta) \\ 0 & 0 & 0 & 0 \\ 0 & 0 & 1 & 0 \end{pmatrix} \tag{B.21}$$

and

$$\frac{\partial g_a}{\partial \chi} = \begin{pmatrix} X_u(t) & X_w(t) & X_q(t) & 0 \\ Z_u(t) & Z_w(t) & Z_q(t) & 0 \\ M_u(t) & M_w(t) & M_q(t) & 0 \\ 0 & 0 & 0 & 0 \end{pmatrix} \tag{B.22}$$

Now Eq. (B.18) becomes

$$\frac{d\Xi(t)}{dt} = \left[\begin{pmatrix} 0 & -q & -w & -g\cos(\theta) \\ q & 0 & u & -g\sin(\theta) \\ 0 & 0 & 0 & 0 \\ 0 & 0 & 1 & 0 \end{pmatrix} + \begin{pmatrix} X_u(t) & X_w(t) & X_q(t) & 0 \\ Z_u(t) & Z_w(t) & Z_q(t) & 0 \\ M_u(t) & M_w(t) & M_q(t) & 0 \\ 0 & 0 & 0 & 0 \end{pmatrix} \right] \Xi(t) \qquad \text{(B.23)}$$

Equation (B.18) is solved for the monodromy matrix $\Xi(t)$. The new system states of Ξ is added to the state vector χ. The simulation is carried out using the results of the optimization problem and the identity matrix for Floquet multipliers as follows

$$\Xi_i(0) = \begin{bmatrix} 1 & 0 & 0 & 0 \\ 0 & 1 & 0 & 0 \\ 0 & 0 & 1 & 0 \\ 0 & 0 & 0 & 1 \end{bmatrix} \qquad \text{(B.24)}$$

The 16 new linearized states are added to the old states (u, w, q, θ). The new system to be solved contains 20 states. The new states added to the system of equations are

$$\frac{d\Xi(t)}{dt} = \begin{pmatrix} \dot{m}_{11} & \dot{m}_{12} & \dot{m}_{13} & \dot{m}_{14} \\ \dot{m}_{21} & \dot{m}_{22} & \dot{m}_{23} & \dot{m}_{24} \\ \dot{m}_{31} & \dot{m}_{32} & \dot{m}_{33} & \dot{m}_{34} \\ \dot{m}_{41} & \dot{m}_{42} & \dot{m}_{43} & \dot{m}_{44} \end{pmatrix} = \begin{pmatrix} X_u(t) & X_w(t) - q & X_q(t) - w & -g\cos(\theta) \\ Z_u(t) + q & Z_w(t) & Z_q(t) + u & -g\sin(\theta) \\ M_u(t) & M_w(t) & M_w(t) & 0 \\ 0 & 0 & 1 & 0 \end{pmatrix} \Xi(t)$$

$$\text{(B.25)}$$

Bibliography

[1] D. T. Greenwood, *Principles of dynamics*. Prentice-Hall Englewood Cliffs, NJ, 1988.

[2] H. Goldstein, C. P. Poole, and J. L. Safko, *Classical Mechanics: Pearson New International Edition*. Pearson Higher Ed, 2014.

[3] J. N. Reddy, *An introduction to the finite element method*, vol. 2. McGraw-Hill New York, 1993.

[4] S. A. Ragab and H. E. Fayed, *Introduction to Finite Element Analysis for Engineers*. CRC Press, 2017.

[5] C. Brown and W. Michael, "Effect of leading-edge separation on the lift of a delta wing," *Journal of the Aeronautical Sciences*, 1954.

[6] D. M. Chapman, "Ideal vortex motion in two dimensions: symmetries and conservation laws," *Journal of Mathematical Physics*, vol. 19, no. 9, pp. 1988–1992, 1978.

[7] N. M. Newmark, "A method of computation for structural dynamics," *Journal of the engineering mechanics division*, vol. 85, no. 3, pp. 67–94, 1959.

[8] A. A. Hussein, H. E. Taha, S. Ragab, and M. R. Hajj, "A variational approach for the dynamics of unsteady point vortices," *Aerospace Science and Technology*, vol. 78, pp. 559–568, 2018.

[9] A. Hussein, H. Taha, S. Ragab, and M. R. Hajj, "A variational approach for the dynamics of unsteady point vortices with application to impulsively started aerofoil," in *2018 Applied Aerodynamics Conference*, p. 3172, 2018.

[10] A. A. Hussein, M. R. Hajj, S. M. Elkholy, and G. M. ELbayoumi, "Dynamic stability of hingeless rotor blade in hover using padé approximations," *AIAA Journal*, pp. 1769–1777, 2016.

[11] T. Theodorsen and W. Mutchler, "General theory of aerodynamic instability and the mechanism of flutter," 1935.

[12] R. G. Loewy, "A two-dimensional approximation to the unsteady aerodynamics of rotary wings," *Journal of the Aeronautical Sciences (Institute of the Aeronautical Sciences)*, vol. 24, no. 2, 1957.

[13] T. Theodorsen, "General theory of aerodynamic instability and the mechanism of flutter," Tech. Rep. 496, NACA, 1935.

[14] R. G. Loewy, "A two-dimensional approximation to unsteady aerodynamics in rotary wings," *J. Aeronautical Sciences*, vol. 24, pp. 81–92, 1957.

[15] A. A. Hussein and R. A. Canfield, "Unsteady aerodynamic stabilization of the dynamics of hingeless rotor blades in hover," *AIAA Journal*, vol. 56, no. 3, pp. 1298–1303, 2017.

[16] M. H. Cho and I. Lee, "Aeroelastic stability of hingeless rotor blade in hover using large deflection theory," *AIAA Journal*, vol. 32, no. 7, pp. 1472–1477, 1994.

[17] A. Hussein, S. A. Ragab, H. E. Taha, and M. R. Hajj, "Optimal tail kinematics for fish-like locomotion using the unsteady vortex lattice method," in *2018 AIAA Aerospace Sciences Meeting*, p. 0311, 2018.

[18] E. Atta, O. Kandil, D. Mook, and A. Nayfeh, "Unsteady aerodynamic loads on arbitrary wings including wing-tip and leading-edge separation," *AIAA*, vol. 156, p. 1977, 1977.

[19] J. Katz and A. Plotkin, *Low-speed aerodynamics*, vol. 13. Cambridge University Press, 2001.

[20] H. Schlichting, "Boundary-layer theory," 1968.

[21] A. Hussein, H. E. Taha, and M. Hajj, "Minimum-time transition of fwmavs from hovering to forward flight," in *AIAA Atmospheric Flight Mechanics Conference*, p. 0017, 2016.

[22] I. E. Garrick, "On some reciprocal relations in the theory of nonstationary flows," 1938.

[23] J. M. Greenberg, "Airfoil in sinusoidal motion in a pulsating stream," 1947.

[24] C. E. Brown and W. H. Michael, "Effect of leading-edge separation on the lift of a delta wing," *Journal of the Aeronautical Sciences*, vol. 21, pp. 690–695, 1954.

[25] R. H. Beckwith and H. Babinsky, "Impulsively started flat plate flow," *Journal of Aircraft*, vol. 46, no. 6, pp. 2186–2189, 2009.

[26] K. Granlund, M. Ol, D. Garmann, M. Visbal, and L. Bernal, "Experiments and computations on abstractions of perching," *AIAA paper*, vol. 4943, p. 2010, 2010.

[27] C. Lin, "On the motion of vortices in two dimensions-ii some further investigations on the kirchhoff-routh function," *Proceedings of the National Academy of Sciences of the United States of America*, pp. 575–577, 1941.

[28] R. Clements, "An inviscid model of two-dimensional vortex shedding," *Journal of Fluid Mechanics*, vol. 57, no. 02, pp. 321–336, 1973.

[29] C. Wang and J. D. Eldredge, "Low-order phenomenological modeling of leading-edge vortex formation," *Theoretical and Computational Fluid Dynamics*, vol. 27, no. 5, pp. 577–598, 2013.

[30] C. Lin, "On the motion of vortices in two dimensions i. existence of the kirchhoff-routh function," *Proceedings of the National Academy of Sciences*, vol. 27, no. 12, pp. 570–575, 1941.

[31] L. M. Milne-Thompson, "Theoretical hydrodynamics," *London: MacMillan, 1968, 5th ed.*, vol. 1, 1968.

[32] E. Kanso and B. G. Oskouei, "Stability of a coupled body–vortex system," *Journal of Fluid Mechanics*, vol. 600, pp. 77–94, 2008.

[33] H. Aref, "Point vortex dynamics: a classical mathematics playground," *Journal of mathematical Physics*, vol. 48, no. 6, p. 065401, 2007.

[34] C. W. Rowley and J. E. Marsden, "Variational integrators for degenerate lagrangians, with application to point vortices," in *Decision and Control, 2002, Proceedings of the 41st IEEE Conference on*, vol. 2, pp. 1521–1527, IEEE, 2002.

[35] P. K. Newton, *The N-vortex problem: analytical techniques*, vol. 145. Springer Science & Business Media, 2013.

[36] E. L. Hill, "Hamilton's principle and the conservation theorems of mathematical physics," *Reviews of Modern Physics*, vol. 23, no. 3, p. 253, 1951.

[37] H. Lamb, *Hydrodynamics*. Cambridge university press, 1932.

[38] S. Michelin and S. G. L. Smith, "An unsteady point vortex method for coupled fluid–solid problems," *Theoretical and Computational Fluid Dynamics*, vol. 23, no. 2, pp. 127–153, 2009.

[39] A. A. Tchieu and A. Leonard, "A discrete-vortex model for the arbitrary motion of a thin airfoil with fluidic control," *Journal of Fluids and Structures*, vol. 27, no. 5, pp. 680–693, 2011.

[40] H. Wagner, "Über die entstehung des dynamischen auftriebes von tragflügeln," *ZAMM-Journal of Applied Mathematics and Mechanics/Zeitschrift für Angewandte Mathematik und Mechanik*, vol. 5, no. 1, pp. 17–35, 1925.

[41] L. I. Sedov, "Two-dimensional problems of hydrodynamics and aerodynamics," *Moscow Izdatel Nauka*, vol. 1, 1965.

[42] L. V. Ahlfors, "Complex analysis: an introduction to the theory of analytic functions of one complex variable," *New York, London*, 1953.

[43] P. G. Saffman, *Vortex dynamics*. Cambridge university press, 1992.

[44] J. Eldredge and C. Wang, "Improved low-order modeling of a pitching and perching plate," *AIAA Paper*, vol. 3579, p. 2011, 2011.

[45] T. V. Karman, "Airfoil theory for non-uniform motion," *Journal of the Aeronautical Sciences*, vol. 5, no. 10, pp. 379–390, 1938.

[46] J. D. Eldredge, "Numerical simulation of the fluid dynamics of 2d rigid body motion with the vortex particle method," *Journal of Computational Physics*, vol. 221, no. 2, pp. 626–648, 2007.

[47] D. Cleaver, Z. Wang, and I. Gursul, "Investigation of high-lift mechanisms for a flat-plate airfoil undergoing small-amplitude plunging oscillations," *AIAA journal*, 2013.

[48] D. Calderon, Z. Wang, and I. Gursul, "Lift-enhancing vortex flows generated by plunging rectangular wings with small amplitude," *AIAA journal*, 2013.

[49] R. T. Jones, *The unsteady lift of a wing of finite aspect ratio*, vol. 681. NACA, 1940.

[50] E. H. Dowell, "A simple method for converting frequency domain aerodynamics to the time domain," 1980.

[51] C. Venkatesan and P. Friedmann, "New approach to finite-state modeling of unsteady aerodynamics," *AIAA Journal*, vol. 24, no. 12, pp. 1889–1897, 1986.

[52] K. R. V. Kaza and R. G. Kvaternik, "Application of unsteady airfoil theory to rotary wings," *Journal of Aircraft*, vol. 18, no. 7, pp. 604–605, 1981.

[53] D. H. Hodges and E. H. Dowell, "Nonlinear equations of motion for elastic bending and torsion of twisted non-uniform rotor blades," tech. rep., Dec.1974.

[54] P. Friedmann, "Influence of modeling and blade parameters on the aeroelastic stability of a cantilevered rotor," *AIAA Journal*, vol. 15, no. 2, pp. 149–158, 1977.

[55] M. Dinyavari and P. Friedmann, "Unsteady aerodynamics in time and frequency domains for finite time arbitrary motion of rotary wings in hover and forward flight," in *Structures, Structural Dynamics and Materials Conference, 25 th, Palm Springs, CA*, pp. 266–282, 1984.

[56] M. Dinyavari and P. Friedmann, "Time domain unsteady incompressible cascade airfoil theory for helicopter rotors in hover," *AIAA Journal*, vol. 27, no. 3, pp. 257–267, 1989.

[57] N. T. Sivaneri and I. Chopra, "Dynamic stability of a rotor blade using finite element analysis," *AIAA Journal*, vol. 20, no. 5, pp. 716–723, 1982.

[58] R. C. Dorf and R. H. Bishop, "Modern control systems," 1998.

[59] J. W. Edwards, "Unsteady aerodynamic modeling for arbitrary motions," *AIAA Journal*, vol. 17, no. 4, pp. 365–374, 1979.

[60] J. Leishman and K. Nguyen, "State-space representation of unsteady airfoil behavior," *AIAA Journal*, vol. 28, no. 5, pp. 836–844, 1990.

[61] P. Friedmann and C. Yuan, "Effect of modified aerodynamic strip theories on rotor blade aeroelastic stability," *AIAA Journal*, vol. 15, no. 7, pp. 932–940, 1977.

[62] M. Dinyavari and P. Friedmann, "Application of time-domain unsteady aerodynamics to rotary-wing aeroelasticity," *AIAA Journal*, vol. 24, no. 9, pp. 1424–1432, 1986.

[63] M. H. Cho and I. Lee, "Aeroelastic analysis of multibladed hingeless rotors in hover," *AIAA journal*, vol. 33, no. 12, pp. 2348–2353, 1995.

[64] H. Shahverdi, A. Nobari, M. Behbahani-Nejad, and H. Haddadpour, "Aeroelastic analysis of helicopter rotor blade in hover using an efficient reduced-order aerodynamic model," *Journal of fluids and structures*, vol. 25, no. 8, pp. 1243–1257, 2009.

[65] D. Hodges and R. Ormiston, "Stability of elastic bending and torsion of uniform cantilevered rotor blades in hover," in *14th Structures, Structural Dynamics, and Materials Conference*, p. 405, 1973.

[66] C. Lindsey, "1 form, function, and locomotory habits in fish," *Fish physiology*, vol. 7, pp. 1–100, 1979.

[67] M. Bozkurttas, R. Mittal, H. Dong, G. Lauder, and P. Madden, "Low-dimensional models and performance scaling of a highly deformable fish pectoral fin," *Journal of Fluid Mechanics*, vol. 631, pp. 311–342, 2009.

[68] S. J. Lighthill, *Mathematical biofluiddynamics*. SIAM, 1975.

[69] P. Webb and R. Blake, "Swimming. in functional vertebrate morphology," 1983.

[70] L. Maddock, Q. Bone, and J. M. Rayner, *The Mechanics and Physiology of Animal Swimming*. Cambridge University Press, 1994.

[71] G. S. Triantafyllou, M. Triantafyllou, and M. Grosenbaugh, "Optimal thrust development in oscillating foils with application to fish propulsion," *Journal of Fluids and Structures*, vol. 7, no. 2, pp. 205–224, 1993.

[72] S. Belotserkovskii, "Study of the unsteady aerodynamics of lifting surfaces using the computer," *Annual Review of Fluid Mechanics*, vol. 9, no. 1, pp. 469–494, 1977.

[73] C. Rehbach, "Numerical calculation of three-dimensional unsteady flows with vortex sheets," in *16th Aerospace Sciences Meeting*, p. 111, 1978.

[74] P. Konstadinopoulos, D. Thrasher, D. Mook, A. Nayfeh, and L. Watson, "A vortex-lattice method for general, unsteady aerodynamics," *Journal of aircraft*, vol. 22, no. 1, pp. 43–49, 1985.

[75] D. Levin and J. Katz, "Vortex-lattice method for the calculation of the nonsteady separated flow over delta wings," *Journal of Aircraft*, vol. 18, no. 12, pp. 1032–1037, 1981.

[76] J. Katz, "Lateral aerodynamics of delta wings with leading-edge separation," *AIAA journal*, vol. 22, no. 3, pp. 323–328, 1984.

[77] G. J. Berman and Z. J. Wang, "Energy-minimizing kinematics in hovering insect flight," *Journal of Fluid Mechanics*, vol. 582, no. 1, pp. 153,168, 2007.

[78] M. Kurdi, B. Stanford, and P. Beran, "Kinematic optimization of insect flight for minimum mechanical power," AIAA paper 2010-1420, Jan 2010.

[79] H. E. Taha, M. R. Hajj, and A. H. Nayfeh, "Wing kinematics optimization for hovering micro air vehicles using calculus of variation," *Journal of Aircraft*, vol. 50, no. 2, pp. 610–614, 2013.

[80] B. K. Stanford and P. S. Beran, "Analytical sensitivity analysis of an unsteady vortex-lattice method for flapping-wing optimization," *Journal of Aircraft*, vol. 47, no. 2, pp. 647–662, 2010.

[81] M. Ghommem, M. R. Hajj, B. K. Mook, D. T.and Stanford, R. D. Beran, P. S.and Snyder, and L. T. Watson, "Global optimization of actively morphing flapping wings," *Journal of Fluids and Structures*, vol. 33, pp. 210–228, 2012.

[82] L. Schenato, D. Campolo, and S. S. Sastry, "Controllability issues in flapping flight for biomemetic mavs," vol. 6, pp. 6441–6447, 42nd IEEE conference on Decision and Control, 2003.

[83] D. B. Doman, M. W. Oppenheimer, and D. O. Sigthorsson, "Wingbeat shape modulation for flapping-wing micro-air-vehicle control during hover," *Journal of Guidance, Control and Dynamics*, vol. 33, no. 3, pp. 724–739, 2010.

[84] M. W. Oppenheimer, D. B. Doman, and D. O. Sigthorsson, "Dynamics and control of a biomimetic vehicle using biased wingbeat forcing functions," *Journal Guidance, Control and Dynamics*, vol. 34, no. 1, pp. 204–217, 2011.

[85] H. E. Taha, M. R. Hajj, A. H. Roman, and A. H. Nayfeh, "A calculus of variations approach for optimum maneuverability of flapping mavs near hover," *submitted to Journal of Guidance Control and Dynamics*.

[86] M. Bhatia, M. Patil, C. Woolsey, B. Stanford, and P. Beran, "Stabilization of flapping-wing micro-air vehicles in gust environments," *Journal of Guidance, Control, and Dynamics*, vol. 37, no. 2, pp. 592–607, 2014.

[87] D. O. Sigthorsson, M. W. Oppenheimer, and D. B. Doman, "Flapping wing micro-air-vehicle control employing triangular wave strokes and cycle-averaging," AIAA-paper 2010-7553, Aug 2010.

[88] R. J. Wood, "The first takeoff of a biologically inspired at-scale robotic insect," *IEEE Transactions on Robotics and Automation*, vol. 24, no. 2, pp. 341–347, 2008.

[89] H. E. Taha, A. H. Nayfeh, and M. R. Hajj, "Aerodynamic-dynamic interaction and longitudinal stability of hovering mavs/insects," No. AIAA-Paper 2013-1707, Apr 2013.

[90] H. E. Taha, M. R. Hajj, and A. H. Nayfeh, "Longitudinal flight dynamics of hovering mavs/insects," *Journal of Guidance, Control and Dynamics*, 2014. doi: 10.2514/1.62323.

[91] W. Dednam and A. E. Botha, "Optimized shooting method for finding periodic orbits of nonlinear dynamical systems," *Engineering with Computers*, vol. 31, no. 4, pp. 749–762, 2015.

[92] H. E. Taha, A. H. Nayfeh, and M. R. Hajj, "On the longitudinal flight dynamics of hovering mavs/insects," *Journal of Guidance Control and Dynamics, In Press*, 2013.

[93] J. M. Dietl and E. Garcia, "Ornithopter optimal trajectory control," *Aerospace Science and Technology*, vol. 26, no. 1, pp. 192–199, 2013.

[94] M. W. Oppenheimer, D. B. Doman, and D. O. Sigthorsson, "Dynamics and control of a biomimetic vehicle using biased wingbeat forcing functions," *Journal of guidance, control, and dynamics*, vol. 34, no. 1, pp. 204–217, 2011.

[95] S. D. Kelly and R. M. Murray, "Modelling efficient pisciform swimming for control," *International Journal of Robust and Nonlinear Control*, vol. 10, pp. 217–?241, 2000.

[96] K. A. Morgansen, B. I. Triplett, and D. J. Klein, "Geometric methods for modeling and control of free-swimming fin-actuated underwater vehicles," *IEEE Transactions on Robotics*, vol. 23, no. 6, pp. 1184?–1199, 2007.

[97] J. Wang, S. Chen, and X. Tan, "Control-oriented averaging of tail-actuated robotic fish dynamics," in *Proc. IEEE Conference on Decision and Control*, (Washington, DC), pp. 591–596, June 2013.

[98] E. Kelasidi, *Modeling, Control and Energy Efficiency of Underwater Snake Robots*. PhD thesis, Norwegian University of Science and Technology, Trondheim, Norway, December 2015.

[99] T. Takayama and S. Hirose, "Amphibious 3D active cord mechanism "helix" with helical swimming motion," in *Proc. IEEE/RSJ Conference on Intelligent Robots and Systems (IROS)*, (Lausanne, Switzerland), pp. 775–780, Sept. 30-Oct. 2 2002.

[100] K. McIsaac and J. Ostrowski, "Motion planning for anguilliform locomotion," *IEEE Transactions on Robotics and Automation*, vol. 19, no. 4, pp. 637?–625, 2003.

[101] H. Yamada, S. Chigisaki, M. Mori, K. Takita, K. Ogami, and S. Hirose, "Development of amphibious snake-like robot ACM-R5," in *Proc. 36th International Symposium on Robotics*, (Tokyo, Japan), 2005.

[102] M. Porez, F. Boyer, and A. J. Ijspeert, "Improved Lighthill fish swimming model for bio-inspired robots: Modeling, computational aspects and experimental comparisons," *The International Journal of Robotics Research*, vol. 33, no. 10, pp. 1322?–1341, 2014.

[103] F. Boyer, M. Porez, and W. Khalil, "Macro-continuous computed torque algorithm for a three-dimensional eel-like robot," *IEEE Transactions on Robotics*, vol. 22, no. 4, pp. 763?–775, 2006.

[104] A. Wiens and M. Nahon, "Optimally efficient swimming in hyper-redundant mechanisms: control, design, and energy recovery," *Bioinspiration and Biomimetics*, vol. 7, no. 4, 2012.

[105] I. E. Garrick, "On some reciprocal relations in the theory of nonstationary flows," Tech. Rep. 629, NACA, 1938.

[106] H. K. Khalil, "Nonlinear systems," 2002. 3rd ed., PrenticeHall, Upper Saddle River, NJ.

[107] J. Guckenheimer and P. Holmes, *Nonlinear Oscillations, Dynamical Systems, and Bifurcations of Vector Fields*. New York, NY: Academic Press, 1983.

[108] K. Madsen, H. B. Nielsen, and O. Tingleff, "Methods for non-linear least squares problems," 2004.

[109] A. Elsadek, H. E. Taha, and G. M. El-Bayoumi, "Stability analysis of longitudinal dynamics of hovering flapping mavs/insects," in *AIAA Atmospheric Flight Mechanics Conference*, p. 1635, 2017.

[110] K. Lust, "Improved numerical floquet multipliers," *International Journal of Bifurcation and Chaos in Applied Sciences and Engineering*, vol. 11.